2011

# Characterization of a Blast Wave Device and Blast Wave Induced Traumatic Brain Injury in a Rat Model by Magnetic Resonance Imaging and Spectroscopy

Frank Corwin
*Virginia Commonwealth University*

# Characterization of a Blast Wave Device and Blast Wave Induced Traumatic Brain Injury in a Rat Model by Magnetic Resonance Imaging and Spectroscopy

Dissertation submitted in partial fulfillment of the requirements for the degree of Doctor of Philosophy in the Division of Medical Physics, Department of Radiation Oncology, School of Medicine, Virginia Commonwealth University.

Frank David Corwin
Virginia Commonwealth University

Director: Kenneth A. Kraft, PhD.
Associate Professor
Department of Radiology

Virginia Commonwealth University.
Richmond, Virginia
May, 2011

# Table of Contents

# List of Figures

# List of Tables

Page

Page

# Abstract

CHARACTERIZATION OF A BLAST WAVE DEVICE AND BLAST WAVE INDUCED TRAUMATIC BRAIN INJURY IN A RAT MODEL BY MAGNETIC RESONANCE IMAGING AND SPECTROSCOPY

Frank D. Corwin

Dissertation submitted in partial fulfillment of the requirements for the degree of Doctor of Philosophy at Virginia Commonwealth University.

Virginia Commonwealth University, Richmond, VA, 2011

Director: Kenneth A. Kraft

Blast wave induced traumatic brain injury (bTBI) is a modality of injury that has come into prominence at the current time due to the large number of military and civilian personnel who have experienced the localized shock wave produced by explosive devices. The shock wave will travel concentrically outward from the explosive center, being absorbed and transmitted thru soft objects, such as tissue, and reflecting off stationary obstructions. Transmission and absorption in tissues can result in a number of physiological measureable injuries, the most common of which being what is frequently called “blast lung”. Blast lung involves the spalling effect at air-tissue interfaces. Another documented effect involves the asynchronous motion of tissue, particularly in the cranium, as the shock wave passes by. This predominately manifests itself in what is believed to be diffuse axonal injury and initiation of secondary injury mechanism.

This study is designed to explore the relationship between shock waves and bTBI. A blast device was constructed for generating a free field shock wave through the high pressure rupture of a polycarbonate membrane. Air pressure in a small chamber is increased to a value several orders of magnitude greater than ambient air pressure and is held in place with the polycarbonate member. At the rupture of this membrane a shock wave is created. Measurements of this blast event, carried out with a piezoelectric pressure transducer, have shown that this shock wave is reproducible for the different membrane materials tested and is symmetrical with respect to the central axis of the high pressure chamber and exit nozzle. Having characterized the shock wave properties in the blast field, a location was chosen at which maximum shock wave pressure could be applied to the cranium for inducing bTBI.

Experiments involving blast wave exposure were performed on two separate groups of animals in an attempt at establishing injury. One group was placed at a fixed distance directly below the blast nozzle, thereby experiencing both the shock wave and the associated air blast from the residual air in the chamber, and one placed at a defined distance off-axis to avoid the air blast, yet receiving two sequential blast exposures. All animal studies were approved by the VCU Institutional Animal Care and Use Committee.

The degree of injury was then assessed with the use of magnetic resonance imaging (MRI) and spectroscopy (MRS). Image Data was acquired on a 2.4 Tesla magnet for assessing changes in either the total percent water concentration or the apparent diffusion coefficients (ADC) of selected regions of interest in the brain of rats. Localized proton spectroscopic data was acquired from a voxel placed centrally in the brain. The baseline values of these parameters were established before the induction of bTBI. After the blast exposure, the animals were followed up with MRI and MRS at defined intervals over a period of one week.

The first group of animals received blast exposure directly underneath the blast device nozzle and the MR data does suggest changes in some of the measureable parameters from baseline following blast exposure. This blast wave data though is confounded with additional and undesirable characteristics of the blast wave. The second group of animals that received a pure shock wave blast exposure revealed no remarkable changes in the MR data pre- to post-blast exposure. The percent water concentration, ADC and spectroscopic parameters were for statistical purposes identical before and after the blast. The resolution of this negative result will require reconsideration of the free field blast exposure concept.

# Chapter 1

# Introduction

## A. Traumatic Brain Injury Overview

Traumatic brain injury (TBI) is the result of an external mechanical force applied to the cranium and the intracranial contents resulting in damage to the brain. It is a nondegenerative, noncongenital insult to the brain. TBI manifests itself clinically over a spectrum of injury from mild concussion, to coma and death and has long been identified as a major health and socioeconomic problem throughout the world. [1] In the United States, falls are listed as the primary cause of TBI (at 28% of all reported), with automobile accidents (at 20%) being a close second. Additional major sources of TBI are being struck by an object (19%) and assault (9%). [2]

Injuries are divided into 2 broad subcategories: primary injuries, which occur at the moment of trauma, and secondary injuries, that may occur with a latency of hours or days. Primary injuries involve macroscopic events, both external and internal to the skull. External injuries might include skull fractures, lacerations, and contusions, and can be readily visualized. Internal injuries such as hematomas and diffuse axonal injury may be assessed with various imaging tools that could include computed tomography and magnetic resonance imaging. Secondary injuries are attributable to cellular responses and damages due to the primary effect and develop over a period of hours to days following the insult. A significant secondary injury response is the sudden rise in brain edema, leading to brain swelling, following trauma. It is well

documented that the rise in brain edema leads to an increase in intracranial pressure, which is a frequent cause of death. [3] Additional secondary effects may be observed in the intracranial proton spectra with magnetic resonance spectroscopy.

### B. Traumatic Brain Injury induced by Blast Waves

A particular subset of TBI is injury due to blast wave exposure, frequently referenced as bTBI. Blast waves are generated by the instantaneous conversion of an explosive solid material into gases, resulting in a sudden, nearly discrete change in atmospheric pressure. As the conversion of the explosive solid material into gases proceeds at velocities that exceed the speed of sound of the surrounding gas, the individual elements in the gas are pushed together faster than the disturbance can be relieved by thermal motion of the gas molecules. Consequently, the molecules pile up and the density, pressure and temperature increase rapidly. Eventually, because the wave propagation speed is directly related to these quantities, a state is reached in which the piling up that is caused by the material motion is just balanced by the dispersion of the thermal motion of the molecules. The gases rapidly expand in a spherical direction from the explosive center, creating a front of compression in the surrounding air, commonly known as a shock wave or blast wave. The blast wave is defined as the instantaneous pressure over atmospheric pressure which is associated with the blast.

The gases from the explosion push out circumferentially into the undisturbed media. At the blast front, a high pressure region is created. The high pressure pulse is immediately followed by a negative or below-atmospheric pressure region [4]. This blast wave can be designated on a pressure-time recording as the positive phase of the blast wave. This is

illustrated in Figure 1.1. An impulse signature of this type is often referred to as a Friedlander wave, named after the British mathematician Fredrick G. Friedlander who used such

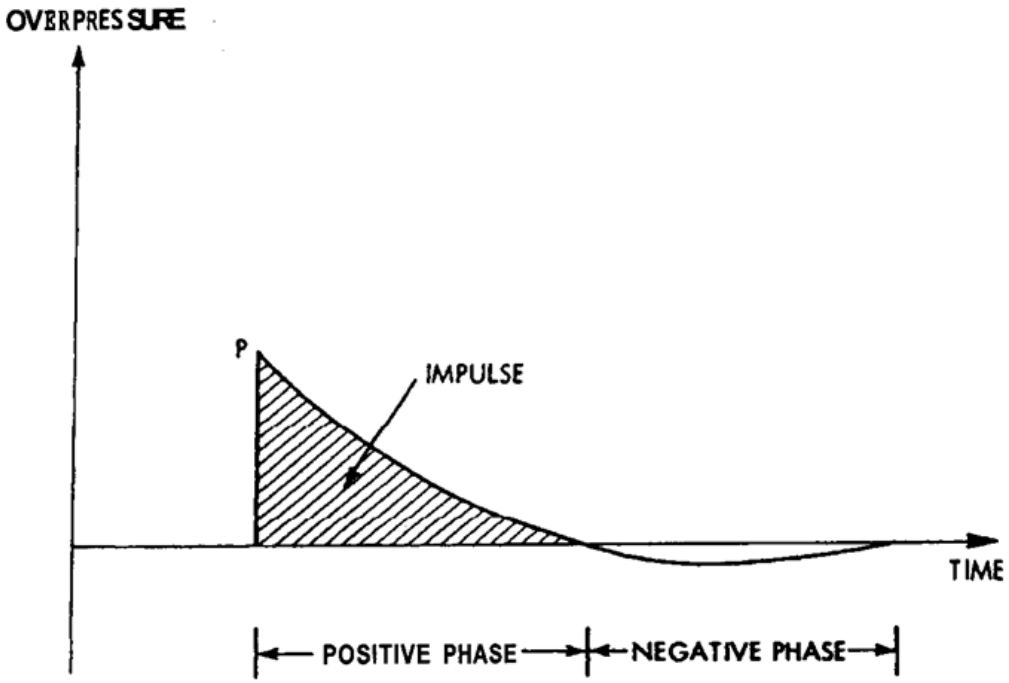


Figure 1.1. Classic Friedlander Shock Wave

waveforms in the study of diffraction [5]. Mathematically this waveform is described by what has come to be known as the Friedlander wave equation:

$$p(t) = (1 - \frac{t}{c})e^{-\frac{t}{c}} \tag{1.1}$$

Where: t is the time point of measurements of the shock wave, c is the speed of sound in the surrounding gas and p(t) is wave pressure at that time point.

In the positive phase, the air is compressed almost instantly to a peak value that decays exponentially back to and then below the ambient (baseline) pressure, into a negative phase. During the positive phase, the flow of gas is away from the explosion, while during the negative phase, the flow is reversed [4].

A number of factors will affect the magnitude of the blast overpressure. They are: the energy of the explosion, the distance from the detonation and the amplification that can be produced as the blast wave is reflected from solid surfaces leading to constructive interferences [6]. The blast wave will rapidly lose energy, dissipating it to the surrounding gas, as the spherical front progresses away from the blast center.

A shock wave is a non-turbulent, but supersonic flow of air. The shock wave can be described mathematically through its dependence on mass, momentum and energy conservation.

$$\rho_1 v_1 = \rho_2 v_2 = j \tag{1.2}$$

$$P_1 + \rho_1 v_1^2 = P_2 + \rho_2 v_2^2 \tag{1.3}$$

$$h_1 + \frac{v_1^2}{2} = h_2 + \frac{v_2^2}{2} \tag{1.4}$$

Where $\rho$ is the density (in units of kg/m$^3$), $v$ is the gas velocity (in units of m/s), P the pressure (in units of Pa) and $h$ is the internal energy (in units of J/kg). These equations connect the

unperturbed values of the gas parameters upstream of the front (subscript 1) with the values downstream of the front (subscript 2). The first two equations can be used to obtain the velocity of the downstream flow relative to the upstream flow:

$$v_1 - v_2 = \sqrt{\frac{(P_2 - P_1)(\rho_2 - \rho_1)}{\rho_1 P_2}}\,. \tag{1.5}$$

Equation (1.5), along with (1.4), derives the following expression which links the pressures and densities on either side of the front:

$$h_2 - h_1 = \frac{(P_2 - P_1)(\rho_2 - \rho_1)}{2\rho_2\rho_1}, \tag{1.6}$$

or, with $V = \frac{1}{\rho}$ (1.7)

$$h_2 - h_1 = \frac{1}{2}(V_2 - V_1)(P_1 + P_2), \tag{1.8}$$

Equation (1.6) and (1.7) are called the shock adiabatic or the Hugoniot –Rankine adiabatic. It relates the change in the internal energy, to the pressure and density of the traveling shock wave front [7] [8]. The internal energy, as will be discussed later, is the kinetic energy of the advancing shock wave. It may be calculated from the measured pressure difference between pressure transducers, one placed orthogonal and the other normal to the advancing shock wave. The adiabatic may be graphically illustrated by the inverse relationship between the pressure and the volume of a gas, where both ends asymptotically approach a non-zero pressure or volume value.

An additional component of an explosive event, beyond the creation of the blast wave, is the air blast pulse. The air blast pulse is a mass of turbulent air placed into motion following the explosive event. The air blast has a high force, but very limited range; becoming inconsequential at much shorter distances than the blast wave.

Upon striking a body, the blast wave is both reflected and absorbed by the tissue. The absorbed blast wave will induce stress and shear waves when interacting with the body [9]. Stress waves are longitudinal pressure forces that propagate in the direction of travel of the wave. They can be most easily visualized as a "push-pull" of the material. They may move at supersonic speeds and create a "spalling" effect at air-tissue interfaces, resulting in severe microvascular damage. This may be visualized by recalling the waveform for the Friedlander wave in Figure 1.1. The initial high pressure phase will compress tissue or cellular structure, while the following negative phase will cause expansion beyond normal size. This is most readily seen in the lungs, with what is commonly known as blast lung, where alveolar walls are damaged resulting in lung laceration and hemothorax [10]. Shear waves also move in the direction of travel of the wave, but impart their energy in the transverse direction. This may cause asynchronous movement of tissue and potential disruption of attachments. This predominately manifests itself in diffuse axonal injury (DAI) and initiation of secondary injury mechanisms [11].

The mechanism of transduction of the blast wave to the brain is controversial. Current theories, for which both positive and negative results exist, are: (1) through direct trans-cranial propagation; (2) via the vasculature system and; (3) from the cerebrospinal fluid in the spinal cord to the foramen magnum in the brain[12]. Although Cernak [13] has hypothesized from rodent studies that blast waves transfer kinetic energy through the vasculature, and trigger pressure oscillations in the blood vessels leading to the brain, others have found little supporting evidence to that theory in other animals models. [14]. These disparate observations suggest that there may be species differences in the role of peripheral vasculature in bTBI.

Early evidence suggests that closed head TBI and bTBI may produce very similar symptoms in terms of cognitive impairments. It can be expected therefore that abnormalities observed in neurological imaging may likewise be similar. This will be tested with the use of Magnetic Resonance Imaging (MRI).

### C. Characteristics of Blast Wave Injury

Blast injuries are defined according to the direct cause of the specific wound. The injuries are classified as primary, secondary, tertiary or quaternary. Primary injuries are those wounds resulting directly from the blast pulse. The most vulnerable organs are considered to be those with air-fluid interfaces, such as the lungs. Rupture of the tympanic membrane is the most frequent injury and is the injury that has received the greatest research effort [15]. Recent research, and the focus of this report, indicated that primary blast wave overpressure can also lead to TBI effects. Secondary injuries are due to objects set in motion, or propelled, by the blast, such as shrapnel and debris. Tertiary blast wounds are inflicted when the body is propelled by the blast wave and strikes a stationary object [5-Okie]. Finally, quaternary blast injuries include a wide variety of conditions, such as burns from the super-heated gases, toxic inhalations or crush injuries from collapsed structures or displaced heavy objects [16].

All stages of blast injuries are frequently associated with traumatic sequelae that may be externally apparent on the body. Primary blast exposure to the head, on the other hand has been shown to induce symptoms that cannot be explained through external observations and must be investigated on a neuropathological basis. Disruption of white matter tract integrity with functional disconnections due to axonal injury has been implicated in slowing of cognitive processing and other impairments. MRI has been shown to be a useful technique for evaluating

white matter tract integrity. This study will utilize diffusion tensor imaging (DTI) to study the white matter microstructure. DTI, as to be described in detail later, is an imaging technique that emphasizes the diffusion of water in structures. White matter tracts, consisting of myelinated axons, normally constrain the isotropic diffusion of water; i.e., water motion is constrained to occur primarily in the direction of the fiber tracts. A disruption in the white matter tracts will result in water diffusion becoming less anisotropic and having the ability to diffuse more freely.

### D. History of Blast Wave Injury

The mechanisms by which blast waves induce injury and death have been increasingly scrutinized throughout the twentieth century as more powerful explosives have come into general use, particularly during warfare. [15]. The arguments though, surrounding the origin of the injury have repeatedly shifted between an organic injury and psychiatric state.

The first published systematic research of blast injuries was conducted in 1914, after Swiss researcher Franchino Rusca observed three soldiers that had been unexpectedly killed, with no external injuries, during the Balkan Wars by a bursting grenade. To study this phenomenon, he placed rabbits inside a sand pit and exposed them to blasts from 100 g of dynamite. Rusca could not account for the animals sudden deaths. However, the gross blast injuries that he described (pulmonary parenchymal hemorrhage, gastrointestinal contusions and gastrointestinal ruptures) are now recognized as primary blast injuries [17].

Medical personnel in World War I knew that a blast could cause bodily displacement, and result in ear injury, but no systematic accounts of internal injuries or deaths from blast exposure were reported in the military medical literature. At the time the blast wave was believe to affect primarily the nervous system. British Army physicians, Drs. Fred Mott, Gordon

Holmes and Charles Myers provided some of the first documentation on cases of blast injuries. They noted that those who survived blast explosions with no external injuries frequently suffer from acute symptoms, such as: amnesia, severe headaches, tinnitus, hypersensitivity to noise and tremors: a condition that had come to be known as "shell shock". [18-20]. Because shell shock was characterized by a wide range of common symptoms, it was open to multiple etiological explanations. At first, forces of compression and decompression were thought to cause a cerebral lesion, a form of commotion cerebri. [21] Mott initially argued that in extreme cases, shell shock could be fatal if intense commotion affected "the delicate colloidal structures of the living tissues of the brain and spinal cord", arresting "the functions of the vital centers in the medulla". [22] Mott also speculated that residual carbon monoxide gases from the explosive warhead contributed a role in the observed effects. In other words, shell shock was framed as an organic problem even though the pathology remained unclear.

However, as the war progressed, the number of British soldiers diagnosed with shell shock approached epidemic proportions. [23] As an increasing appreciation of the stress of trench warfare and the finding that many shell shocked soldiers who had been nowhere near an explosion but had identical symptoms to those who had, a psychological explanation was put forward. For these cases, the term "emotional", rather than "commotional" shock was proposed. The psychological explanation gained ground over the neurological in part because it offered the British Army an opportunity to quickly return shell-shocked soldiers to active duty. Servicemen invalidated from the front were given a preliminary label of "not yet diagnosed, nervous" and those who failed to recover but had no visible cerebral injury were then classified as "neurasthenic". These redefinitions of etiology and management of shell shock served to inhibit further the design of an effective treatment protocol. In the last year of the war the acute

treatment of emotional cases was, as summarized by the Prideaux Report, [24] 'reassurance combined with an appeal to personal and patriotic pride and a large dose of bromide'. [25]

By 1918 though, regimental medical officers in the trenches developed a pragmatic and eclectic understanding of shell shock. Shepard, in his book *A War of Nerves: Soldiers and Psychiatrist in the Twentieth Century*, commented that if anything, the theoretical understanding of shell-shock evolved further at the end of the war, away from a simple psychological point of view. [26] In later papers, Fred Mott [27], in describing autopsy results on two cases of death from shock, referencing the "vascular disturbances in the central nervous system… and rupture of delicate walled vessels with microscopic hemorrhages", implying that these vascular changes are antecedent to the cellular changes that could initiate symptoms. [28]

Following the war however, the British government, facing an enormous case load of wounded soldiers on military pensions, produced the *Report of the War Office Committee of Enquiry into "Shell-shock"*, which was published in 1922. [29] The report concluded that there is little or no evidence about the cause of death in any of these cases, either from the point of view of the circumstances in which it occurred or from that of post-mortem examination. The subject of shell-shock and blast injury effectively became taboo and was laid to rest for the next 20 years.

A spattering of research into blast wave injury was begun during this time though. Rusca, as mentioned above, found that a blast exposure alone could kill, but could not explain why. Carver and Dinsley [30] studied the effects seen in battle injuries and through observations, postulated three zones surrounding a blast exposure. First, those closest to the explosion experienced direct concussion produced by fragments of shell, or earth, or being bodily displaced. Second, those close enough to the explosion to be subject to the violent

variations in pressure, but suffer no bodily injury. Third were those who experienced just the rapid atmospheric vibrations from the explosion. They studied the effects in these zones using both explosions in water and on land. Animals (rats and mice) in the first zone were killed outright or severely wounded by fragments. Autopsy revealed varying amounts of internal hemorrhage in the viscera and central nervous system. The alveoli of the lungs were almost always found to be to a certain extent ruptured. In the second zone, some animals exhibited similar injuries as in the first zone, but to a lesser extent. Those that died during the blast in this zone exhibited primarily capillary engorgement, especially noticeable in the central nervous system and meninges. Third zone animals exhibited a state of stupor or transitory loss of consciousness in almost all cases. Massive and exaggerated reflex response with rapid fatigue was also noted. Animals that were allowed to recover began to behave in a manner more normal to them, though for a considerable time their conduct, posture and gaits were awkward and abnormal. These animals invariably crouched down as flat as possible and when liberated, made no efforts to run away. It is very interesting to note the similarities described here with animals and those that were described by Mott earlier with wounded soldiers. [22].

Carver and Dinsley additionally reported observations from the third zone involving the Ammunition Proof and Demolition Section staff members who prepared and detonated the munitions. All staff were sheltered in well-protected dug-outs about 100 yards from the explosion. It was found that whereas simple explosive material, such at Trinitrotoluene (TNT), picric acid or 2,4,6-Trinitrophenylmethylnitramine (tetryl) rarely cause the men any discomfort, certain combinations of explosive material, such as ammonal and amatol, lead to complaints of unpleasant physical sensations. These included weakness of legs, violent shaking and increased rate of respiration and pulse. This is the first documentation that not all explosions are the same.

Following World War I, David R. Hooker investigated the effects of blast injury. His experiments, performed at Sandy Hook Proving Grounds, New Jersey, studied the effect of the blast exposure of large-caliber guns used in powder testing on animals. [28] He exposed dogs, cats, rabbits and frogs to the muzzle blast from large-caliber guns used in powder testing. The guns used were 10 and 12 inch rifles and a 12 inch mortar. He found that animals placed ten to twenty feet in front of either the 10 or 12 inch rifles yielded a significant drop in blood pressure following blast, whereas those placed in front of the 12 inch mortar did not. Hooker correctly attributed the pathophysiological abnormalities produced by the cannon's blast to the longer duration of its positive pressure phase. [17] Frequently, animals that were killed exhibited extensive lung injuries.

With the exception of these mentioned investigators, blast injuries faded from the literature for practically the next 15 years. The Spanish Civil War brought a handful of papers of observed cases of blast injury. Notably, Mira [31], who argued from cases seen after air raids in Barcelona, Spain, that the presence of amnesia was a powerful indicator of cerebral injury [21]. But reminiscent of World War I and the debate between either an organic or psychiatric cause, Culpin [32], argued that for many victims, amnesia was the product of an unconscious process designed to block unpleasant memories.

In late1939, Walter Schaller [33], published an article describing the known landscape of head injuries at that time. The observed conditions are manifest from obvious organic causes, such as skull fracture, lacerations, contusion, infections, etc. to observed functional disorders, or commonly called psychiatric disorders, such as post-traumatic psychoneuroses or traumatic hysterias. Schaller proposed a condition that can be observed midway between the two, "post-trauma concussion state". Post-trauma concussion state describes the "disturbance of

consciousness with no immediate or obvious pathologic change in the brain". By 1941, as the intensity of World War II was increasing, a variation of Schaller's condition, now termed "post-concussion syndrome" had caught hold.

The advent of World War II reinvigorated a substantial amount of research into blast wave injuries. With the injuries that were becoming apparent, the problem of blast injuries seemed to be reinvented, first in England in 1940-41 and then in Germany in 1942-43. The earliest WWII paper describing blast effects on a surviving subject was one published by Stewart, Russels and Cone, all officers in the British Army, describing their observation on a pheasant which had developed a state of catatony with flexibilitas cerea after bombs had exploded in a park. [34] Data on soldiers and civilians quickly followed with works by Fulton [35], Abbott [36], Pollock [37], Rodgers [38], Aita and Kerman [39], and Fabing [40]. Cramer, Paster and Stephenson [41] described a number of cases, all with similar outcomes, that came to exemplify the cardinal factors in blast wave injury. As Mott had documented 30 years earlier, patients presented who were subject to nearby explosions with no overt or external harm to the skull, yet were rendered unconscious. All suffered retrograde amnesia with great motor unrest and exaggerated responses to noise or stimuli. On regaining consciousness, intense and intractable headache, which later gave way to a milder, but constant, headache, tinnitus, dizziness, intolerance of noise, tremors and nervousness were observed. At this point, patients who did not recover became progressively worse and frequently died within a couple of days. Gross pathology on selected individuals revealed that the brain suffered massive, non-localized, hemorrhage and significant edema development. The types of pathological lesions described included cerebral edema, petechial hemorrhages, meningeal hemorrhages, cerebral contusion and lacerations, intracerebral hematomas and subdural hematomas.

As following World War I, the fact that a blast wave could induce traumatic brain injury was realized, but the causes were still not solidly established. During and post World War II the arguments shifted to the mechanism by which the brain was injured. Due to the short duration of the blast wave and the ensuing confusion at the scene of the explosion, accurate and objective descriptions were frequently lacking. A number of authors joined in the fray: Denny-Brown [42] thought the probable mechanism was acceleration of the head of the victim to move through a sufficient arc, at a sufficiently great speed and for a sufficiently long moment of time to cause the injury; Stewart, Russel and Cone [34] and Cramer, Paster and Stephenson [41] shared the opinion that the since the late stages were chiefly of brain stem origin, the early manifestations were likewise, requiring that the percussion wave is applied to the body wall and that the force is then transmitted to the cranium via either the venous system or the spinal fluid; and Benzinger and Rössle [43] were convinced that air emboli created the injury.

Following World War II, as after World War I, no clear understanding existed of the effects observed with survivors of blast. A summary Technical Report issued in 1956 [44] described the current state of affairs: "Some psychological effects of blast have detectable physiological changes as concomitants; some do not."

A new device for the study of shock waves began entering the literature in the 1950's. The device was what is known as a shock tube. Shock tubes are long, usually cylindrical tubes, open at one end and closed at the other. An explosive device is placed at the closed end and upon detonation creates a shock wave that travels the length of the tube. As the shock wave travels faster than the resultant air blast from the explosion, the two become separated after some distance and the shock wave may be studied in isolation. If the tube is long enough, the air blast component will die out before it reaches the open end of the tube. Shock tubes were originally

invented in the very late 1890s, but were used almost exclusively for the study of combustion and detonation [45].

Shock tubes have entered the literature as means for inducing injury to animals over the last 40 years, with brain injury only over the last 20. The earliest "modern" blast wave-induced injury research was begun by Ibolja Cernak following her observation of soldiers and civilians during the Balkan war of the middle 1990s [46]. Cernak used a shock tube that was 39 meters long and 1 meter in diameter for inducing whole body trauma.

In the 2000's, Cernak, along with others [47] [48] developed smaller bore shock tubes that were rodent specific. These allowed for a more focused shock wave impact, but still covering the entire body. Some novel modifications were Kevlar jackets or plates with holes sized for the cranium. All of these studies focused on animal behavioral, physiological monitoring or neuroanatomical assessment via sectioning. None correlated the blast wave trauma with MRI measureable parameters.

This study will focus on inducing traumatic brain injury in rodents through a free field blast wave, as opposed to a shock tube, with subsequent imaging of intracranial damage that may be observed with magnetic resonance imaging.

# Chapter II

# Materials

## A. Description of the Blast Device

Detonation of an explosive device creates a blast wave which can injure or kill. Blast waves, as previously described, are produced by the instantaneous conversion of an explosive solid material to rapidly expanding gas. Most studies of blast injury have utilized high explosive, either in the open air or in a blast tube, to create a shock wave for study. These experiments are difficult to carry out in a controlled laboratory environment.

A blast wave generator was constructed following the basic design of Jaffin *et al.* and others, as shown in Figure 2.1. [49]. The generator consists of a pressure reservoir or chamber constructed of brass with approximately 16 cubic centimeters volume. The chamber is fed by a cylinder of compressed air with a maximum pressure of 3600 pounds per square inch (psi). A control valve (Tescom, Elk River, NM) regulates the pressure build-up in the chamber and the pressure is measured directly by a pressure gauge.

A disk, securely mounted below the chamber and just above the base or exit nozzle, ruptures when the pressure in the chamber exceeds the bursting strength of the material. A number of different disk materials are investigated for this study. These materials, Mylar, polyethylene terephthalate (PETG), polycarbonate, and polyvinylchloride, are common polymers that may be commercially purchased (Piedmont Plastics, Charlotte, NC). The sudden rupture of

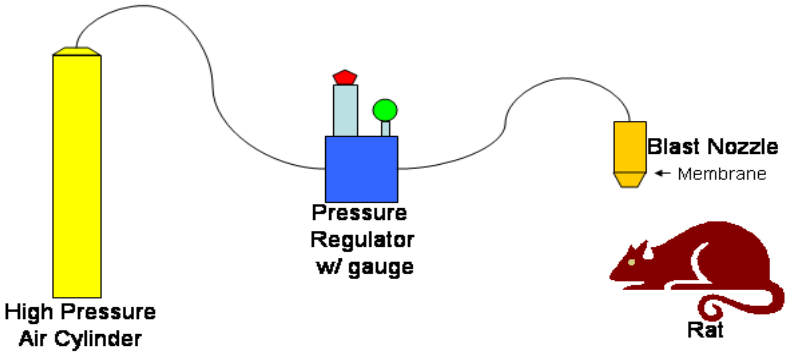


Figure 2.1. Schematic View of Blast Device.

the disk creates a shock wave which exits via the nozzle. The pressure waveform from the blast wave is recorded with a piezoelectric pressure transducer (PCB Piezotronics, Depew, NY) and amplified before being displayed on a digitizing oscilloscope.

The polymer based materials used for the blasting disk are all thermoplastic polymers. Thermoplastic polymers are composed of long chains of high molecular weight polymers. They are chosen due to their unique feature of durability and ease of use. All of these polymers are manufactured in an extrusion process in which bead or chips (called resin) consisting of the chemical structure of each polymer (PETG, PVC, PC) are feed into the barrel of an extruder. The extruder consists of a long screw inside of a cylinder that forces the resin from one end to another while heating and applying pressure along the path of travel. After passing through the barrel, the polymer enters the die for shaping and cooling. For the material used in this study, the die would be rollers for creating sheets of polymer material.

PETG is a variation of the pure polyethylene terephthalate (PET), created by replacing the eythelene glycol with cyclohexane dimethanol in the polymer backbone. Mylar is a biaxially oriented (or orthogonally drawn) sheet of polyethylene terephthalate. The resultant orientation of the polymer chains is responsible for its high strength and stiffness. Polyvinylchloride and polycarbonate are both hard and durable materials that are easily accessible in varying thickness.

Operation of the blast wave generator requires mounting the appropriate disk into the blast nozzle and tightening, through machine threads, the nozzle securely to the chamber. Pressure in the chamber is slowly increased via the pressure regulator knob and the instantaneous pressure in the chamber observed at the gauge. Upon rupture of the disk, the regulator valve is closed again and a new disk may be mounted.

As the pressure in the chambers increases, the unsupported area of the membrane begins to bulge outward. The bulging results from the reorientation of the long polymer chains that make up the material. Whereas, initially the polymer chains might be long, randomly intertwined assemblies, as the stretching progresses the, the chains begin to line up and become parallel to each other. At the point of failure, the material will have been stretched to where no more polymer rearrangement is possible and the only thing left is to break the resilient carbon bonds. The material can then no longer resist the air pressure and a rupture occurs. Because the central area of the bulge will have been stretched to the greatest extent, the membrane material is at its thinnest and ruptures will begin there. The speed and resultant shape of the rupture is determined by the material characteristics.

The rupture is nearly instantaneous and the sudden release of the high pressure air behind the membrane results in the production of a shock wave. The volume of air stored in the chamber prior to bursting, compared to standard atmospheric pressure can be easily determined by the ideal gas law:

$$pV = nRT \tag{2.1}$$

As the gas used for the blast generator is similar in composition to the gas in the lab, nRT may be removed and the equation written as:

$$p_1V_1 = p_2V_2 \tag{2.2}$$

As the bursting pressure will depend on the disk thickness, factors of volume expansion of 1000 to 3000 of the gas in the immediate area of the nozzle will occur. This instantaneous increase, similar to the instantaneous conversion of solid material to a gas as with combustible explosives, will create the front of compression required for the generation of a blast wave.

The pressure generated from the disk rupture is transmitted into the surrounding environment as a radially propagating pressure wave that can attain supersonic speeds.[50] The wave front from the blast device will be of a hemispherical shape, as can be seen in the spark shadowgraph picture acquired by Jaffin *et al.* in Figure 2.2. [49]. The outer circular wave is the blast wave moving outward at supersonic speed. Behind it, emanating directly from the blast nozzle, is a column of turbulent air called the plume, or elsewhere, the air blast. This blast waveform closely resembles that from a gun muzzle. The duration of the blast wave is less than 0.1 millisecond, while the air blast my last multiple milliseconds and can impart significant energy to an object. The air blast is the predominate cause of secondary and tertiary blast injuries.

The pressure wave, both blast and plume, are measured directly with a piezoelectric pressure transducer. The pressure transducer chosen for this work is a PCB Piezotronics, Model 113B22. The transducer is specifically designed for blast wave measurements and applications requiring very high frequency acquisitions. Quartz crystals preloaded in the detector housing generate a charge when compressed by a pressure wave. This design gives the transducers microsecond response time. The high-impedance charge is converted internally in the transducer through a built-in MOSFET microelectronic amplifier to a low-impedance voltage signal. The transducer electronics is powered by a constant-current source and signal conditioner unit (PCB Piezotronics, Model 482C05) that allows interfacing the transducer to a readout device. The measured pressure wave is then read out on a Digitizing Storage Oscilloscope (Hewlett Packard, Model 54505A), from which the waveforms may be saved and/or plotted.

The operation of the pressure transducer is as follows: when the sensor is subjected to a mechanical input, such as the front of a shock wave, a quantity of charge, $\Delta q$, is produced, by the

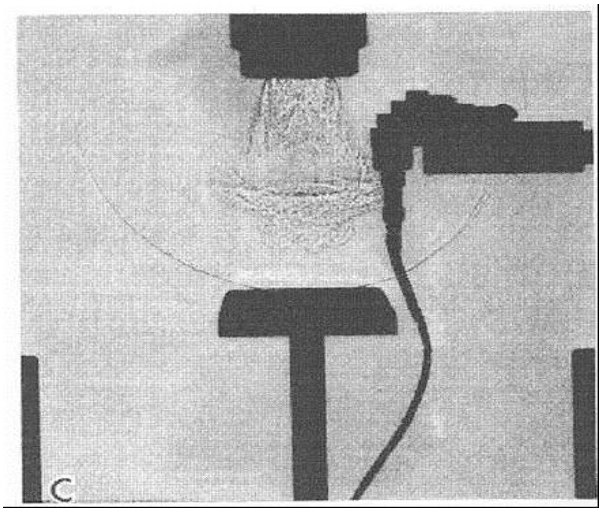

Figure 2.2. Spark shadowgraph Image of shock wave from a free field blast wave device.

compression of the quartz crystals, proportional to the input. The sensor output voltage is then $\Delta V = \Delta q/C$, where C is the total capacitance of the sensing element, amplifier and ranging capacitor; all the components internal to the transducer. The voltage is amplified by the MOSFET amplifier to determine the final sensor sensitivity.

The drawback of capacitive controlled elements is that the signal will decay with a certain time constant that may be described by

$$q = Qe^{(\frac{-t}{RC})} \tag{2.3}$$

where: q = the instantaneous charge (pC)

Q = the initial quantity of charge (pC)

R = the bias resistor value (ohms)

C = total sensor capacitance (pF)

t = time after initial input

e = base of natural log (2.718)

If the time constant, the product RC, is too short, signal may decay while a measurement is being taken from a blast wave. This is particularly important for low-frequency responses, signal inputs that would change slowly in time. The time constant for a PCB sensor is fixed by the various internal components and is measured to be greater than 500 seconds.

The time constant is further modified by the signal conditioning and readout instruments. As mentioned, the pressure transducer is connected to a signal conditioner (PCB Piezotronics, Model 482C05). The signal conditioner has a capacitively coupled output with a time constant fixed by a shunting resistor across the capacitor. These components fix the time constant in the signal conditioner at around 10 seconds, under the condition that the input to the readout device is at least 1 megaohm. The readout device, the oscilloscope, is set with an input impedance of 1

megaohm. The blast wave to be measured will have a duration not exceeding 1 millisecond, therefore the signal loss due to decay within the instruments is inconsequential.

The measured blast waves are defined as either static, dynamic or reflected. The static, or side-on, pressure is measured when the sensing surface of the transducer is oriented parallel to the direction of propagation of the wave. The sensor is thereby unaffected by any kinetic energy in the traveling wave front and measures the air compression that is active in all directions due to the thermal motion of the gas [4]. A precise perpendicular alignment is required to reduce the effect of any refraction of the wave as it crosses the sensor.

If the sensing surface is oriented so that the net motion of the wave front strikes the surface at a perpendicular angle, then the total pressure is recorded. The total pressure will include both the static pressure plus the dynamic pressure. The dynamic pressure is due to the stopping of the net air motion at the sensor surface and is the kinetic energy that is associated with the motion of air particles at the leading edge for the shock wave. The dynamic pressure can be determined as the difference in the readings between two sensors oriented at right angles; side-on and facing the blast wave and is described mathematically as the specific kinetic energy in the flow:

$$p_d = \frac{\rho v^2}{2} \tag{2.4}$$

This is the term that was previously described in equation (1.8).

Finally, when the blast wave encounters a large, solid and immovable barrier, like a wall or the ground, the motion of the gas molecules is impeded. If the barrier is perpendicular to the direction of propagation of the blast wave, the wave is said to undergo a normal reflection. As the blast wave can no longer propagate forward, the molecules are compressed even more by those following, until they are packed so tightly that they push back in the direction of the

incident wave. This even greater concentration of gas molecules that builds up on the surface facing the incident wave is called the reflected region. The reflection process results in a wave which moves in the opposite direction of the incident wave with a nearly identical waveform [4]. In general, the reflected blast pressure is the relevant load imparted to the object and can be several times the incident pressure.

Mathematically, the static and dynamic pressures can be understood as the arrival of the shock front leading to a jump from atmospheric pressure, $P_1$, to the shock-generated pressure, $P_2$. The pressure increment, $P_2$-$P_1$, is termed the side-on, or static pressure. If the shock wave reflects from a rigid surface, the pressure increases from $P_1$ to the reflected pressure $P_5$. The corresponding pressure increment $P_5$-$P_1$ is termed the face-on overpressure. [51]. The dynamic pressure is the difference between the face-on and side-on pressure:

$$(P_5\text{-}P_1) - (P_2\text{-}P_1) \text{ or } P_5\text{-}P_2 \quad (2.5)$$

The difference, $P_5$-$P_2$, is what will be measured with the piezoelectric transducer. This is the maximum potential kinetic energy that could be imparted to the surface of the cranium.

A blast wave occupies a particular place at any given time, and a pressure-measuring device, as described above, placed at a fixed location for a defined period of time can quantitatively describe a blast. As a result, the spatial variation of the wave is translated into a time variation, its pressure-time history and can be seen in Figure 1.1. Characterization of blast wave that may be measured using piezoelectric pressure transducers includes the following observations:

- The finite duration of the nearly instantaneous rise in pressure to its peak value.
- The peak value, the duration and decay of the positive phase of the blast wave as it passes the measuring point.

- The duration and magnitude of the lower than ambient pressure that slowly returns to ambient marking the passage of the negative phase.
- Any following air blast component and it peak value and duration.

These parameters will be measured in the characterization of the blast box.

## B. Description of Nuclear Magnetic Resonance Measurements Techniques

Nuclear Magnetic Resonance (NMR) is based on the fact that the nuclei of many elemental isotopes possess spin angular momentum and an associated magnetic moment. The nucleus is comprised of protons and neutrons and each possess a certain magnetic moment. The magnetic moments combine in a phenomenon known as pairing whereby the constituent protons and neutrons determine the nuclear magnetic moment. Because the magnetic moments of the neutron and the proton are almost equal in value, but of opposite sign, only those nuclei with dissimilar numbers of neutrons and protons will generate a non-integer magnetic moment. Classically, this magnetic moment may be viewed as a bar magnet with north and south poles. Thermal energy will randomize the orientations of these magnetic moments, so no bulk magnetization is measurable. When these nuclei are placed in a static magnetic field, they assume a number of quantized orientations. Most nuclei of interest for *in vivo* NMR have a nuclear spin quantum number, I, of one-half and hence exist in either one of two energy levels as shown in Figure 2.3.

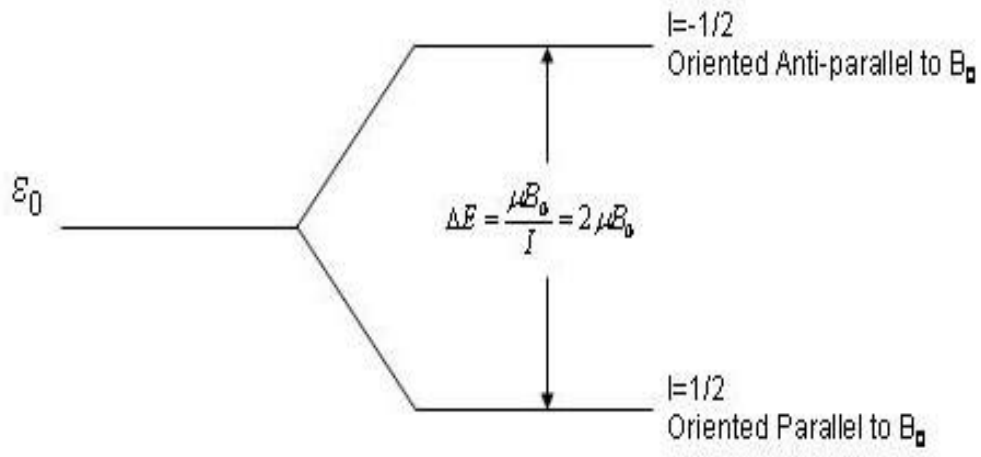


Figure 2.3. Magnetic Energy Levels of a Spin ½ Nucleus

These levels consist of a "lower" energy state in which the nuclear magnetic moments are aligned parallel with the external field, and a "higher" energy state, in which the moments are aligned anti-parallel to the field. A slight excess of nuclear spins will exist in the lower energy state relative to the higher energy state, the number of which is determined by the thermal energy of the sample.

In addition to the energy separation of the spins, the spinning protons will experience a torque from the applied magnetic field that will cause precession, much as a spinning gyroscopic top precesses in a gravitational field. This precession or "angular frequency of rotation" is directly related to the static magnetic field ($B_0$) by the Larmor equation

$$\omega_0 = \gamma B_0 \tag{2.6}$$

where $\gamma$ is the gyromagnetic ratio, a unique constant for each nuclear magnetic isotope, and $\omega_0/2\pi$ is the resonant or Larmor frequency. The gyromagnetic ratio for the proton nucleus is 42.58 Megahertz per Telsa.

In order to induce transitions from one energy state to another, a second magnetic field, oscillating with the Larmor frequency, is briefly applied perpendicular to the static field. This is normally accomplished using a pulse of radio wave energy, since the Larmor frequency for nuclei precessing in typical laboratory magnet fields falls within the radiofrequency portion of the electromagnetic spectrum. Only radio waves at the Larmor frequency will induce nuclear energy absorption. The nuclei undergo transitions in both directions due to the two energy levels, but due to the excess of spins in the lower level, a net absorption of energy will exist. The nuclei excited to the higher energy state may now relax to the lower state, either through re-irradiations of the absorbed energy or some other relaxation process involving the associated

lattice and/or neighboring spins. It is the irradiated signal, arising from the transverse magnetization, $M_{xy}$, which is observed by the NMR apparatus.

The NMR apparatus consist of a number of separate devices, some controlled by a central processing computer. The main component is a high field, highly homogeneous, magnet. The magnet of interest for this research is a 2.4 Tesla, superconducting unit. The unit's horizontal bore is ideal for small animal work used in following the time course and severity of TBI.

Added into the horizontal cylindrical bore of the magnet, is a set of room temperature coils that are used to further homogenize the magnetic field. These coils are called the shim coil set and consist of 13 separate windings of various shape on a cylindrical former. The goal of the adjustment of these coils is too manipulate the magnetic field at the center of the magnet to make the magnetic field lines as homogeneous as possible. An additional set of three orthogonal room temperature coils, that are also used for shim control, are called the gradient coils. In a standard cylindrical magnet, the direction along the bore is termed the z-axis, the left-right direction, the x-axis and the top-bottom direction, the y-axis. [52] Although the gradients are oriented in the three orthogonal directions, the gradient magnetic fields themselves are parallel to the main magnetic field, $B_0$. The null point at the center of the gradient coils, and also the center of the magnet, is called the iso-center. Gradient amplifiers generate the electric currents and voltages that need to be applied to the coils to produce the pulsed-gradient magnetic field required for NMR imaging.

The radiofrequency (rf) system consists of the components required to generate, shape and apply a burst of rf energy at the Larmor frequency to the spin. The rf energy that is then re-irradiated as the spins decay from one energy level to the other is then received, de-encoded and digitized. Hardware needed for the transmission of rf energy are the frequency synthesizers, the

rf power amplifier and the rf coil. rf energy reception is performed from the rf coil, pre-amplifiers, receiver, and digitizer. The rf coil, like the shim and gradient coils, is in the shape of a cylinder and concentrically placed inside the gradient coil set. These primary components are shown in Fig. 2.4.

An MR image consists of a number of discrete voxel elements, each one defined by the calibrated magnetic gradients field created by the gradient coils in the three orthogonal axes. Because the coils set up a gradient magnetic field in their respective planes, the resonance of the nuclear spins will change in accordance with the equation:

$$\omega_z = \gamma(B_0 + zG_z) \tag{2.7}$$

Where, $G_z$ is the strength of the gradient field in Gauss per centimeter applied along the z-direction. An rf pulse of energy, applied at the specific $\omega_z$, will allow for nuclear excitation and data reception from spins meeting the requirements of the imaging parameters.

As can be seen, a nearly infinite number of options may be applied for imaging multiple slices, orientations, etc. through the judicious selection of gradient magnetic field and rf excitation frequencies. Imaging protocols of importance that will be used in this research will involve the so-called $T_1$ and $T_2$ weighted, diffusion weighted and inversion-recovery sequences.

The simplest of all imaging protocols are the $T_1$ and $T_2$ weighted sequences. $T_1$ and $T_2$ are fundamental properties of nuclei in a magnetic field. Following rf excitation, the nuclear magnetic moments are in a higher energy state, as described above, and are aligned parallel to each other. The $T_1$ relaxation mechanism is the loss of the extra energy from the spin system due to the surrounding environment or lattice. It is commonly known as spin-lattice relaxation. For nuclei to undergo this relaxation mechanism, an external stimulating magnetic field is required. This is provided by the magnetic moment of neighboring nuclei or molecules. Because the

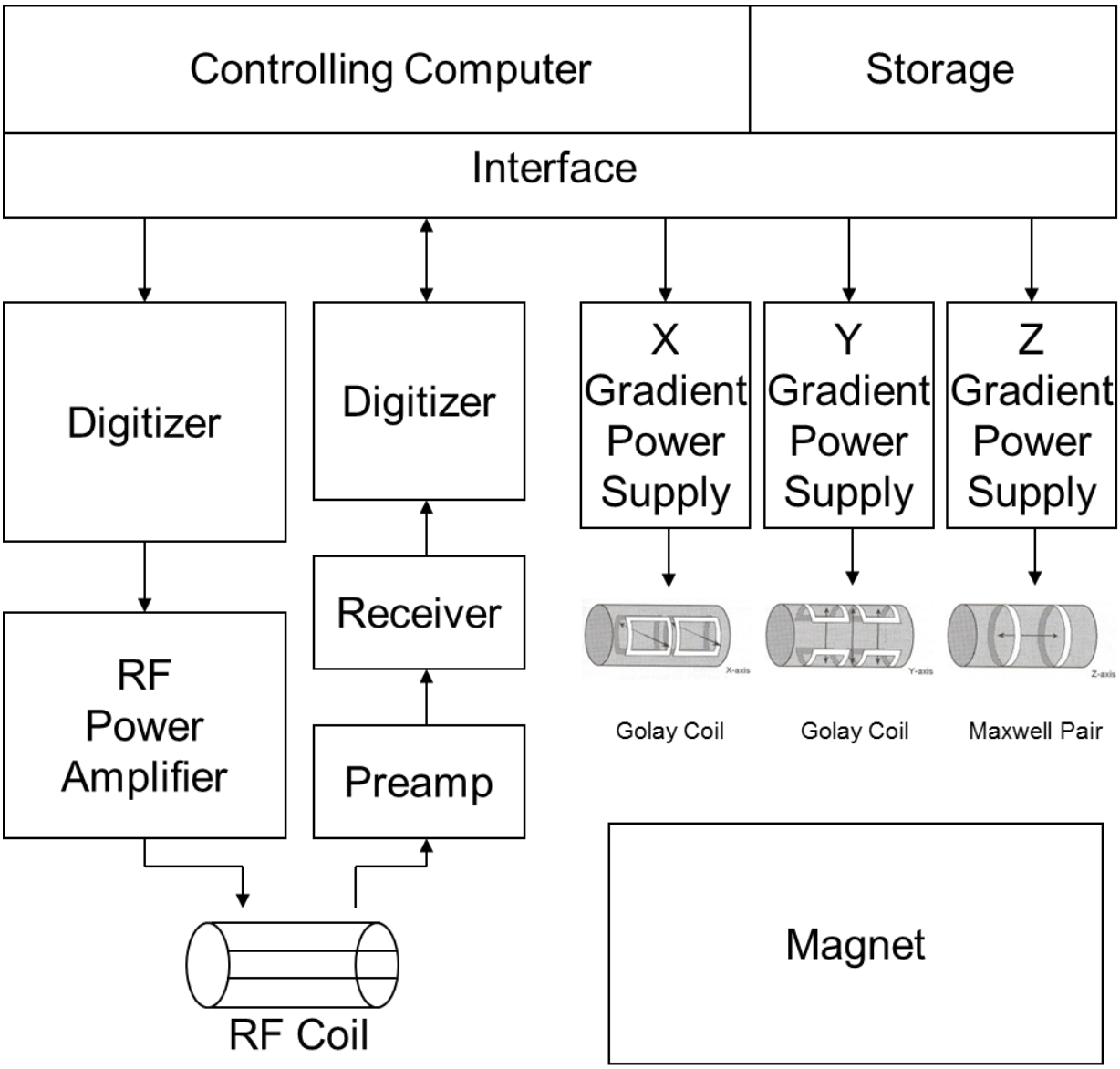


Figure 2.4. NMR Apparatus Component Layout

excited nuclei are precessing at the Larmor frequency, the fluctuations that they observe need to be at this frequency to induce transitions. As proton nuclei may range from being rigidly bound in hydration layers to freely mobile in aqueous solutions, therefore, a wide range of tumbling frequencies are possible. The predominate binding state of the assembly of nuclei will determine its characteristic $T_1$ relaxation time [52].

The $T_2$ relaxation mechanism involves a dephasing of the spin system that begins immediately after the end of the excitation rf pulse. A common technique for MR scientist is to consider the nuclear spin system from the rotating frame reference. An observer traveling with the rotating spins that have just been put into phase due to the rf pulse, would witness spins that are experiencing a slightly higher local magnetic field accelerating and pulling ahead of the assembly, while those that experience a slightly lower field would be slowing down. Anything that can change a spin's frequency from the Larmor frequency will add to this dephasing. As soon as the variant magnetic field is removed from the nuclei, they will return to the Larmor frequency, but will maintain the induced phase shift. This discrepancy will compound over time until the spins vectors are completely random. The dominate effect for causing dephasing is the inhomogeneity in the main magnetic field. Great care is taken to reduce this inhomogeneity by "shimming" the magnetic field around the sample to be studied. A second effect is the fluctuation experienced by the nuclei in the local magnetic field as the spins move around within the tissue or other medium. It is this interaction that is called the spin-spin relaxation and characterized by the spin-spin relaxation time, $T_2$. $T_2$ is strongly dependent on the density of the local medium or tissue and the presence of any strongly magnetic substance [52].

The $T_1$ and $T_2$-weighted imaging protocol take advantage of acquisition parameters that may highlight either of these two properties. Both protocols employ a standard spin-echo

excitation regime as shown in Fig 2.5. The rf power is applied first to excite the nuclear spins and then to refocus any dispersion that occurs in the spin vectors. This is accomplished through the $90^0$ and $180^0$ rf pulses, respectively. Gradients, called slice-select gradients or $G_{Slice}$, applied with these rf pulses, localize the nuclear excitation to a pre-defined slab. A phase-encoding gradient, $G_{PE}$, applied in an orthogonal direction between the two rf pulses produces a positionally dependent phase shift along the gradient direction. The phase-encoding gradient is systematically stepped through values from +M to –M. Finally the frequency-encoding gradient, $G_{Read}$, orthogonal to the slice-encoding and phase-encoding gradients, allows acquisition of all the spatial frequency information that is needed from one MR signal following rf excitation [52].

In practice, for the $T_1$-weighted acquisition, a short time delay is chosen between the $90^0$ excitation pulse and the data acquisition (with the $180^0$ refocusing pulse being directly in the middle), along with a short sequence repetition time. This allows for enhancement of signals that decay quickly, and provides a high contrast image for anatomical identification. The $T_2$-weighted sequence imposes a substantially longer delay between the $90^0$ pulse and the acquisition and a sequence repetition time long enough so $T_1$ contrast is masked. A $T_2$-weighted sequence will highlight tissue that have a long $T_2$ relaxation time, such as water, cerebrospinal fluid or edema. These protocols will be employed in this study to: localize anatomical structure both for identification and for setting up the voxel localized spectroscopy (to be discussed below) and to allow a qualitative view of edema development.

A second imaging protocol to be employed is diffusion weighted imaging (DWI) and the calculation of quantitative Apparent Diffusion Coefficient (ADC) and Fractional Anisotropy (FA) maps. In DWI the overall effect observed in a voxel reflects the displacement distribution of water molecules [53]. The water mobility, called “Brownian Motion”, is the random motion

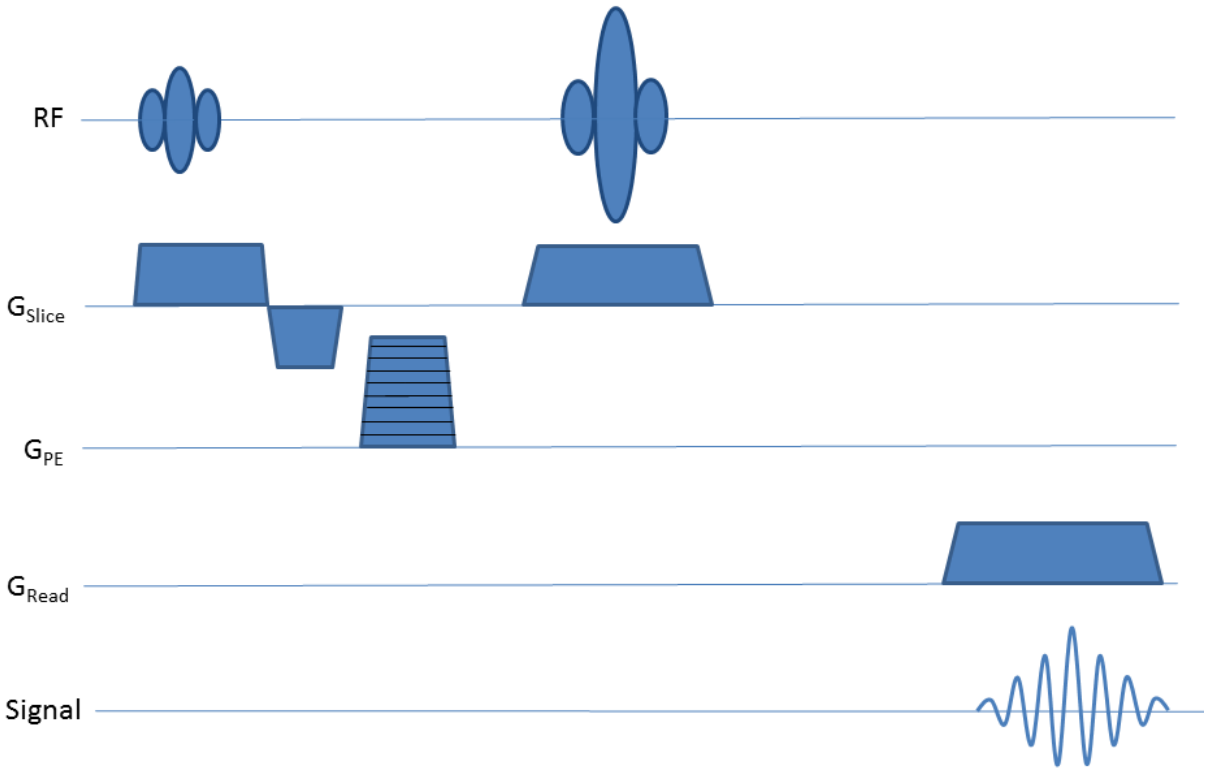


Figure 2.5. Spin Echo Pulse Sequence

of molecules within a sample. The rate of diffusion depends on the kinetic energy and temperature of the molecules and their environment. In biological tissues, this diffusion is not truly random due to the cell membranes, vascular structure and axonal pathways. Therefore, in the brain, water diffusion is referred to as an "apparent diffusion".

DWI measures this apparent mobility or diffusion of water molecules by the addition of diffusion sensitizing gradients that are placed on both sides of the $180^0$ refocusing pulse. The first diffusion gradient de-phases the spins, while the second one, symmetrically placed around the $180^0$ pulse, re-phases the spins to their initial state, provided no net motion has occurred. If net motion of the spins has occurred, the signal is attenuated, with the degree of attenuation dependent on the magnitude of molecular translation and diffusion weighting. The amount of diffusion weighting is determined by the diffusion gradient amplitude, duration and time between the gradient. This weighting factor is commonly called the "b-value', and is mathematically stated as:

$$b = \gamma^2 G^2 \delta^2 (\Delta - \frac{\delta}{3}) \tag{2.8}$$

Where G and δ are the gradient amplitude and duration, respectively and Δ is the time interval between the two diffusion gradients. b has the units of seconds/millimeters$^2$. In the presence of a gradient with amplitude G, molecular diffusion attenuates the MRI signal by the exponential equation:

$$S = S_0 e^{-bD} \tag{2.9}$$

Where S and $S_0$ are the voxel signal intensities with and without diffusion, respectively, and D is the diffusion coefficient along the applied direction.

To calculate a simple ADC map, a minimum number of two DW images must be acquired, one with b=0 and one with b≠0. The limitation here is that only diffusion along the

direction of the diffusion gradient is highlighted. For anisotropic tissue, as encountered in biological environments, this can result in a serious underestimation of the molecular diffusion. In the more general case the diffusion properties are described by a tensor [52]. The diffusion tensor has at minimum nine values, each corresponding to a gradient and cell orientation. The diffusion tensor is:

$$D = \begin{pmatrix} D_{xx} & D_{xy} & D_{xz} \\ D_{xy} & D_{yy} & D_{yz} \\ D_{xz} & D_{yz} & D_{zz} \end{pmatrix} \tag{2.10}$$

The first subscript refers to the natural orientation of the cells or tissue, and the second refers to the gradient direction. The on-axis orthogonal elements are most straight-forward to understand, as they employ only the laboratory defined x, y and z gradients for diffusion sensitizing. The tensor elements $D_{xx}$, $D_{yy}$ and $D_{zz}$ are known as the characteristic or eigenvalues of the matrix. The sum of the three eigenvalues is called the Trace of the diffusion tensor:

$$Tr(D) = D_{xx} + D_{yy} + D_{zz} \tag{2.11}$$

The Trace equation enters the voxel signal intensity equation (2.9) by replacing D:

$$S_{xyz} = S_0 e^{-b(D_{xx}+D_{yy}+D_{zz})/3} \tag{2.12}$$

Where the average diffusion is defined as:

$$D_{avg} = \frac{D_{xx} + D_{yy} + D_{zz}}{3} = \frac{Tr(D)}{3} \tag{2.13}$$

An image generated using equation (2.12), is routinely referred to as a Trace image.

The off-axis elements are vector sums of the three primary axes. Due to the redundancy in the matrix, only six images, plus an un-weighted, b=0, need to be acquired. Once the eigenvalues are known, a number of additional diffusion parameters can be produced [54]. The

most sensitive and useful of these is the Fractional Anisotropy (FA), which represents the fraction of the magnitude of the Diffusion Tensor that may be ascribed to anisotropic diffusion [55]. It is a measurement that reflects the directional orientation of structure within the brain and may be calculated from the Tensor elements and the Trace by the equation:

$$FA = \sqrt{\frac{3}{2}} \frac{\sqrt{(D_{xy} - Tr(D))^2 + (D_{xz} - Tr(D))^2 + (D_{yz} - Tr(D))^2}}{\sqrt{D_{xy}^2 + D_{xz}^2 + D_{yz}^2}} \tag{2.14}$$

As the standard spin-echo sequence requires a long acquisition time (on the scale of minutes), a diffusion tensor acquisition can become intolerably long. To this end a spin-echo, echo-planar imaging sequence is used. A diffusion weighted echo-planar pulse sequence, as shown in Fig 2.6, is similar to the spin-echo sequences described above, with the first notable difference that the phase-encoding gradient follows the $180^0$ refocusing pulse. More significantly though, both the phase and read gradients are rapidly applied and a number of phase encoding steps are acquired for each spin echo excitation. This is commonly called a "Blipped" echo-planar acquisition.

Spin-lattice relaxation, as explained above, is a fundamental property of MRI and will be the third NMR imaging routine to be employed in this study. $T_1$ measurement protocols involve the use of a so-called inversion-recovery MR acquisition sequence, as shown in Fig 2.7. A radio frequency pulse designed to invert the net magnetization, commonly called an inversion pulse, is applied at the beginning of the sequence, followed by either a spin-echo or, more commonly, a spin-echo echo-planar acquisition to acquire the image. The delay between the inversion pulse and the spin-echo excitation is varied to allow recording of the magnetization at different time points as it returns to the ground state. The resultant images may be post processed through linear regression to yield a $T_1$ map image, in which each pixel represents a quantitative value (in

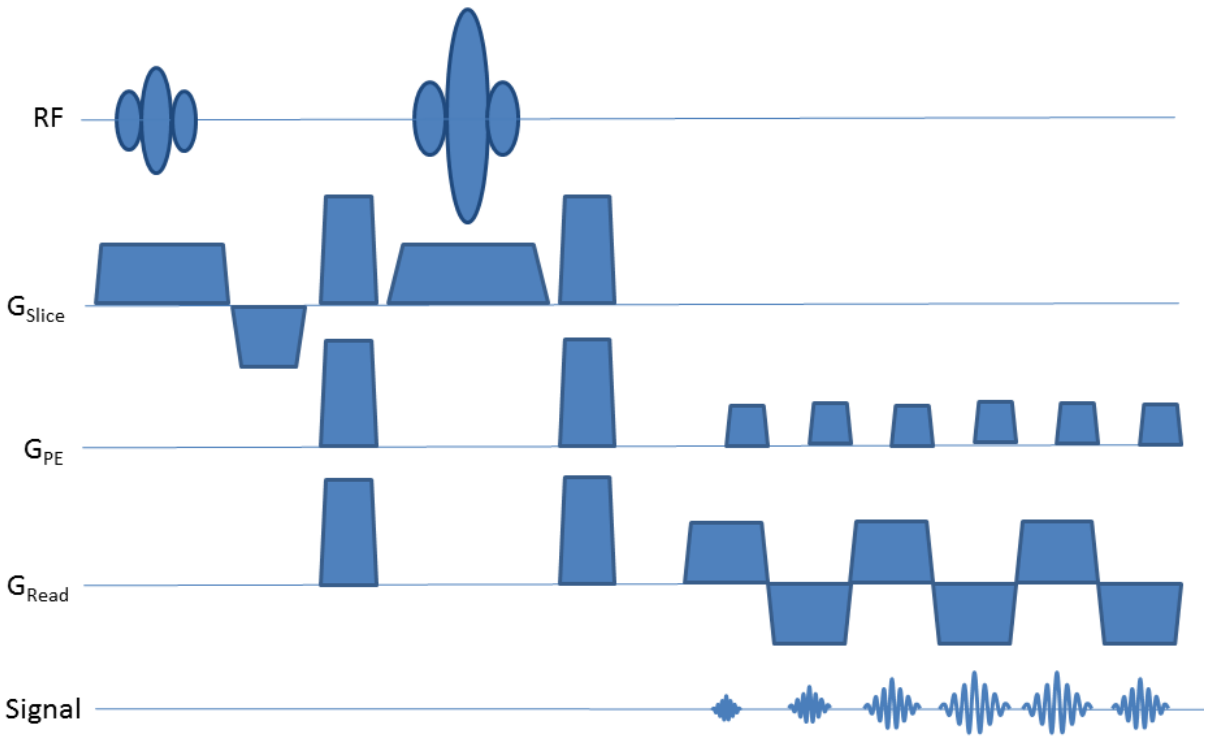


Figure 2.6. Diffusion Weighted Spin-Echo Echo-Planar Pulse Sequence

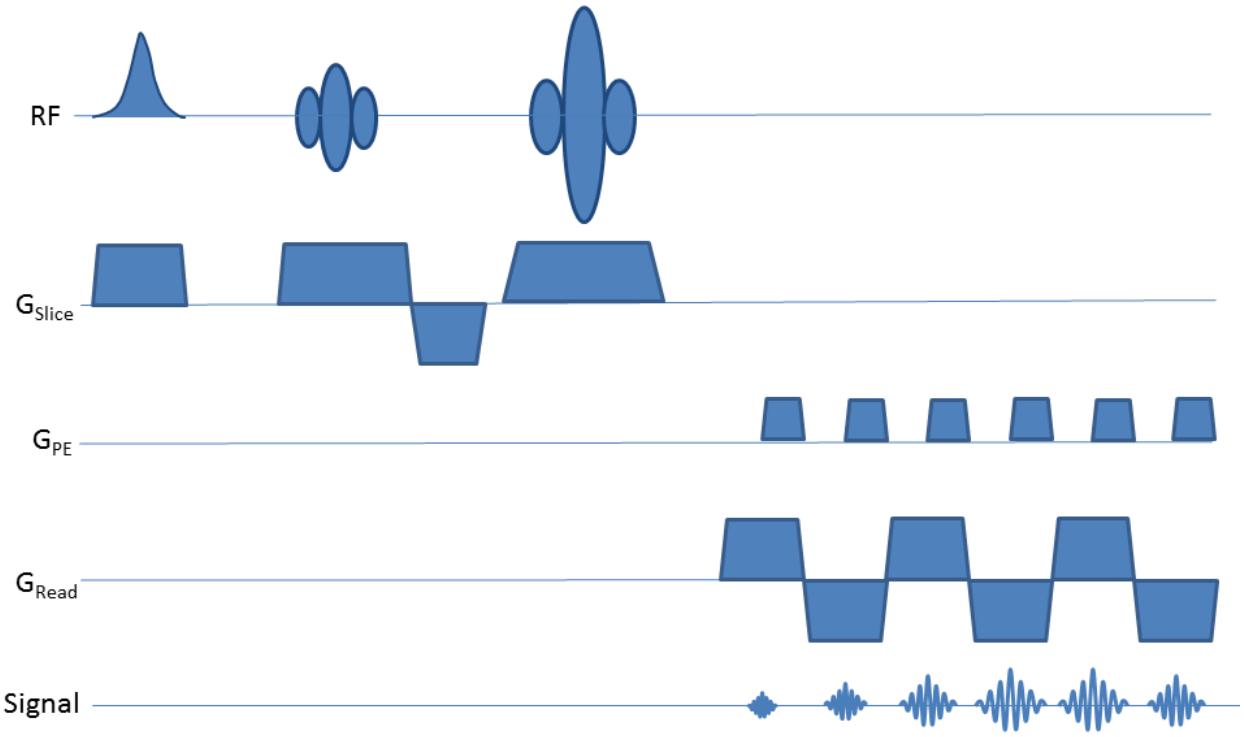


Figure 2.7. Inversion-Recovery Spin-Echo Echo-Planar Pulse Sequence

seconds). A further numerical relationship exists between the $T_1$ map and a map based purely on brain water content, W [56]. As this relationship is magnetic field strength dependent, for the MRI system to be used in this study, the equation is:

$$\frac{1}{W} = 0.907 + \frac{0.407}{T_1} \tag{2.15}$$

The units of brain water content are in percent water.

An additional measure of the physiological state of the brain may be determined, again non-invasively, through the use of Proton ($^1$H) Magnetic Resonance Spectroscopy (MRS). MRS is a useful tool for detecting signal from cerebral metabolites, which are present in the tissues, at concentrations not exceeding a few tens of millimols. The metabolic effects of TBI are known to be quite complex, affecting to different degrees a number of cerebral compounds. It is thus necessary to identify the most relevant changes describing the cerebral metabolic status at different time points post injury [57]. For MRS to be carried out in this study, three predominate peaks will be identified and followed over the time course. These are N-acetylaspartic acid (NAA), creatine/phosphocreatine (Cr), and choline-containing compounds (Cho). Additional minor peaks, that may be observed as the MRS signal resolution allows, are myo-inositol (Ino) and S100B [58]. NAA, in particular, being almost exclusively localized in neurons, is considered a marker of neuronal damage caused by diffuse axonal injury, or TBI. NAA is generally found to decrease following TBI, with the degree of reduction dependent on the severity of injury and may be reflective of neuronal cell death. A reduction in NAA can be a transient, reversible phenomenon reflective of mitochondrial dysfunction. If the injury is prolonged, irreversible damage may follow ultimately leading to neuronal loss. NAA changes have been correlated with outcome. In experimental models of diffuse axonal injury, NAA loss is found to be in direct correlation with the brain energy state showing identical ATP profiles

[59]. Hence, a direct link exists between mitochondrial function and the ability to synthesize NAA as assessed by oxygen consumption and ATP synthesis. Choline, a marker for cell membrane disruption, is elevated in gray matter after injury.

MRS may be measured with a so-called PRESS MR technique. Point-RESolved Spectroscopy (PRESS) is based on a spin-echo pulse sequence and is shown in Fig 2.8. A $90^0$ rf pulse is followed by two $180^0$ rf pulses so that the primary spin echo is refocused twice. The first echo contains the signal from a line which is the intersection between the two orthogonal planes selected by the $90^0$ pulse and the $180^0$ pulse. The second echo contains only the signal from the intersection of the three planes selected by the three pulses, resulting in a cube; this is the signal that is collected. Signal from outside the cube does not experience the refocusing pulses and theefore rapidly dephases [60].

Image processing of the diffusion weighted and inversion-recovery data sets will take place on a Sun Workstation using the MRVision software (MRVision Co, Winchester, MA). Spectroscopic data will be analyzed on the Bruker Biospec, using the WinNMR software.

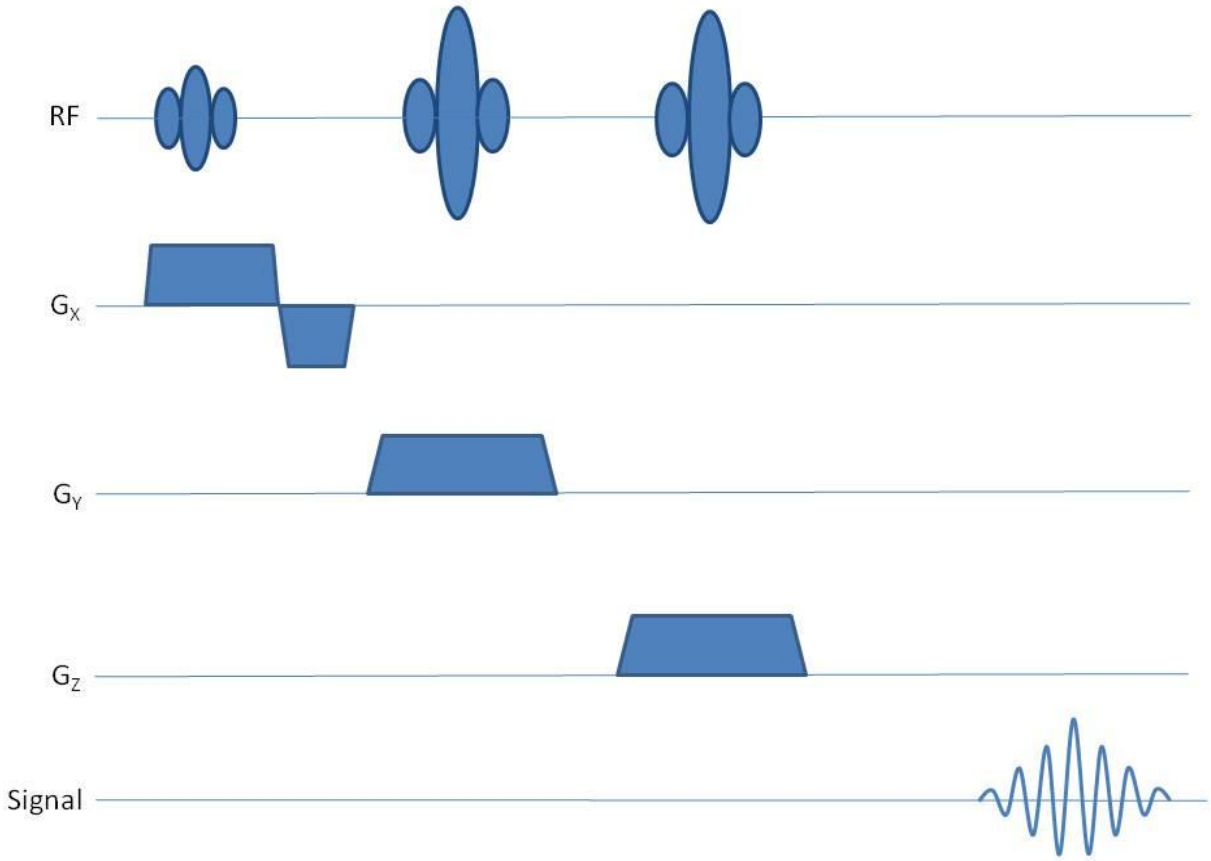


Figure 2.8. PRESS Localized Spectroscopic Sequence

# Chapter III

# Measurements

## A. Blast Wave Device Measurements

The blast wave device was constructed at VCU with the help of the Custom Design and Fabrication Machine shop. The final unit is as described above and shown in Figures 3.1 and 3.2. Testing of the blast wave device involved numerous blast exposures with measurement and recording of the data from the piezoelectric pressure transducer. Data measured from the shock wave produced by each blast included: the maximum positive pressure peak, the rise time to maximum pressure, the fall time from maximum to ambient pressure, the maximum negative pressure, the duration of the negative pressure phase, and the potential existence of an air blast plume. As described earlier, these were all measured and documented with the PCB piezoelectric pressure transducer, PCB signal conditioner and the Hewlett-Packard digitizing storage oscilloscope. Values were recorded in a Microsoft Excel spreadsheet for comparison and analysis.

Because a quantitative photographic image of the blast is impossible with our current setup, data must be acquired by repetitive blast explosions measured spatially over the expected area of the blast wave. The two general components of the blast wave are readily measured with our current measurement setup. As was described earlier regarding Figure 2.2, the blast pulse emanating from the nozzle contains both a radially progressing shock wave and an air blast plume exiting linearly from the nozzle opening. These are both recorded by the piezoelectric

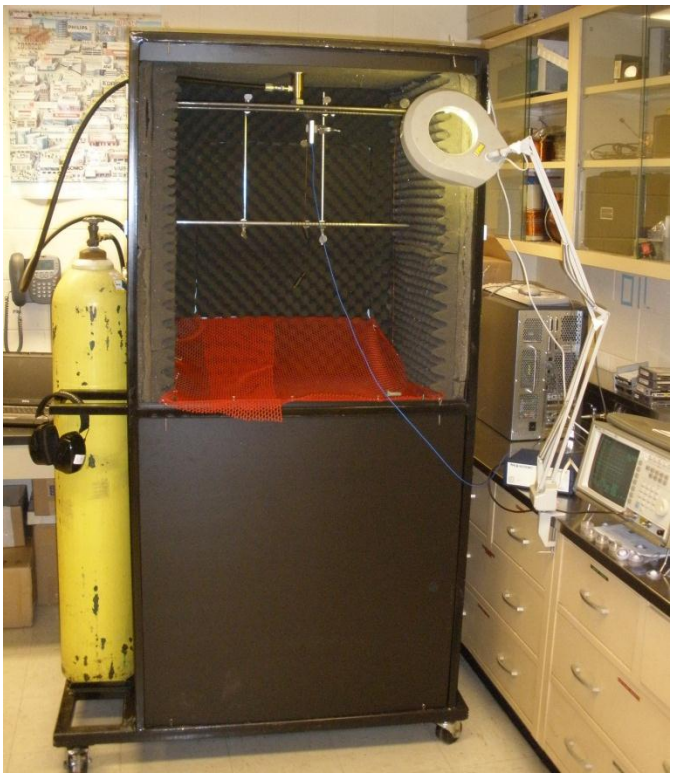

Figure 3.1. Blast box

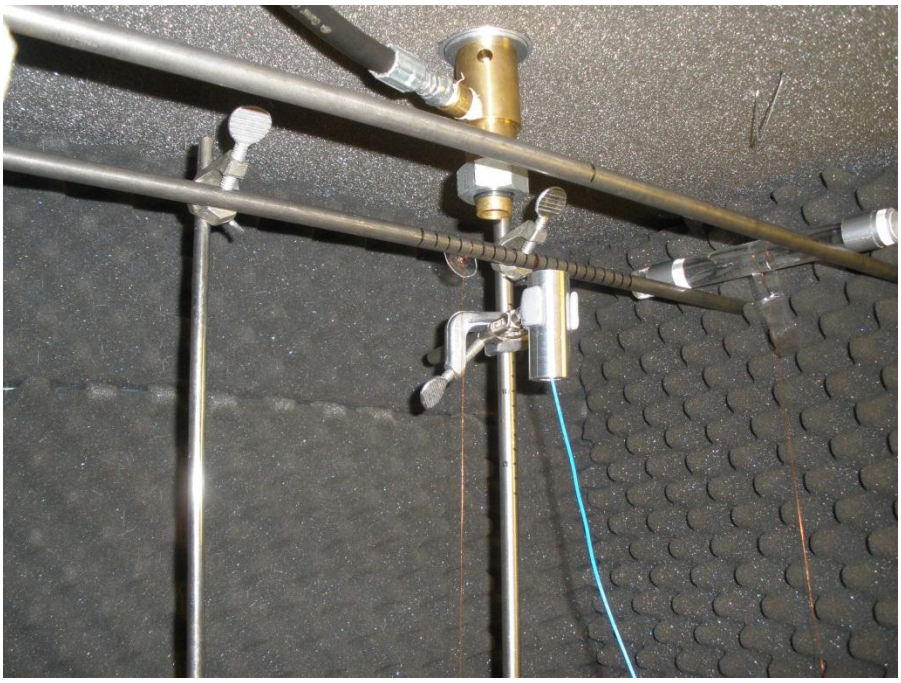

Figure 3.2. Blast Nozzle with support rods and Piezoelectric Transducer

pressure transducer. Figures 3.3 and 3.4 show transducer recordings from two different locations in the blast wave that highlight each of these components. The shock wave only recording, Figure 3.3, is very well described by the Friedlander wave described earlier. As the pressure transducer is positioned closer to the central axis of the blast nozzle, the air blast plume becomes more prominent. The air blast, as shown in Figure 3.4, is an additional and confounding component that follows the shock wave. Measurements have shown that this plume pressure amplitude may greatly exceed the shock wave pressure amplitude. It is currently hypothesized that optimal blast induced traumatic brain injury will result from the shock wave only, with the air blast functioning more as a blunt force trauma mechanism.

At each measurement point the piezoelectric sensor must be positioned using visual landmarks. The transducer is supported between rods that run horizontally across the blast box. Two rods are placed 8 centimeters on either side and slightly above the blast nozzle and a third rod is placed 33 centimeters below one of these. The upper rods can be seen in Figure 3.2. The rods were marked in 10 mm distance increments from the center of the nozzle. A section of fine magnetic wire, under tension, was hung from one of these support rods and using the markings was positioned directly in front of the center of the nozzle. This wire then becomes the central axis, or 0 mm, off-axis of the blast nozzle. With this wire at the 0 mm offset, the transducer could be positioned with the aid of a mechanics ruler at the desired offsets (x and y-coordinate) to be studied. Likewise, the mechanics ruler could be used to extend and visualize the transducer axis, to ensure that the face of the transducer is always perpendicularly aligned with the center of the blast nozzle. These two adjustments usually needed to be repeated a number of times to fully align the transducer at a particular point, as adjustment of the transducer angle from horizontal,

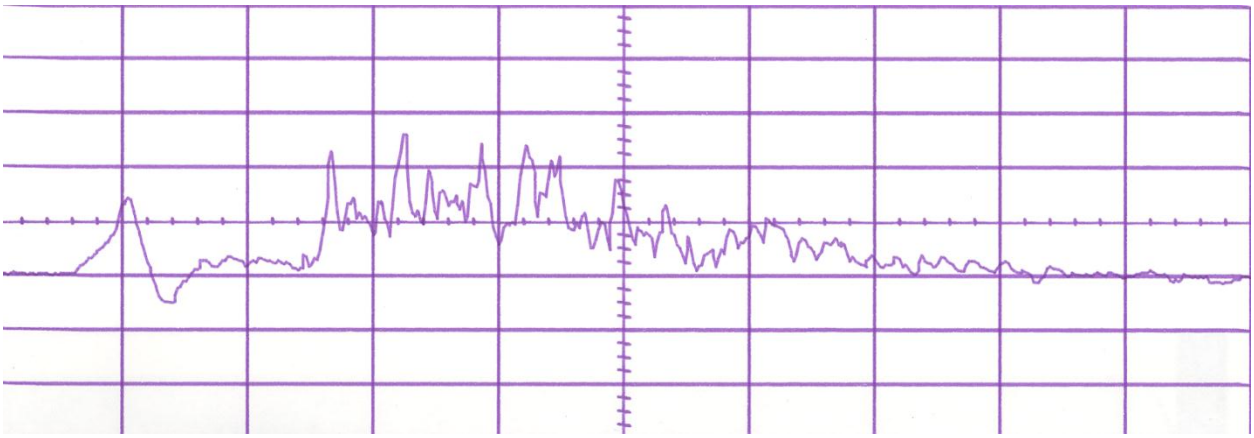

Figure 3.3. Shock Wave Measured from Blast Device.

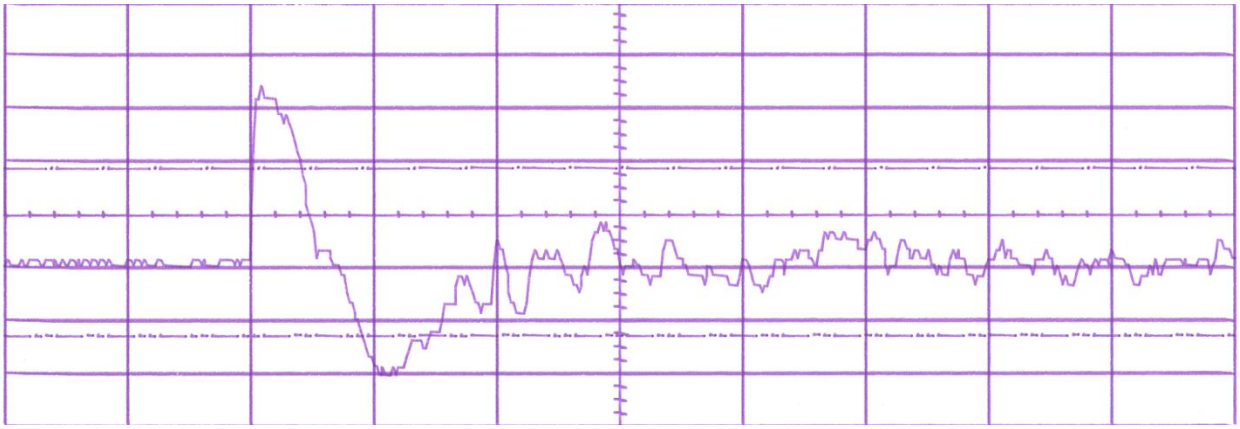

Figure 3.4. Shock Wave with following Air Blast Measured from Blast Box.

changes the distances from the blast nozzle along the x andy  axis and *vice versa*.  Likewise, adjustment of the x and y position, affected the angle.

Measurements at each point involved loading the membrane material and securing the blast nozzle to the blast chamber.  Initial testing with these materials involved a basic understanding of the rupture pressure of single and multiple layers of membranes.  The membrane material used and the thickness of the membrane greatly influences both the bursting pressure in the chamber, shock wave maximum pressure, and the occurrence of a measureable air blast wave at some point off axis from the nozzle.  At very thin total thicknesses, a membrane would rupture at such a low nozzle pressure as to make shock wave measurements meaningless. From previous, non-optimized work performed with the blast nozzle and animals, it was decided that a bursting pressure of >1500 psi would be required.  For the specific purpose of mapping out the shock wave resulting from the blast explosion, the materials listed in Table 3.1 were used.

Table 3.1.  Membrane Material Thickness used for testing Blast Device.

| Material | Disks Used (inches) | Total Thickness (inches) |
|---|---|---|
| Mylar | 0.014, 0.014 + 0.005, 0.014+0.005+0.005 | 0.014 or 0.019 or 0.024 |
| Polycarbonate | 0.030, 0.030 + 0.010 | 0.030 or 0.040 |
| PETG | 0.030 + 0.030 | 0.060 |
| PVC | 0.030 + 0.030 | 0.060 |

Before fully characterizing the shape and intensity of the shock wave, and determining the optimal polymer based material for the blast disks, some initial questions must be addressed. The most fundamental question is that of the reproducibility of the polymer material to rupture at the same chamber pressure and to yield a shock wave that offers similar pressure characteristics

as measured at a fixed point. The pressure transducer may be secured at a fixed location through the support mechanism described earlier. A fixed distance down from the opening of the nozzle, chosen to be the y-axis, and a fixed distance perpendicular to the central axis of the nozzle, chosen to be the x-axis, is selected. As mentioned above, to reduce complexities of the waveform measurement, only a pure shock wave should be recorded, with no contribution from the associated air blast. Preliminary measurements showed that a distance of 50 mm down and 50 mm off-axis fulfilled this requirement.

For each material, 6 or more blast repetitions were performed. The maximum amplitude and duration of the shock wave was recorded. Additionally, the magnitude and duration of the negative phase of the wave was noted. For the materials and respective thicknesses listed in Table 3.1, the measured shock wave parameters are listed in Table 3.2

What is readily apparent is the wide range in the maximum shock wave pressure from the different membrane materials. This relates directly to the structure and the chemical bonding of the polymer chains. Obviously, as a maximal shock wave pressure is desirable for inducing injury and chamber pressure is limited by the native pressure in the high-pressure air cylinder, PETG and PVC are less desirable materials for performing this work.

Because each membrane consists of a different chemical formulation or mechanical processing (such as Mylar), it can be accepted that along with having different maximum bursting pressures, the methodology by which the membranes burst could be slightly different. This is best illustrated in Figure 3.5, where typical ruptured disks from the four different materials are shown. PETG and PVC exhibit similar rupture patterns: the bulging of the material in the nozzle to a point of failure with a small opening for the compressed air to escape. The small size of the opening is perhaps due to the relatively great thickness of the material required

Table 3.2. Measured Shock Wave Parameters for Different Membrane Material

| Material | Mylar | Polycarbonate | PETG | PVC |
|---|---|---|---|---|
| Thickness (in.) | 0.019 | 0.030 | 0.060 | 0.060 |
| Chamber Pressure at Bursting (psi) | 1900 | 1700 | 1700 | 1400 |
| Positive Phase | | | | |
| Mean Maximum Positive Pressure (psi) | 15.3 | 15.8 | 8.2 | 4.3 |
| Standard Deviation (psi) | 1.5 | 0.9 | 0.4 | 0.2 |
| Coefficient of Variation | 9.8 | 5.9 | 4.4 | 5.7 |
| Duration of Positive Phase | | | | |
| Mean Duration (sec) | 0.060 | 0.060 | 0.052 | 0.083 |
| Standard Deviation (sec) | 0.008 | 0.007 | 0.003 | 0.011 |
| Coefficient of Variation | 13.5 | 12.3 | 5.6 | 12.8 |
| Negative Phase | | | | |
| Mean Maximum Negative Pressure (psi) | -7.8 | -7.8 | -3.7 | -2.7 |
| Standard Deviation (psi) | 2.3 | 1.2 | 0.7 | 0.5 |
| Coefficient of Variation | 30.1 | 15.5 | 18.9 | 19.4 |
| Duration of Negative Phase | | | | |
| Mean Duration (sec) | 0.744 | 0.766 | 0.361 | 0.154 |
| Standard Deviation (sec) | 0.036 | 0.049 | 0.009 | 0.033 |
| Coefficient of Variation | 4.8 | 6.4 | 2.4 | 21.5 |

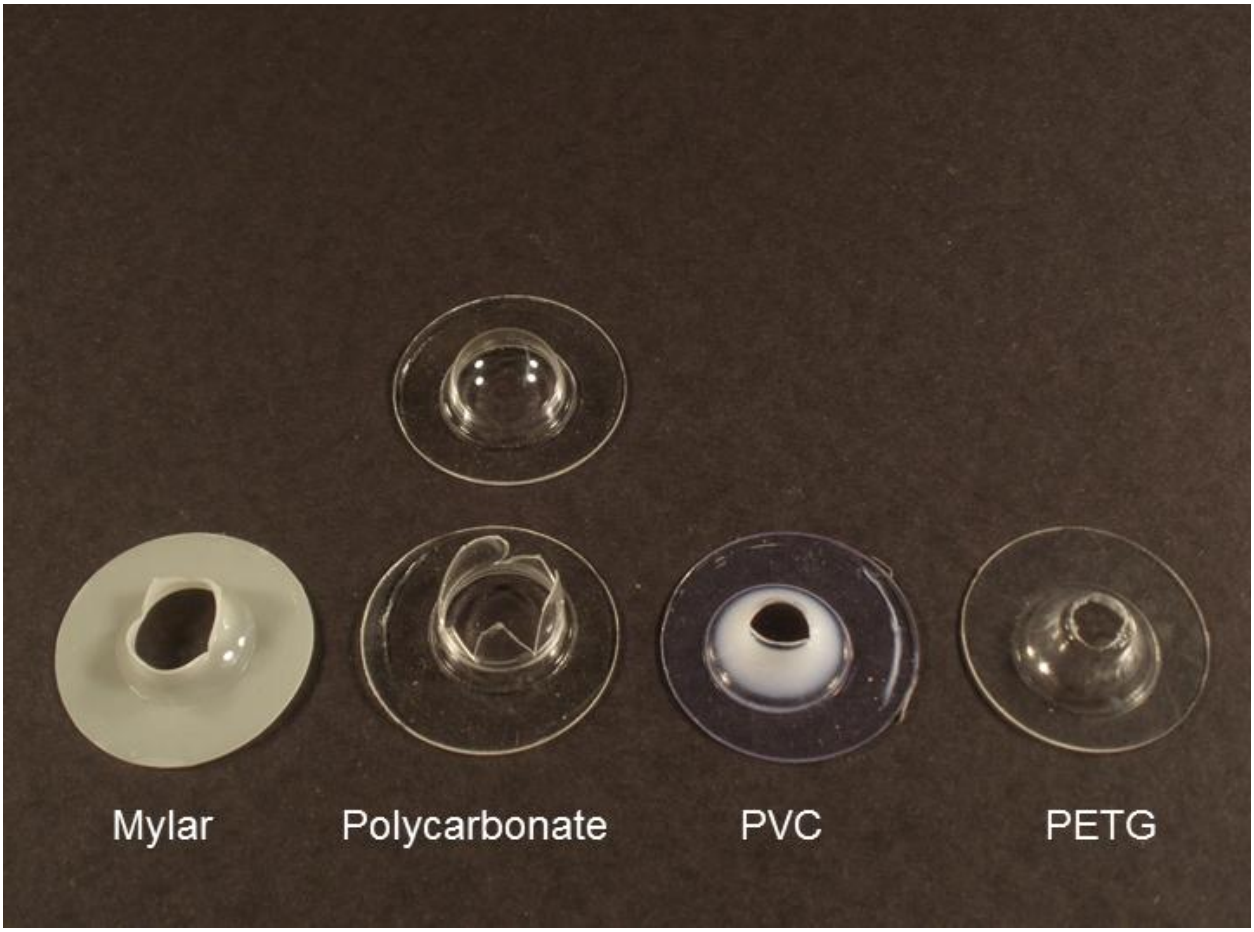


Figure 3.5. Membranes used for Blast Explosures

and potentially a reason for the observed low shock wave pressure. The polycarbonate material, on the other hand, opens to the full width of the blast nozzle, occasionally dislocating fragments that are expelled during the rupture. The second polycarbonate membrane shown in the picture is one that experienced a high pressure, without actually rupturing.

Mylar presents an interesting issue. As mentioned earlier, Mylar is a biaxial drawn material. PET is heated to approximately 200 degrees Celsius and then drawn or stretched in two dimensions to reorient the polymer chains for increased strength. Because the polymer chains become to a greater extent co-linear through the stretching process than the other thermoplastics used in this study, a rupture at high pressure appears to occur between the chains. The resulting opening in the membrane material therefore appears something like a "cat's eye". This raises the question though as to whether the resultant shock wave is directionally dependent as it exits the nozzle due to this rupture pattern.

As a single Mylar sheet is bi-axially drawn, the polymer orientation for that particular sheet should be uniform. To answer the "cat's eye" question, a section of a Mylar sheet was labeled with a continuous line, and then disks for the blast nozzle, centered on that line, were punched out. Blast exposure measurements, with the same positional parameters as previously used (50 mm down, 50 mm off-axis), were performed. The maximum shock wave pressure from ten blasts exposures were measured with the Mylar membrane marked line oriented at 0 degrees to the plane of the blast nozzle/transducer and ten blast exposures with the membrane marked line at 90 degrees to the plane of the blast nozzle/transducer. The results are shown in Table 3.3. A single disk of thickness 0.014 inch Mylar was used for these measurements.

Table 3.3. Blast Exposure Pressure of Mylar Disk Rotated Relative to the Blast Nozzle/Transducer Plane.

| Orientation to Nozzle/Transducer Plane (degrees) | 0 | 90 |
|---|---|---|
| Mean Maximum Positive Pressure (psi) | 8.9 | 8.9 |
| Standard Deviation (psi) | 0.9 | 0.6 |
| Coefficient of Variation | 10.5 | 7.1 |

As can be seen, identical mean maximum blast pressures are attained irrespective of the orientation of the Mylar membrane. This is most likely due to the membrane being mounted 20 mm above the actual exit port of the blast nozzle. At the point where the sudden rush of air leaves the nozzle any variability created by the membrane has been somewhat ameliorated.

These reproducibility and membrane tests performed above were done under identical conditions; that is the piezoelectric transducer was not moved or repositioned during the acquisition series. Therefore positioning variability need not be taken into account with the measurements. The piezoelectric crystal is shaped as a cylinder that must undergo compression on its long axis to produce a signal. In practice therefore, the transducer output will depend on its angular position relative to the blast nozzle output. The angular position dependence of the transducer with respect to the shock wave must be the next question to clarify.

Measurements to determine the angular position dependence of the transducer were performed with the plane of the transducer face at various angles with respect to vertical. The input surface of the transducer was maintained at 50 millimeters down (y-axis) and 50 millimeters off-axis (x-axis) from the center of the blast nozzle, as with the reproducibility measurements. Mylar membranes, with a total thickness of 0.019 inches, were used for generating the blast wave. The collected data are presented in Table 3.4.

Table 3.4. Angular Dependence of Piezoelectric Transducer with Axis of Blast Nozzle

| Transducer Angle to Vertical | Mean Maximum Positive Phase Pressure (psi) | Standard Deviation of Maximum Pressure (psi) |
|---|---|---|
| 0 | 9.3 | 0.4 |
| 15 | 13.7 | 0.6 |
| 30 | 14.0 | 2.0 |
| 45 | 13.2 | 1.2 |
| 60 | 12.1 | 1.6 |
| 75 | 10.9 | 1.9 |

These data are plotted in Figure 3.6. The mean pressure values tend to show first an increase in measured pressure up to 30 degrees. This is followed by a slight decrease in pressure as the angle relative to vertical is increased, but with a larger standard deviation. A statistical analysis using the Students t-test shows that from 30 degrees on, the change is not significant. Therefore, it can be assumed that although care must be taken to ensure that the transducers normal surface is perpendicular to the opening of the blast nozzle, inaccuracy of a couple of degrees will not significantly affect the pressure readings.

From the spark shadowgraph picture acquired by Jaffin, *et. al*. in Figure 2.2, the shape of the blast wave emanating from the nozzle should be something resembling a hemisphere. Measurements acquired on one side of the nozzle axis should be mirrored on the other side. Significant variations from this assumption could indicate a non-uniform and perhaps non-reproducible rupture of the membranes. Here again, without the aid of photographic recordings, the single pressure transducer must be used. To verify that the shock wave is symmetrical and thereby remove concerns of long range variability in the wave, the pressure transducer must be advanced along the x-axis at a fixed distance down (y-axis) from the opening of the nozzle.

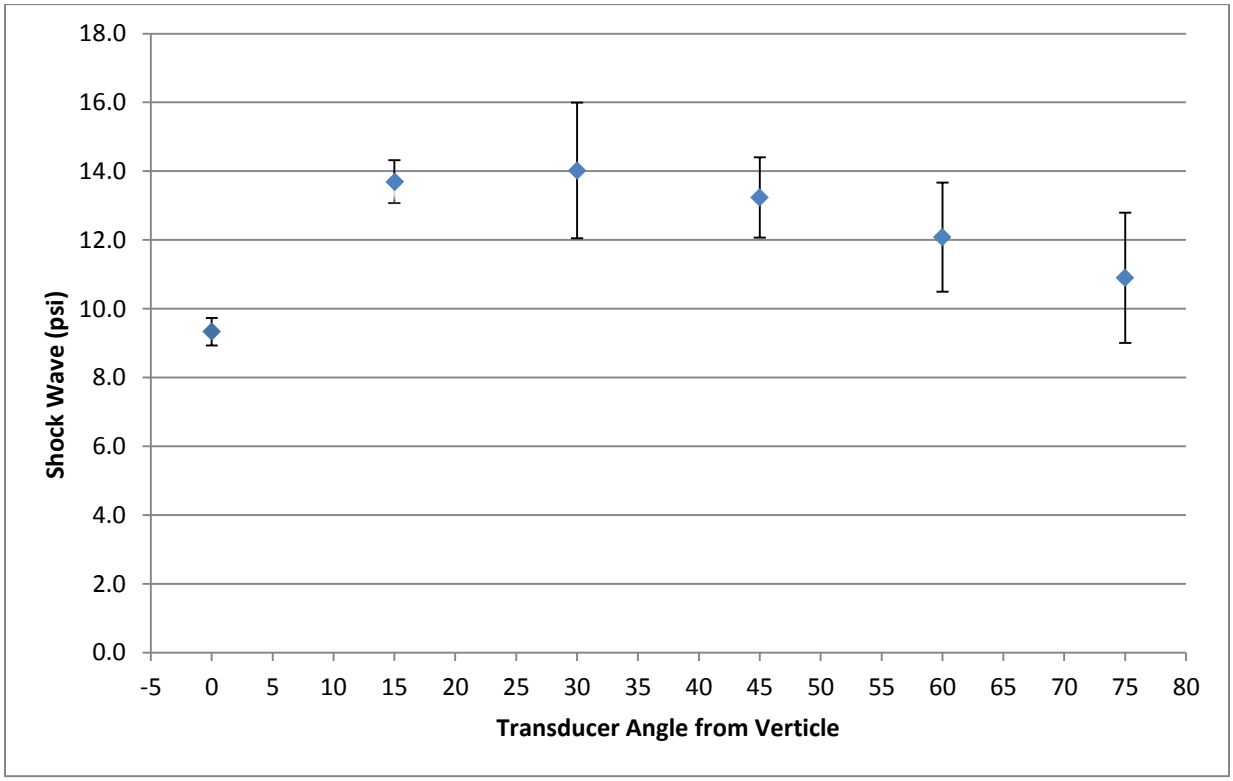


Figure 3.6. Angular Dependence of Piezoelectric Pressure Transducer Relative to Blast Nozzle

Measurements were taken from 100 mm on the left (defined as positive) of the nozzle to 100 mm on the right (defined as negative) of the nozzle. A y-axis distance of 50 mm from the nozzle opening was chosen and at least three measurements were performed at each location for averaging purposes. Following from the reproducibility test, Mylar and polycarbonate, having the highest shock wave pressure for a given chamber pressure at rupture, were chosen for these measurements. Mylar and polycarbonate membranes, of total thickness of 0.019 and 0.030 inches respectively, were used for these measurements. The resultant shock wave pressure readings for Mylar are listed in Table 3.5 and displayed in Figure 3.7 and for polycarbonate are listed in Table 3.6 and displayed in Figure 3.8.

Measurements with both membranes are remarkably similar, both showing a similar decrease in shock wave pressure as the measurements on either side move away from the central axis of the blast nozzle. This is as would be expected if the shock wave was symmetrical in shape. This measurement could likewise have been performed by maintaining a constant distance from the blast nozzle.

As the pressure transducer approached the central axis of the blast nozzle, the pressure trace of the air plume began to appear in the recordings. This was entirely expected. Of note though, are the values of the maximum pressure for this plume. For both the Mylar and Polycarbonate membranes, the maximum air plume pressure was recorded at 20 mm off axis on both sides of the nozzle. For the polycarbonate membrane, where this effect was most pronounced, the pressure data are given in Table 3.7.

Table 3.5. Mylar Pressure measurements relative to off-axis distance.

| Transducer Position along X-axis (mm) | Mean Maximum Positive Phase Pressure (psi) | Standard Deviation of Maximum Pressure (psi) |
|---|---|---|
| 100 | 5.2 | 0.5 |
| 80 | 7.2 | 1.0 |
| 60 | 11.8 | 0.9 |
| 40 | 18.5 | 0.8 |
| 20 | 40.0 | 4.0 |
| 0 | 53.3 | 1.3 |
| -20 | 38.4 | 2.5 |
| -40 | 20.5 | 1.6 |
| -60 | 11.6 | 2.6 |
| -80 | 6.8 | 0.2 |
| -100 | 4.8 | 0.3 |

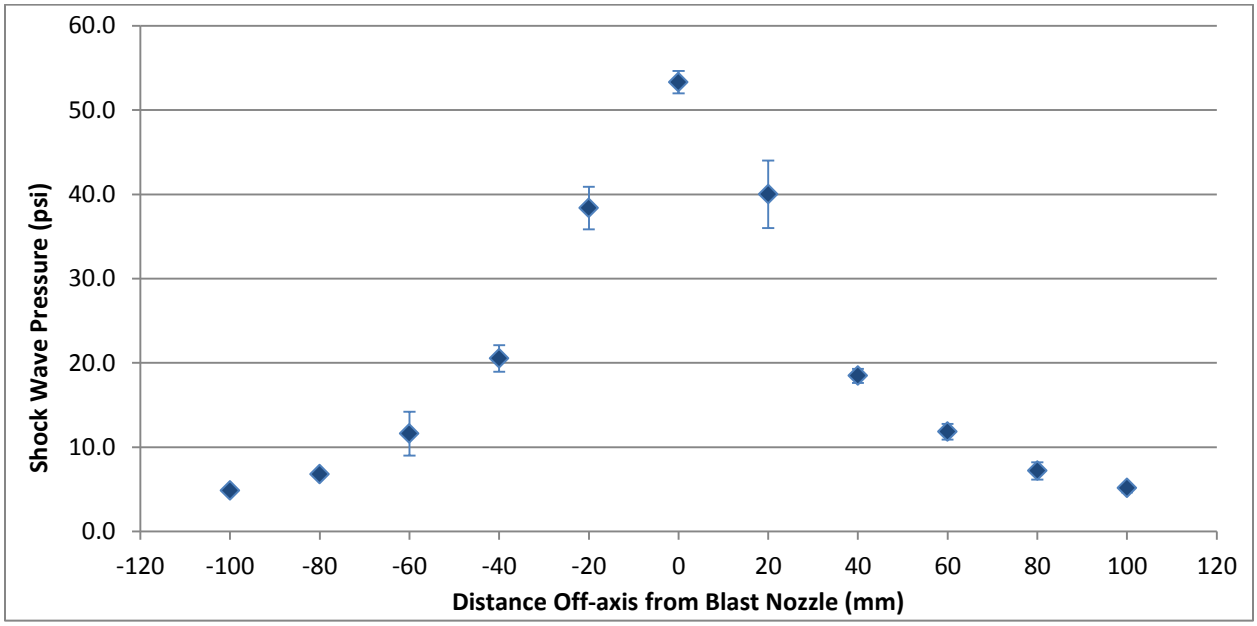


Figure 3.7. Shock wave pressure at 50 mm down relative to off-axis distance for Mylar membranes

Table 3.6. Polycarbonate Pressure measurements relative to off-axis distance.

| Transducer Position along X-axis (mm) | Mean Maximum Positive Phase Pressure (psi) | Standard Deviation of Maximum Pressure (psi) |
|---|---|---|
| 100 | 6.5 | 0.4 |
| 80 | 8.2 | 1.9 |
| 60 | 12.4 | 1.5 |
| 40 | 21.9 | 1.7 |
| 20 | 45.8 | 2.9 |
| 0 | 61.4 | 5.1 |
| -20 | 42.3 | 1.4 |
| -40 | 22.5 | 0.9 |
| -60 | 11.0 | 0.6 |
| -80 | 8.2 | 0.8 |

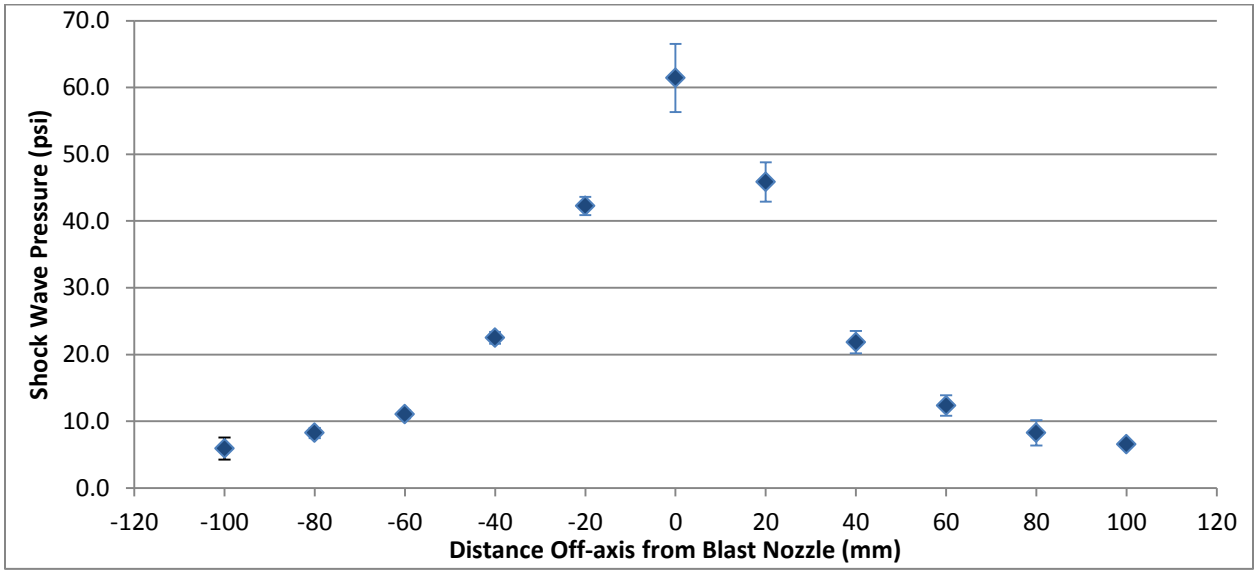


Figure 3.8. Shock wave pressure at 50 mm down relative to off-axis distance for Polycarbonate membranes

Table 3.7. Polycarbonate Air Blast Pressure measurements relative to off-axis distance.

| Transducer Position along X-axis (mm) | MeanMaximum Air Blast Pressure (psi) | Standard Deviation of Maximum Pressure (psi) |
|---|---|---|
| 40 | 33.4 | 14.4 |
| 20 | 115.6 | 18.2 |
| 0 | 54.5 | 0.4 |
| -20 | 120.4 | 12.6 |
| -40 | 28.9 | 8.8 |

The cause of this effect is uncertain, but undoubtedly related to the cylindrical shape of the blast nozzle and the dynamics of the air flow as the pulse escapes the nozzle confines and expands in space. Of primary importance though, these measurements do show that extreme caution must be used when performing the animal studies. Animals placed too close to the central axis of the nozzle could experience blast air pressures multiple factors higher that the shock wave and the injury may be confounded with the variable pressures experienced. Although similar results were noted with the Mylar membranes, no air blast pressures were detected at 40 mm offset. This could be primarily due to the fact that the ruptured opening of the Mylar membranes is smaller than that of the polycarbonate membranes.

Since it can now be shown that the shock wave is symmetrical, further blast wave measurement data need be acquired on only one side of the blast nozzle. The piezoelectric transducer was positioned in fixed x and y locations relative to the central axis of the blast nozzle opening, as has already been outlined. The final goal of the blast measurements was to find an optimal membrane material and optimal location, defined by maximum shock wave pressure with no contributing air blast pulse, for placing the animals, with the intent of inducing blast wave traumatic brain injury. To fully characterize the blast pulse output for a particular

membrane, measurements were performed at 0, 20, 40, 50, 60, 80 and100 millimeters (mm) off-axis from the central axis of the nozzle. At each one of these offsets, measurements were taken at 40, 60, 80, 100 and 120 mm below the nozzle exit port. These measurements positions are graphically illustrated in a composite form in Fig 3.9. The face of the piezoelectric transducer was always maintained normal to a line drawn between the transducer and the center of the blast nozzle.

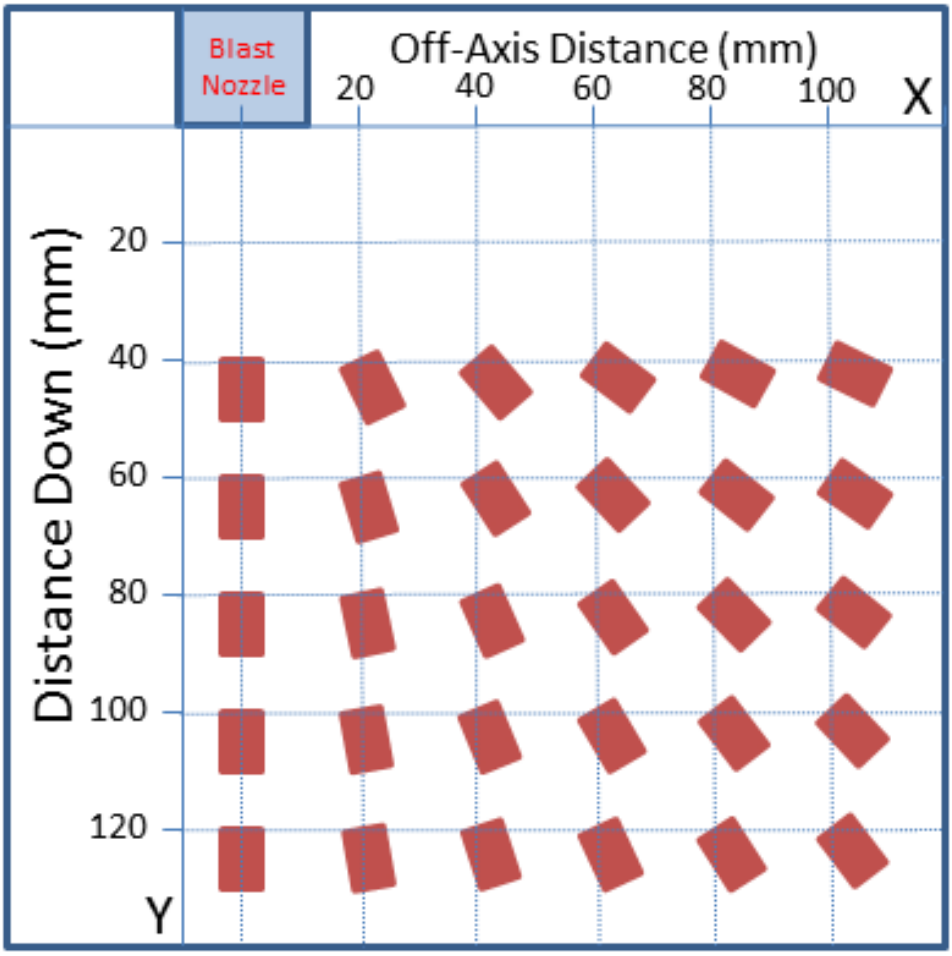


Figure 3.9. Transducer measurement positions in blast field

First the data from PVC and PETG will be discussed. As was shown above in the reproducibility test, both of these membranes produce a shock wave that off-axis is substantially lower in amplitude than either polycarbonate or Mylar. The purpose of testing these therefore was merely to get a global impression of the blast waves produced by those membranes. At all measurement positions, an attempt was made to acquire two or more blast exposures. A total thickness of 0.060 inches of either PVC or PETG was required to give a chamber pressure around 1500 psi. The data were maintained and manipulated in a Microsoft Excel spreadsheet. The complete set of data collected for the PVC membranes is displayed in Table 3.8 to 3.11 and that for PETG is in Tables 3.12 to 3.15.

As explained earlier, and shown in Figure 3.5, the rupture of the PVC and PETG membranes produces a fairly small opening. The entire pulse of air escaping the chamber must therefore be tightly focused. This explains the high on-axis pressure peak, with the shock wave pressure rapidly dropping to low values at greater off-axis distances. With PETG, the shock wave pressure dropped below the sensitivity of the piezoelectric transducer at 60 mm off-axis. It is difficult to speculate what is happening at the membrane at the time of rupture without high speed photography, but the data seems to indicate that the rupture, especially for PETG, must be slow compared to other membranes, such as polycarbonate to be discussed shortly. A rapid and complete opening of the membrane would force the entire mass of high pressure air stored in the chamber to almost instantaneously come into contact with the static air at the nozzle, thereby generating a strong shock wave. A slower opening will extend that time of contact, reducing the amplitude of a shock wave. Furthermore, the long duration of the PETG shock wave data supports this “slow opening” concept; a slow interaction between the high pressure and static air would result in a drawn out duration of the positive wave.

## PVC Membrane Data

Table 3.8. PVC Shock Wave Maximum Pressure Measurements

| Pressure Measurements in psi | | Off-axis Distance from Blast Nozzle Center (mm) | | | | | |
|---|---|---|---|---|---|---|---|
| | | 0 | 20 | 40 | 60 | 80 | 100 |
| Distance Down from Nozzle (mm) | 40 | - | - | 6.4 ±0.7 | - | - | - |
| | 60 | - | 15.8 ±0.2 | - | 5.4 ±0.1 | 5.7 ±0.1 | 3.2 ±0.4 |
| | 80 | - | - | 9.6 ±0.0 | 6.8 ±0.3 | 6.1 ±0.1 | 3.5 ±0.1 |
| | 100 | 107.0 ±10.0 | 29.7 | 9.7 ±1.0 | 6.8 ±0.7 | - | 3.4 ±0.1 |
| | 120 | - | - | - | 5.9 ±0.1 | - | 4.8 ±0.6 |

Table 3.9. PVC Duration of Positive Phase

| Duration Measured in milliseconds | | Off-axis Distance from Blast Nozzle Center (mm) | | | | | |
|---|---|---|---|---|---|---|---|
| | | 0 | 20 | 40 | 60 | 80 | 100 |
| Distance Down from Nozzle (mm) | 40 | - | - | 41 ±1 | - | - | - |
| | 60 | - | 64 ±6 | - | 62 ±3 | 55 ±1 | 46 ±0 |
| | 80 | - | - | 90 ±0 | 72 ±3 | 77 ±16 | 49 ±1 |
| | 100 | 220 ±71 | 188 | 118 ±2 | 102 ±12 | - | 69 ±4 |
| | 120 | - | - | - | 124 ±6 | - | 97 ±1 |

Table 3.10. PVC Negative Phase Minimum Pressure Measurements

| Pressure Measurements in psi | | Off-axis Distance from Blast Nozzle Center (mm) | | | | | |
|---|---|---|---|---|---|---|---|
| | | 0 | 20 | 40 | 60 | 80 | 100 |
| Distance Down from Nozzle (mm) | 40 | - | - | -3.4 | - | - | - |
| | 60 | - | 11.7 ±1.1 | - | -1.2 ±0.1 | -1.9 | -0.6 ±0.0 |
| | 80 | - | - | -6.9 ±1.3 | -1.8 ±0.2 | -1.2 ±0.4 | -0.9 ±0.1 |
| | 100 | - | -1.5 | -9.6 ±2.1 | -3.0 ±1.1 | - | -1.0 ±0.2 |
| | 120 | - | - | - | -2.7 ±1.1 | - | -1.4 ±0.1 |

Table 3.11. PVC Air Blast Maximum Pressure Measurements

| Pressure Measurements in psi | | Off-axis Distance from Blast Nozzle Center (mm) | | | | | |
|---|---|---|---|---|---|---|---|
| | | 0 | 20 | 40 | 60 | 80 | 100 |
| Distance Down from Nozzle (mm) | 40 | - | - | - | - | - | - |
| | 60 | - | - | - | - | - | - |
| | 80 | - | - | - | - | - | - |
| | 100 | 135.6 ±5.8 | 17.2 | 7.0 ±0.7 | - | - | - |
| | 120 | - | - | - | - | - | - |

## PETG Membrane Data

Table 3.12. PETG Shock Wave Maximum Pressure

| Pressure Measurements in psi | | Off-axis Distance from Blast Nozzle Center (mm) | | | | | |
|---|---|---|---|---|---|---|---|
| | | 0 | 20 | 40 | 60 | 80 | 100 |
| Distance Down from Nozzle (mm) | 40 | - | 10.0 | 1.7 | - | - | - |
| | 60 | - | 7.2 ±1.3 | 5.0 | - | - | - |
| | 80 | 125.0 | 17.2 ±11.0 | 2.6 ±0.3 | - | - | - |
| | 100 | 108.5 ±20.9 | 31.2 | 2.9 | - | - | - |
| | 120 | 76.8 | - | - | - | - | - |

Table 3.13 PETG Duration of Positive Phase

| Duration Measured in milliseconds | | Off-axis Distance from Blast Nozzle Center (mm) | | | | | |
|---|---|---|---|---|---|---|---|
| | | 0 | 20 | 40 | 60 | 80 | 100 |
| Distance Down from Nozzle (mm) | 40 | - | 76 | 84 | - | - | - |
| | 60 | - | 117 ±13 | 114 | - | - | - |
| | 80 | 380 | 266 ±144 | 146 ±6 | - | - | - |
| | 100 | 420 ±341 | 256 | - | - | - | - |
| | 120 | 740 | - | - | - | - | - |

Table 3.14. PETG Negative Phase Minimum Pressure

| Pressure Measurements in psi | | Off-axis Distance from Blast Nozzle Center (mm) | | | | | |
|---|---|---|---|---|---|---|---|
| | | 0 | 20 | 40 | 60 | 80 | 100 |
| Distance Down from Nozzle (mm) | 40 | - | -6.6 | -0.9 | - | - | - |
| | 60 | - | -7.4 ±0.6 | -3.4 | - | - | - |
| | 80 | - | -6.8 ±1.8 | -3.3 ±0.9 | - | - | - |
| | 100 | - | - | -3.2 | - | - | - |
| | 120 | - | - | - | - | - | - |

Table 3.15. PETG Air Blast Maximum Pressure

| Pressure Measurements in psi | | Off-axis Distance from Blast Nozzle Center (mm) | | | | | |
|---|---|---|---|---|---|---|---|
| | | 0 | 20 | 40 | 60 | 80 | 100 |
| Distance Down from Nozzle (mm) | 40 | - | 11.9 | - | - | - | - |
| | 60 | - | 9.1 ±1.8 | - | - | - | - |
| | 80 | 76.7 | 12.4 ±4.1 | - | - | - | - |
| | 100 | 82.7 ±13.0 | 21.8 | - | - | - | - |
| | 120 | 73.8 | - | - | - | - | - |

Data for the polycarbonate membrane are tabulated in Tables 3.16 - 3.19. Polycarbonate disks of thickness 0.030 inches were used. These membranes had a rupture pressure of 1400 psi. As mentioned above, and shown in Figure 3.5, the polycarbonate material is the one that ruptures and separates (or opens) to the greatest extent possible. The residue of a post-blast ruptured member is completely in contact with the internal cylindrical side wall of the blast nozzle. Small pieces of polycarbonate material (shrapnel) are also dislodged from the membrane and can exit with the air blast.

An immediate item of note about the polycarbonate blasts, as presented in the Table 3.16, is the significantly higher amplitude of the shock wave generated by polycarbonate, compared to either the PVC or PETG membranes. As explained above, this can only be due to the larger "impact zone" where the high pressure air meets the static room pressure air. The shock wave pressures are almost twice the pressures produced by the PVC membrane at off-axis distances of greater than 60 mm. The drawback though to this large opening rupture of the polycarbonate membrane is the wider air blast pulse. The data from Table 3.19 show that this air blast is substantially greater in pressure and observed at greater off-axis distances than either of the other two membranes which have smaller openings. If the goal is a pure shock wave, this will be a detriment, as the animal must be positioned further away from the nozzle where the shock wave pressure is reduced. Of additional note though, the total shock wave pulse durations are greater and as mentioned above, this could potentially be a benefit for inducing injury blast TBI injury.

From the four polymer membrane materials chosen for this study, Mylar was the material studied to the greatest degree. This was due to the simplicity of cutting the material, ease and rapidity of fitting it into the blast nozzle, the fact that it is referenced by other researchers working in blast wave measurements [48], and perhaps most importantly, the high shock wave

## Polycarbonate Membrane Data

Table 3.16. Polycarbonate Shock Wave Maximum Pressure

| Pressure Measurements in psi | | Off-axis Distance from Blast Nozzle Center (mm) | | | | | |
|---|---|---|---|---|---|---|---|
| | | 0 | 20 | 40 | 60 | 80 | 100 |
| Distance Down from Nozzle (mm) | 40 | - | - | 21.7 ±1.1 | 11.0 ±2.3 | 6.7 ±1.7 | 4.5 ±0.4 |
| | 60 | - | - | 19.9 ±1.3 | 12.1 ±1.8 | 7.9 ±0.8 | 5.6 ±0.7 |
| | 80 | - | 24.2 | 20.3 ±0.8 | 13.7 ±1.3 | 9.4 ±0.5 | 6.9 ±0.9 |
| | 100 | 22.9 ±1.2 | 21.8 | 15.9 ±0.8 | 12.4 ±0.4 | 9.3 ±0.4 | 8.4 ±0.4 |
| | 120 | 15.8 ±0.2 | - | - | 11.3 ±0.4 | 9.4 ±0.4 | 8.0 ±0.2 |

Table 3.17. Polycarbonate Duration of Positive Phase

| Duration Measured in milliseconds | | Off-axis Distance from Blast Nozzle Center (mm) | | | | | |
|---|---|---|---|---|---|---|---|
| | | 0 | 20 | 40 | 60 | 80 | 100 |
| Distance Down from Nozzle (mm) | 40 | - | - | 69 ±14 | 51 ±5 | 51 ±1 | 55 ±4 |
| | 60 | - | | 52 ±9 | 72 ±7 | 61 ±5 | 75 ±31 |
| | 80 | - | 60 | 56 ±0 | 112 ±23 | 96 ±17 | 82 ±12 |
| | 100 | 180 ±113 | 224 | 42 ±3 | 159 ±9 | 113 ±8 | 132 ±5 |
| | 120 | 52 ±6 | - | - | 221 ±42 | 165 ±3 | 159 ±28 |

Table 3.18. Polycarbonate Negative Phase Minimum Pressure

| Pressure Measurements in psi | | Off-axis Distance from Blast Nozzle Center (mm) | | | | | |
|---|---|---|---|---|---|---|---|
| | | 0 | 20 | 40 | 60 | 80 | 100 |
| Distance Down from Nozzle (mm) | 40 | - | - | -8.6 ±1.1 | -4.3 ±0.9 | -1.9 ±0.2 | -0.8 ±0.3 |
| | 60 | - | - | - | -5.3 ±1.7 | -2.6 ±0.3 | -1.6 ±0.2 |
| | 80 | - | - | - | -9.1 ±1.9 | -3.9 ±0.2 | -2.0 ±0.4 |
| | 100 | - | - | - | -10.3 ±1.0 | -4.7 ±0.3 | -3.1 ±0.6 |
| | 120 | - | - | - | -9.1 ±1.9 | -5.5 ±1.0 | -4.0 ±0.2 |

Table 3.19. Polycarbonate Air Blast Maximum Pressure

| Pressure Measurements in psi | | Off-axis Distance from Blast Nozzle Center (mm) | | | | | |
|---|---|---|---|---|---|---|---|
| | | 0 | 20 | 40 | 60 | 80 | 100 |
| Distance Down from Nozzle (mm) | 40 | - | - | 29.0 ±11.8 | - | - | - |
| | 60 | - | - | 32.6 ±9.0 | - | - | - |
| | 80 | - | 125.0 | 60.0 ±7.1 | - | - | - |
| | 100 | 61.6 ±19.0 | 137.3 | 55.0 ±7.1 | - | - | - |
| | 120 | 47.4 ±3.7 | - | - | - | - | - |

pressure relative to the other polymers. In Table 3.2, Mylar stands out as a material that produces a strong shock wave with total material thickness of half of what is required for other membranes, including polycarbonate. Additionally, due of the rigidity of PVC and PETG, these membranes must be forced, frequently with a hammer, into the blast nozzle.

A single Mylar membrane of 0.014 inches was used for the experiments to map out the blast wave in space. These membrane disks ruptured at 1300 psi. The complete set of data for the various parameters measured during each blast is listed in Tables 3.20 – 3.23. On-axis, the initial shock wave is immediately followed by the air blast as was shown in Figure 3.4. Therefore the shock wave is a nearly instantaneous pressure increase, with no decline to a baseline or negative pressure value: in essence, on- or nearly on-axis readings display an unexpected shock wave profile. The maximum pressure of this instantaneous rise is noted to decrease dramatically with increasing distance, by a factor of 5, as the transducer is moved from 40 to 120 millimeters from the blast nozzle. The following maximum pressure due to the air blast pulse on the central axis does not change as dramatically though. For the 40 to 120 millimeter distance from the blast nozzle, the peak air blast pressure decreases by a factor of 1.5, as can be seen by comparing data from Tables 3.20 and 3.23. This is easily understood due to the nature of the shock wave. It is a movement of energy and not bulk material, like the air pulse.

As measurements are recorded further off-axis, the air blast wave is absent and only the Friedlander type shock wave is recorded. The shock wave peak pressure values of Mylar are very similar, although slightly lower than the polycarbonate values. Without the understanding of the lateral dimensions of the air blast pulse emitted from both the polycarbonate and the Mylar membranes, polycarbonate would appear to be the material of choice. Here again, the final

## Mylar Membrane Data

Table 3.20. Mylar Shock Wave Maximum Pressure

| Pressure Measurements in psi | | Off-axis Distance from Blast Nozzle Center (mm) | | | | | |
|---|---|---|---|---|---|---|---|
| | | 0 | 20 | 40 | 60 | 80 | 100 |
| Distance Down from Nozzle (mm) | 40 | 89.5 ±0.0 | 31.2 ±4.1 | 15.5 ±0.9 | 6.6 ±0.2 | 4.5 ±0.7 | 3.3 ±0.1 |
| | 60 | 38.9 ±0.8 | 111.5 ±12.0 | 17.4 ±0.7 | 11.3 ±0.7 | 7.1 ±0.1 | 3.7 ±0.1 |
| | 80 | 35.7 ±1.7 | 28.3 ±2.2 | 16.6 ±0.6 | 9.7 ±0.2 | 8.2 ±0.3 | 5.0 ±0.2 |
| | 100 | 25.6 ±1.7 | 23.5 ±0.2 | 14.2 ±0.7 | 11.3 ±0.4 | 8.1 ±0.4 | 5.9 ±0.4 |
| | 120 | 17.9 ±2.0 | 16.0 ±0.6 | 13.1 ±0.7 | 10.9 ±0.8 | 8.5 ±0.5 | 6.9 ±0.7 |

Table 3.21. Mylar Duration of Positive Phase

| Duration Measured in milliseconds | | Off-axis Distance from Blast Nozzle Center (mm) | | | | | |
|---|---|---|---|---|---|---|---|
| | | 0 | 20 | 40 | 60 | 80 | 100 |
| Distance Down from Nozzle (mm) | 40 | - | - | 51 ±1 | 54 ±1 | 52 ±1 | 49 ±1 |
| | 60 | - | - | 68 ±1 | 70 ±0 | 62 ±1 | 59 ±1 |
| | 80 | - | - | 105 ±1 | 70 ±7 | 81 ±1 | 64 ±1 |
| | 100 | - | - | 121 ±1 | 101 ±1 | 88 ±1 | 86 ±1 |
| | 120 | - | - | 83 ±1 | 140 ±1 | 140 ±1 | 121 ±1 |

Table 3.22. Mylar Negative Phase Minimum Pressure

| Pressure Measurements in psi | | Off-axis Distance from Blast Nozzle Center (mm) | | | | | |
|---|---|---|---|---|---|---|---|
| | | 0 | 20 | 40 | 60 | 80 | 100 |
| Distance Down from Nozzle (mm) | 40 | - | - | -9.2 ±0.6 | -1.4 ±0.0 | -0.8 ±0.3 | -1.1 ±0.1 |
| | 60 | - | - | -8.9 ±1.2 | -4.7 ±0.5 | -1.6 ±0.6 | -1.2 ±0.0 |
| | 80 | - | - | -9.5 ±2.9 | -3.2 ±0.6 | -2.0 ±0.0 | -1.4 ±0.0 |
| | 100 | - | - | -9.3 ±1.2 | -5.8 ±0.9 | -2.7 ±0.5 | -1.8 ±0.2 |
| | 120 | - | - | - | -7.6 ±1.4 | -3.6 ±0.5 | -2.4 ±0.3 |

Table 3.23. Mylar Air Blast Maximum Pressure Measurements

| Pressure Measurements in psi | | Off-axis Distance from Blast Nozzle Center (mm) | | | | | |
|---|---|---|---|---|---|---|---|
| | | 0 | 20 | 40 | 60 | 80 | 100 |
| Distance Down from Nozzle (mm) | 40 | 69.2 ±6.6 | 86.6 ±11.6 | - | - | - | - |
| | 60 | 27.1 ±6.2 | 124.5 ±27.6 | - | - | - | - |
| | 80 | 57.9 ±1.3 | 136.0 ±15.6 | 40.1 | - | - | - |
| | 100 | 53.1 ±4.7 | 85.0 ±4.6 | 29.7 | - | - | - |
| | 120 | 45.3 ±7.3 | 110.7 ±3.3 | 32.5 ±9.8 | - | - | - |

rupture width of the membrane plays a significant role. Whereas it was mentioned above how the polycarbonate membranes rupture to the maximum extent allowed by the blast nozzle, the Mylar membranes are slightly less than that. The average ruptured open area measured from 8 polycarbonate disk is 166 $mm^2$, while for 8 Mylar membranes the area is 100 $mm^2$. These numbers compare with PVC and PETG at around 35-45 $mm^2$.

The total duration of the shock wave measured, where there is no confounding air blast pulse, reveals that for both the Mylar and polycarbonate membranes the shock wave lengthens, or spreads out, as it travels radially from the nozzle. This can be seen in Tables 3.17 and 3.21 for polycarbonate and Mylar respectively, as one examines the data in diagonal lines. From those two tables, it can be inferred that the shock wave from the polycarbonate membrane begins to disperse at shorter radial distances than the Mylar membrane. Additionally, at the maximum radial distances of the shock wave measurements, the increased dispersion of the polycarbonate shock wave is greater than the dispersion for Mylar.

A clear indication that the air blast component has no contribution to a particular blast explosion is the presence of a negative phase to the shock wave. As repeatedly demonstrated, the air blast is an additional, confounding positive pressure component, that when superimposed on the explosion, obliterates the negative phase. The negative phase of the shock wave, as was shown in Figure 3.3, is a readily observable component in the recordings performed here. Data for negative phase for the polycarbonate and Mylar membranes are displayed in Tables 3.18 and 3.22. From these two tables it can be seen that Mylar maintains the greatest negative pressure at measurement points closest to the nozzle, while polycarbonate has greater negative pressure values at further distances away. As the shock wave is absorbed and traverses through tissue, it will be the sum of the absolute values of the positive and negative pressure values, the peak-to-

peak pressure, which will contribute to the traumatic brain injury through the generation of shear wave, as discussed earlier.

The data for the four membranes have been collected and described throughout this section. The choice is now to select the membrane that will yield the strongest shock wave (i.e. that potential for the greatest injury) while avoiding the potential for detrimental effects from the air blast wave. PETG and PVC membranes may be disqualified immediately due to their low shock wave pressures. Polycarbonate and Mylar, both generate shock waves with high amplitudes. Polycarbonate, though, as discussed above, has a wider air blast component, requiring that an animal be positioned radially further away from the nozzle, and into an area of lower maximum shock wave pressure. Through elimination, Mylar then becomes the membrane of choice.

Beginning with the positional dependence measurements that were done with the Mylar membranes, a location of 40 millimeter off-axis and 60 millimeters down from the nozzle was chosen as the location for the placement of the cranium of the test animals. This position seemed to provide the strongest shock wave with no air blast contribution for the measurement characteristic used in the collection of the Mylar data. The final set of testing and data collection involved measurements at this position, while trying to increase the overall chamber pressure and resultant shock wave pressure. Increasing the chamber pressure before membrane rupture was achieved by adding additional layers of membrane material. The above Mylar data were collected while using a single membrane of 0.014 inches thickness. Additional Mylar membranes of 0.005 inches were added on top of the first one.

The first set of measurements with the layered Mylar involved a total thickness of 0.019" with the transducer positioned at 40 millimeters off-axis and 60 millimeters down as described

above. Immediately, an air blast exposure was noted in the recordings. This air blast pulse was not noted in the measurements with the 0.014" Mylar membrane alone and is due to the increased pressure and volume of air exiting the chamber at the instant of rupture. Therefore, to stay within the selected criteria of avoiding an air blast for the induction of TBI, a greater off-axis position is required. A new position of 50 millimeters off-axis, and 60 millimeters down was chosen. The input surface of the piezoelectric transducer was maintained normal to the line bisecting the transducer and the center of the blast nozzle. Mylar membrane thicknesses totaling 0.014, 0.019 and 0.024 inches were tested. No air blast pulse was measured at this position for any of these total membrane thicknesses. The measured parameters are listed in Table 3.24.

These measurements clearly show that at the maximum total Mylar membrane thickness of 0.024 inches, and the transducer position of 50 mm off-axis, 60 mm down, the peak-to-peak shock wave has amplitude of nearly 29 psi. The bursting pressure of the stack of Mylar membrane disks is at 2700 psi. Attempts were made to generate blast exposures with 0.029 inches of Mylar membrane, but this thickness required a maximum pressure that exceeds the pressure supplied by the high pressure air cylinder.

Although an air blast is not noted at the 50 mm off-axis, 60 mm down position, earlier measurements (above) have shown the edges of it to exist at 40 mm off-axis; a mere 10 mm away. For the animal work, the desire is for the shock wave to impact the cranium of the animal. Basic rat anatomy shows that the center of the brain is approximately 20 mm from the tip of the nose. If an animal is placed at the 50 mm off-axis, 60 mm down position, it is very possible that the strong air blast component will unintentionally impact rat body structure that is located at a lesser off-axis distance than the cranium. The result of this blunt force on the physiological state of the animal could lead to an indeterminate and unpredictable amount of

Table 3.24. Mylar Shock Wave Parameters measured at 50 mm off-axis and 60 mm down.

| Material | Mylar | | |
|---|---|---|---|
| Total Thickness (in.) | 0.014 | 0.019 | 0.024 |
| Chamber Pressure at Bursting (psi) | 1300 | 1900 | 2700 |
| Positive Phase Amplitude | | | |
| Mean Maximum Positive Pressure (psi) | 12.7 | 15.1 | 19.6 |
| Standard Deviation (psi) | 1.3 | 2.1 | 2.2 |
| Coefficient of Variation | 10.3 | 13.9 | 11.0 |
| Duration of Positive Phase | | | |
| Mean Duration (msec) | 67 | 66 | 80 |
| Standard Deviation (msec) | 8 | 4 | 11 |
| Coefficient of Variation | 11.3 | 5.9 | 13.4 |
| Negative Phase Amplitude | | | |
| Mean Maximum Negative Pressure (psi) | -5.9 | -8.3 | -9.6 |
| Standard Deviation (psi) | 1.6 | 1.6 | 1.4 |
| Coefficient of Variation | 28.3 | 19.5 | 14.2 |
| Duration of Negative Phase | | | |
| Mean Duration (msec) | 446 | 648 | 840 |
| Standard Deviation (msec) | 29 | 97 | 61 |
| Coefficient of Variation | 6.1 | 14.9 | 7.2 |

damage. To reduce the possibility of this happening, additional measurements were acquired at another location.

Out of concern for the potential that other anatomical structures on the rat to be studied might be affected by the air blast emanating from a blast exposure, measurements were made at 50 mm off-axis and 50 mm down. It has already been shown that the air blast expands in the x dimension as the volume of air leaves the nozzle following rupture of the membrane. This expansion increases with increasing distance from the nozzle and continues until the force of the air blast is dissipated. The picture by Jaffin, Figure 2.2, illustrates this effect well. So instead of moving further off-axis, a decision was made to remain at the 50 mm off-axis, but decrease the vertical distance from the nozzle from 60 to 50 mm. Measurements from this new location are shown in Table 3.25.

The measurements at this position show that the maximum peak-to-peak shock wave pressure is nearly 24 psi. As before, this value is from the maximum thickness of Mylar membranes that may be used with the current setup. This value at 50 mm off-axis, 50 mm down, is slightly less than the 29 psi noted above for the 50 mm off-axis, 60 mm down measurements. The final question remains to see if this shock wave pressure is sufficient for inducing the desired blast wave traumatic brain injury in the rat model.

In summary, the blast device was tested with four different membrane materials. These were PVC, PETG, polycarbonate and Mylar. PVC and PETG were quickly discarded due to their rupturing characteristics that produce a low amplitude shock wave. Polycarbonate and Mylar, both being able to create a strong shock wave were further explored to test various parameters associated with the blast device.

Table 3.25. Mylar Shock Wave Parameters measured at 50 mm off-axis and 50 mm down.

| Material | Mylar | | |
|---|---|---|---|
| Total Thickness (in.) | 0.014 | 0.019 | 0.024 |
| Chamber Pressure at Bursting (psi) | 1300 | 1900 | 2700 |
| Positive Phase Amplitude | | | |
| Mean Maximum Positive Pressure (psi) | 9.7 | 11.9 | 16.0 |
| Standard Deviation (psi) | 0.7 | 2.8 | 2.8 |
| Coefficient of Variation | 7.1 | 23.5 | 17.2 |
| Duration of Positive Phase | | | |
| Mean Duration (msec) | 52 | 53 | 57 |
| Standard Deviation (msec) | 3 | 5 | 4 |
| Coefficient of Variation | 4.9 | 10.2 | 6.9 |
| Negative Phase Amplitude | | | |
| Mean Maximum Negative Pressure (psi) | -4.2 | -5.2 | -7.9 |
| Standard Deviation (psi) | 0.9 | 1.2 | 1.3 |
| Coefficient of Variation | 20.2 | 23.0 | 15.8 |
| Duration of Negative Phase | | | |
| Mean Duration (msec) | 523 | 756 | 801 |
| Standard Deviation (msec) | 14 | 24 | 39 |
| Coefficient of Variation | 2.7 | 3.2 | 4.9 |

It was found that although Mylar membranes have a preferential orientation for rupturing, the actual orientation of the membrane in the nozzle does not affect the resultant shock wave. The shock wave was further shown, with the use of both the polycarbonate and Mylar membranes, to be symmetrically emanating from the exit port of the blast nozzle. The air blast component of the blast explosion was noted to exist only at points directly underneath the nozzle exit port, but was found to increase in the lateral dimension with increasing distance from the nozzle. For the polycarbonate membrane this lateral dispersion of the air blast was found to be greater than that of the Mylar membrane, necessitating a greater off-axis distance for recording a pure shock wave. The use of a greater off-axis distance results in a distance dependent reduction in the absolute amplitude of the shock wave. Polycarbonate membranes therefore are less desirable than the Mylar membranes. And finally, the orientation of the central axis of the piezoelectric pressure transducer relative to the nozzle was shown to have an effect on the maximum pressure reading of the shock wave. Caution must therefore be employed when positioning the transducer for acquiring pressure measurements.

Having characterized the shock wave produced by this blast device, and having selected an initial position for what can be hoped to produce the greatest injury to the cranium, the study of this project will now move to the work with animals.

## B. Animal Measurements

Inducing blast wave traumatic brain injury in experimental animals was carried out with the use of the blast wave device. The degree of TBI was assessed through measurement with the Nuclear Magnetic Resonance Imager in the Department of Radiology, Radiation Physics and Biology Division. All animal studies were approved by the VCU Institutional Animal Care and Use Committee (IACUC) prior to commencement of any work. The animal species selected for this work were Sprague-Dawley rats in the weight range of 300-400 grams. These rats are adult age, yet small enough to fit inside the imaging apparatus for the MR imager without causing restrictions.

Performing MR studies on research animals is extremely difficult. There are many factors that need to be considered and accounted for, as the stability of the animals while undergoing the MR examination is of utmost importance. All animals that go into the MR imager must be anesthetized with isoflurane, intubated and mechanically ventilated. Isoflurane is a halogenated ether administered with pure oxygen, that produces the anesthetic state through the interference of synaptic transmission. The ventilation rate and volume must be carefully defined before the study. The animal's body temperature must also be maintained, as the anesthesia gas will interfere with the animal's ability to self-regulate. At the optimal isoflurane concentration, ventilation rate and volume and body temperature, the animal should be completely motionless. A peculiarity of working with the MR imager is the requirement that no conductive lines for monitoring may extend from outside of the magnet to the animal. With the setup for this experiment, once the animal is in the magnet, monitoring is impossible.

Anesthesia and ventilation is provided by a Narcomed (North America Dräger) air driven ventilator. The unit has received annual calibrations and was functioning normally. The

animal's condition is assessed visually while on the table, before and after the MR studies. The assessment is based on two observable conditions. First is the observation of adequate chest motion during inspirations, particularly, chest motion only during the inspiration phase on the driving ventilator. Animals that that have not experienced deep enough anesthesia level will frequently breathe on their own, something referred to as "auto-breath", in-between the ventilator inspiration phase. This will lead to motion artifacts, especially on the diffusion weighted images. Second, the color of the rat's limbs and eyes are a good indication of the animal's perfusion state. A pinkish color of the limbs and eyes is indicative of a healthy, well ventilated and perfused animal, whereas grey indicates a state of oxygen stress. Body temperature may also be monitored by touch, as an animal cold enough to be in distress is easily discernable with one's hand. Placement of a femoral line for monitoring blood pressure and blood gas content is possible and has been performed numerous times with animals in the past, but the animals in this study are to be imaged almost daily over a seven or eight day period. We have found that the extensive damage done to the femoral artery line prevents multiple catheterizations. Similarly, electrodes for physiological monitoring that are attached to the animal may not be used. The electrodes will introduce a significant amount of radio frequency noise in to the MR data collection, as they will act as antennae extending outside of the magnet.

Small animal studies have been performed in the MR Laboratory for many years, so substantial experience was already developed before this blast project was begun. For use with rats, a specially designed stereotactic device, in the shape of a cylindrical tube, had already been constructed that allowed positioning of the animal at the iso-center of the magnet. Adaptations to the tube allowed for connection of anesthesia gas and ventilation. Ear and mouth bars were provided within the cylinder for securing the animal and to aid the minimization of motion.

Two major series of experiments were performed with the animals. The first series was primarily a development group as we tried to understand the blast wave and its effects on the rat cranium. This series involved 38 rats with blast exposures both on and off-axis. The second series was focused on blast exposure at a fixed location off-axis and involved 14 animals. In the second series greater attention was given to the membrane material and thickness. The overall protocol for each series generally adhered to one of the following protocols:

Series 1:

1. Control or baseline NMR examination of the animal
2. Induction of blast wave injury
3. 1 hour post blast injury follow up of animals
4. 1 day post blast injury follow up of animals
5. 2 day post blast injury follow up of animals
6. 3 day post blast injury follow up of animals
7. 4 day post blast injury follow up of animals
8. 7 or 8 day post blast injury follow up of animals

Or

Series 2:

1. Control or baseline NMR examination of the animal
2. Induction of blast wave injury
3. Induction of blast wave injury 24 hours following first blast exposure
4. 1 hour post blast injury follow up of animals
5. 1 day post blast injury follow up of animals
6. 2 day post blast injury follow up of animals

7. 5 day post blast injury follow up of animals
8. 7 day post blast injury follow up of animals

These two series developed out of trial and error measurements with the blast device and its ability to induce the desired TBI. The time between these two attempts was about 18 months, during which the above characterization of the blast wave device took place.

Series 1 was the initial attempt at creating injury. As uncertainty existed in the effect that the shock wave would have on the animal's cranium, a number of different positions were tested. These positions were 60 mm off-axis and either 50, 70 or 130 mm below the nozzle or 0 mm off-axis (directly below the nozzle) and 70 or 130 mm down. The predominate amount of data from this series comes from the animals that were placed at the 0 mm off-axis, 70 mm down location. At the other positions only one or two animals underwent blast wave trauma. Due to this low number of animals, those data will not be presented. Series 2 attempted to reestablish the off-axis model of induced injury by placing the cranium at the position established through the characterization of the blast device, that is, at 50 mm off-axis and 50 mm below the nozzle. The magnetic resonance imaging and spectroscopy data collection followed a defined protocol for both series of animal experiments. Imager setup and data acquisitions were performed in the following order:

1. Magnetic field shimming over the region of the brain.
2. Transmitter and receiver calibrations.
3. Sagittal scout acquisition w/ defining Coronal slices.
4. Coronal $T_1$ and $T_2$ weighted images.
5. Coronal inversion-recovery image acquisitions
6. Coronal diffusion-weighted image acquisition

7. Localized spectroscopic acquisition.

The total time required for these acquisitions was generally around 90 minutes.

Before any blast wave exposure was performed on the animals, they were first studied in the MR device to establish a set of baseline values. The baseline values are critical for understanding and elucidating any changes that might happen in the brain following blast. All animals were prepared as described above with anesthesia and ventilation. They were positioned in the stereotactic support tube and carried to the magnet. A receive-only surface coil was placed centrally over the head and secured, and then the animal positioned inside the transmitter radio frequency coil in the magnet. The cranium at this point is at iso-center of the magnet.

MR excitation and data reception was as described in Chapter 2. First a set of three co-planar $T_1$-weighted sagittal images were acquired through the brain. These are 2-dimensional images along the long axis of the animal and are used for localizing the position of the coronal 2-dimensional image to be acquired next. Sagittal images are meant to be quick and of lower resolution, the only significant anatomy to be identified in the brain is the triangular shape of the pituitary gland that is near the center of the brain. A sample sagittal image is shown in Figure 3.10. The primary parameters for this image are: 4.0 cm field of view, 96 x 96 matrix and a TR/TE of 500/10 milliseconds.

From the sagittal image, new images in an orthogonal or orthogonal-oblique plane may be prescribed using the Bruker software. For all the imaging protocols to be acquired from here on, a set of three images that are primarily in the anatomical coronal plane are selected. An example of this image selection is seen in Figure 3.10, where the new images are prescribed by

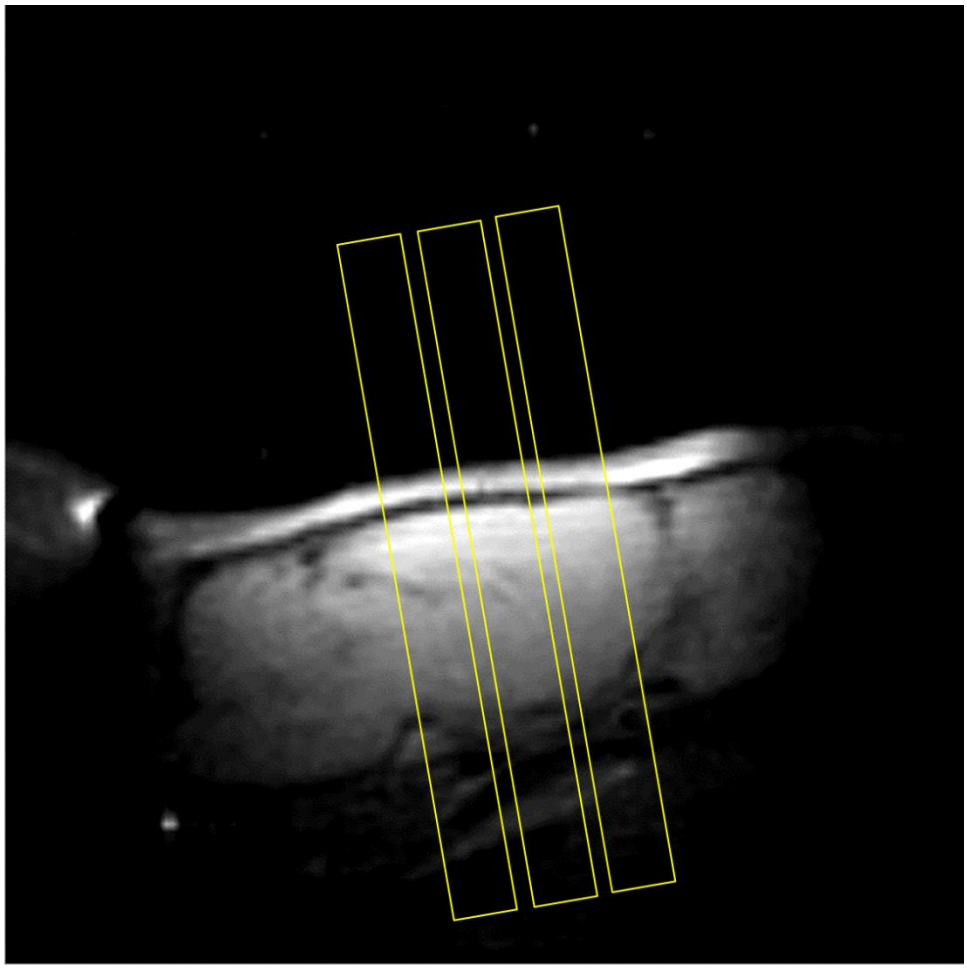

Figure 3.10. Sagittal $T_1$-weighted MR Image of a rat's brain.

the highlighted rectangles. These images are perpendicular to the sagittal images previously acquired, but are also maintained perpendicular to the top of the brain. The edge of the first image in the group of three is always positioned at the top of the triangular point of the pituitary gland. The coronal images for all the remaining protocols will be 2.5 millimeters thick and the center of each will be 3.0 millimeters off-axis from the center of the adjacent slice. These slices are chosen due to the relevant structure that may be visualized in each one; structure which will exhibit TBI induced changes.

The first sets of images to be collected are $T_1$- and $T_2$-weighted images. Examples of the $T_1$-weighted and $T_2$-weighted coronal images are shown in Figure 3.11 and 3.12. The acquisition parameters for the $T_1$-weighted images are: a field of view of 3.0 cm square, 128 x 128 matrix and a TR/TE of 500/10 milliseconds. Parameters for the $T_2$ image are similar, but with a TR/TE of 6000/100 milliseconds. The primary importance of these images is for anatomical localization. The $T_2$ image, in particular, is important for positioning the voxel to be used in localized spectroscopy. Additionally, the $T_2$ image, as explained earlier, is also very sensitive to visualizing edema. Both $T_1$- and $T_2$-weighted images suffer from the fact that they are native signal images. Beyond the Fourier transformation of the raw K-space data, no additional processing is applied. The intensity in each set of images is not only related to the $T_1$ and $T_2$ values of the tissue, but also to the signal strength. This is very apparent with the $T_2$ weighted images. The top of the brain, closest to the radio frequency surface coil, appears brighter due to the greater intensity of signal that the coil may receive from there. Tissue further away from the coil appears progressively darker. Images that are post-processed, where every pixel is evaluated separately from all the others in the image, will reduce this effect. The remaining sets of images to be acquired are all post-processed images.

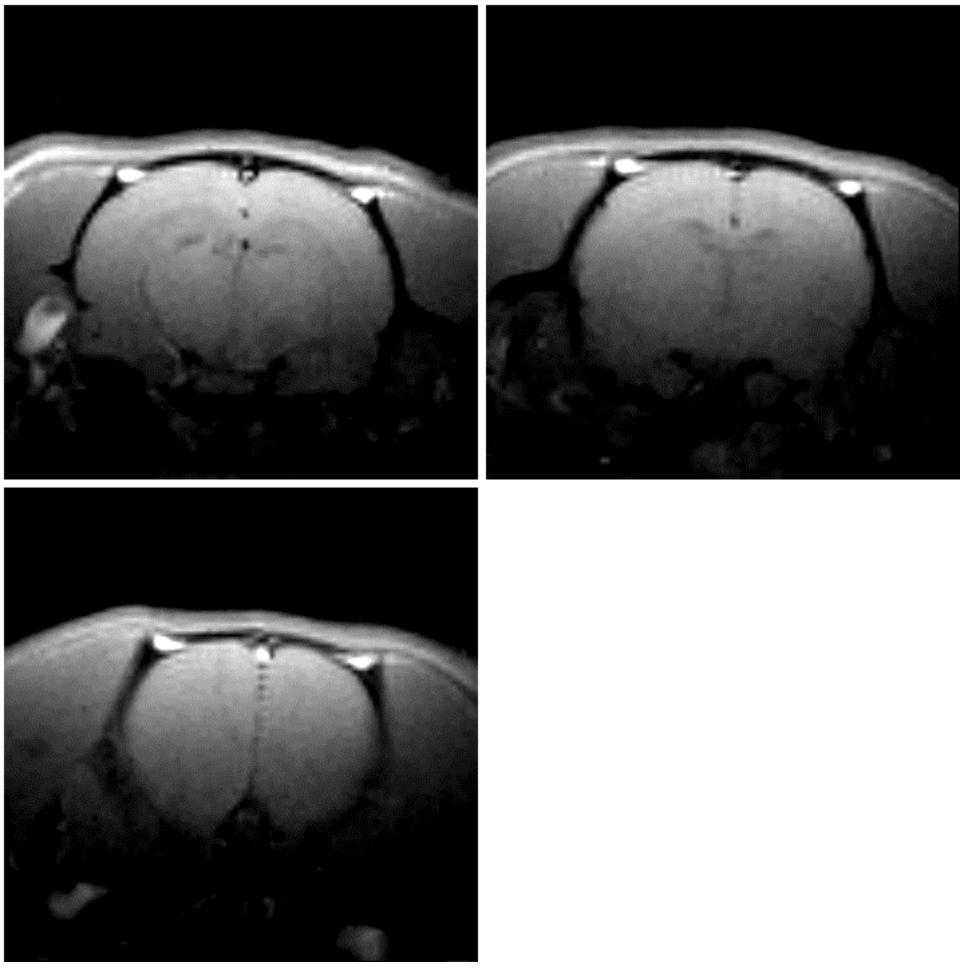

Figure 3.11. Coronal $T_1$-weighted MR Image of a rat's brain.

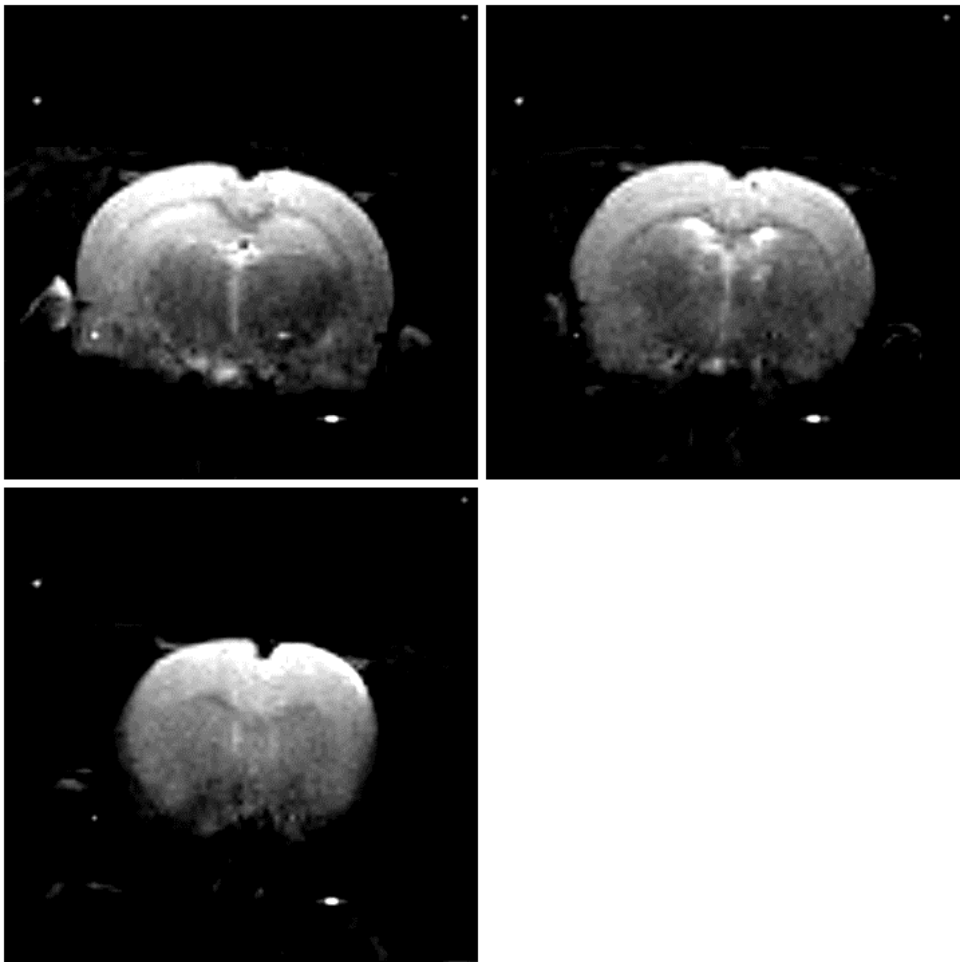

Figure 3.12. Coronal $T_2$-weighted MR Image of a rat's brain.

Images that are used for calculating a quantitative percent water value for every pixel, commonly called water-map images, were described in Chapter 2. The percent water map images are a secondary calculation on the quantitative $T_1$ map images. In a $T_1$ map, every pixel in the image is the quantitative $T_1$ relaxation value of that tissue. An example of calculated percent water map images from an animal are shown in Figure 3.13. The basic parameters employed with the inversion-recovery protocol used for creating the initial $T_1$-map images on the rat are: 3.0 cm square field of view, 128 x 128 matrix and TR/TE of 6000/29 milliseconds. For generating the $T_1$-map seven inversion-recovery images are acquired with the same basic parameters, but with a variable time between the inversion pulse and the image acquisition. The delay times chosen for the individual images are: 30, 150, 300, 700, 1300, 2500 and 4000 milliseconds. These seven images are fitted on a pixel-by-pixel basis to generate the $T_1$-map. As explained in Chapter 2, the $T_1$-maps are then further processed to yield images that are dependent on the percent concentration of water.

Figure 3.13. Coronal Percent Water MR Images of a rat's brain.

Likewise, the calculation of Trace Apparent Diffusion Coefficient or Fractional Anisotropy Images may be generated through pixel-by-pixel calculations of a number of diffusion weighted images. In this experiment seven DWI images are acquired. Each image again has the same basic acquisition parameters of a 3.0 cm field of view and 128 x 128 matrix. The TR/TE for the first series of animals was 1500 and 41 milliseconds, respectfully, but was modified to 1500 and 27 milliseconds, respectively, in the second series. This change was instituted to reduce the effect that animal motion has on the image set and will be described shortly. Due to the low sensitivity of the EPI pulse sequence, 10 repetitions of each acquisition step were performed. The first image of the seven has no diffusion weighting, while the remaining six applied a diffusion weighting along the Read/Phase (positive and negative gradient vector), Read/Slice axis (positive and negative gradient vector) and the Phase/Slice axis (positive and negative gradient vector) through a vector combination of diffusion weighted gradients on the respective axes. Processing the images involves first creating a diffusion map for each of the diffusion weighted directions, then further processing the data to create the Trace and fractional isotropy maps. Examples of Trace and Fractional anisotropy images are shown in Figures 3.14 and 3.15.

Lastly, proton spectroscopic acquisitions were carried out using the PRESS pulse sequence as described in Chapter 2. A voxel of 4.5 $mm^3$ was placed centrally in the brain of the rat. An example of the placement is shown in Figure 3.16. Basic acquisition parameters for spectroscopy are: TR/TE 3000/30 and 256 repetitions or number of scans. A proton spectra, acquired with these parameters is shown in Figure 3.17.

Once the image data was acquired, it was post-processed on a Sun workstation with the MRVision software (MRVision Co., Winchester, MA). The raw inversion-recovery images

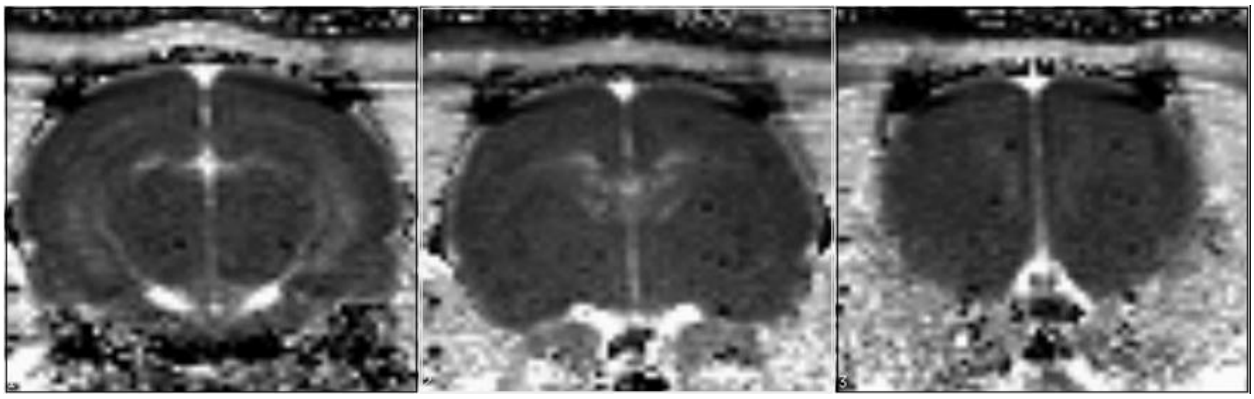

Figure 3.14. Coronal Trace ADC MR Images of a rat's brain.

Figure 3.15. Fractional Anisotropy MR Images of a rat's brain.

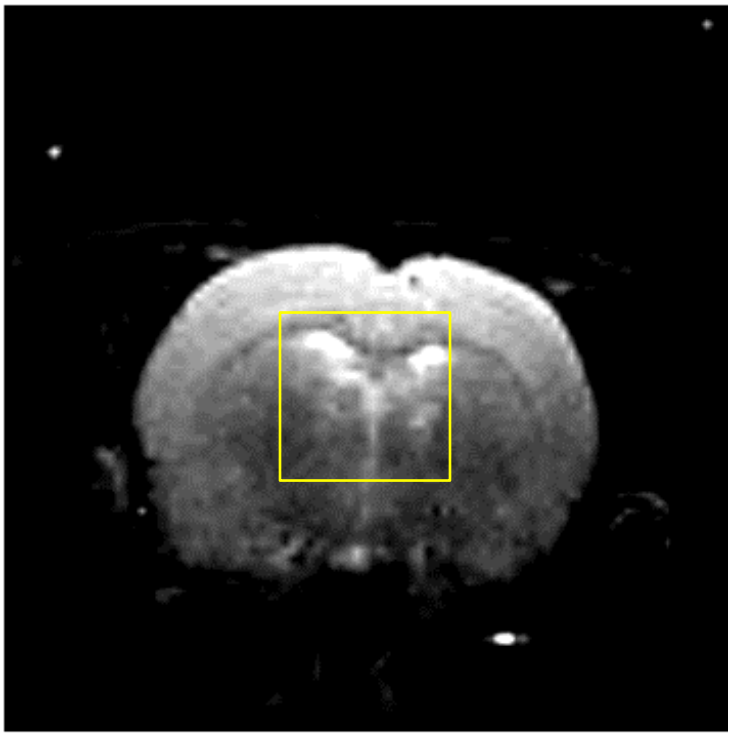

Figure 3.16. Coronal $T_2$-Weighted MR image with voxel for acquiring spectroscopic data

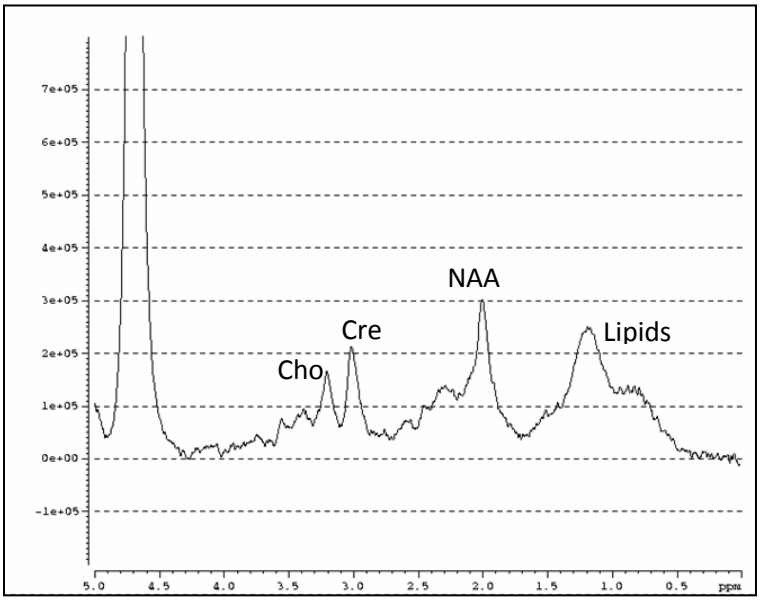


Figure 3.17. Proton Spectra Acquired from voxel

were inputted for generating first the $T_1$-maps, then the percent water-maps. Likewise, the raw diffusion-weighted images were inputted to generate first the Apparent Diffusion maps, then the Trace and Fractional Anisotropy images. As described above, images from three coronal slices were collected and processed. As each slice contains different tissue structure that could potentially exhibit some blast wave TBI effects, hand drawn specific region-of-interests (ROIs) were selected on each image. The choice of these ROIs was determined by the tissue structure that is known to exist in the selected slice [61], and through what can actually be visualized in the MR images. These regions-of-interest for each image slice are listed in Table 3.26 and visually drawn in Figure 3.16.

Table 3.26. Anatomical structure to be studied in MR images.

| | Slice 1: Position 4.5 mm posterior from Bregma | | | |
|---|---|---|---|---|
| | Cortex | Hippocampus | Thalamus | Whole Brain |
| TRACE | √ | √ | √ | √ |
| FA | √ | √ | √ | √ |
| Percent Water | √ | √ | √ | √ |
| | Slice 2: Position 1.5 mm posterior from Bregma | | | |
| | Cortex | Corpus Callosum | Caudate Putamen | Whole Brain |
| TRACE | √ | | √ | √ |
| FA | √ | | √ | √ |
| Percent Water | √ | √ | √ | √ |
| | Slice 3: Position 1.5 mm anterior from Bregma | | | |
| | Whole Brain | | | |
| TRACE | √ | | | |
| FA | √ | | | |
| Percent Water | √ | | | |

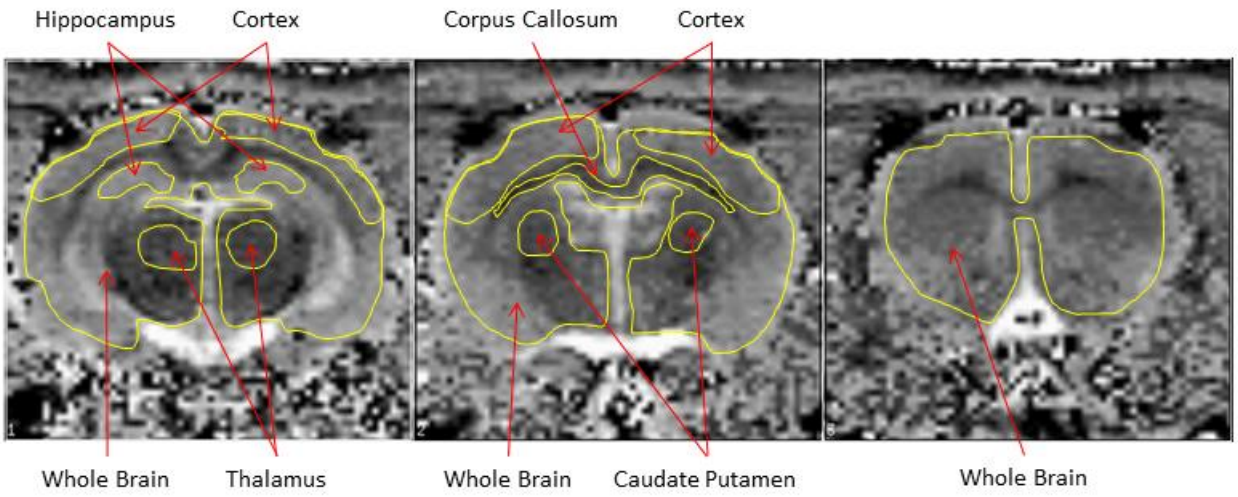


Figure 3.18. Coronal Percent Water MR Image with hand-drawn Region of Interests (ROIs)

For both series, as described above, the animals were prepared and positioned in the magnet and baseline data was acquired. The baseline data, as determined through the post-processing step and ROI analysis as previously described, are presented in Tables 3.27 – 3.30 for the first series of animals and Tables 3.31 – 3.33 for the second.

The numbers of animals that comprise the baseline data in each acquisition protocol, as well as data sets to be acquired after blast wave injury, is dependent on a number of parameters, some under our control and some that are not. The simplest parameter that determines the number of animals in the dataset is the actual number of animals that are scanned for baseline data. The optimal goal, of course, was to scan every animal before blast wave exposure, but that was not always possible for various reasons. Each dataset of MR images as described above required about 2 hours to complete. During a particular session, the raw image data may have been corrupted due to acquisition or animal issues.

Acquisition issues that were encountered involved inconsistent parameter execution associated with the NMR device. A defect in the software occasionally causes a phase error to appear in the images generated with the EPI technique. Also, the use of the very high diffusion gradient strengths could cause the gradient amplifiers to switch off due to an overload condition. If observed, the acquisition could be easily repeated and the problem resolved. If not observed though, and once the animal was removed from the magnet, the data became unrecoverable.

The most serious animal issue to be encountered was motion. Animal motion consisted of auto breaths and tremors, which involved the whole body, or lower jaw and tongue motion involving the head. As stated above, optimal conditions must be met with the anesthesia to produce a state where the animal will remain motionless. Not being able to monitor or observe the animal in the magnet greatly hinders this implementation during image acquisition.

Table 3.27. Percent Water MRI Baseline Data from Series 1 Animals for the "Entire Brain" ROI.

| % Water | Slice 1 | | | | Slice 2 | | | | Slice 3 | N |
|---|---|---|---|---|---|---|---|---|---|---|
| | Cortex | Hippocampus | Thalamus | Whole Brain | Cortex | Corpus Collusum | Caudate Putamen | Whole Brain | Whole Brain | |
| Mean | 76.9 | 78.1 | 71.9 | 75.6 | 76.3 | 71.4 | 71.8 | 75.4 | 75.7 | 14 |
| Stand. Dev. | 0.6 | 0.5 | 0.7 | 0.5 | 0.6 | 0.8 | 0.8 | 0.6 | 1.0 | |

Table 3.28. Trace ADC MRI Baseline Data from Series 1 Animals for the "Entire Brain" ROI.

| $mm^2/sec$ | Slice 1 | | | | Slice 2 | | | Slice 3 | N |
|---|---|---|---|---|---|---|---|---|---|
| | Cortex | Hippocampus | Thalamus | Whole Brain | Cortex | Caudate Putamen | Whole Brain | Whole Brain | |
| Mean | 0.72 | 0.78 | 0.77 | 0.78 | 0.73 | 0.76 | 0.76 | 0.73 | 13 |
| Stand. Dev. | 0.06 | 0.05 | 0.06 | 0.06 | 0.05 | 0.06 | 0.06 | 0.05 | |

Table 3.29. Fractional Anisotropy MRI Baseline Data from Series 1 Animals for the "Entire Brain" ROI.

| | Slice 1 | | | | Slice 2 | | | Slice 3 | N |
|---|---|---|---|---|---|---|---|---|---|
| | Cortex | Hippocampus | Thalamus | Whole Brain | Cortex | Caudate Putamen | Whole Brain | Whole Brain | |
| Mean | 0.37 | 0.34 | 0.37 | 0.38 | 0.38 | 0.48 | 0.39 | 0.40 | 13 |
| Stand. Dev. | 0.07 | 0.06 | 0.05 | 0.05 | 0.05 | 0.08 | 0.05 | 0.06 | |

Table 3.30. Proton Spectroscopy Baseline Data from Series 1 Animals.

| Ratio Relative to Creatine | 4.5 $cm^3$ Voxel | | | | N |
|---|---|---|---|---|---|
| | Inositol | Creatine | Choline | NAA | |
| Mean | 0.41 | 1.00 | 0.81 | 2.15 | 13 |
| Stand. Dev. | 0.19 | 0.00 | 0.17 | 0.50 | |

Table 3.31. Percent Water MRI Baseline Data from Series 2 Animals for the "Entire Brain" ROI.

| % Water | Slice 1 | | | | Slice 2 | | | | Slice 3 | N |
|---|---|---|---|---|---|---|---|---|---|---|
| | Cortex | Hippocampus | Thalamus | Whole Brain | Cortex | Corpus Collusum | Caudate Putamen | Whole Brain | Whole Brain | |
| Mean | 77.8 | 79.0 | 73.4 | 76.3 | 77.5 | 71.9 | 72.5 | 76.2 | 77.0 | 7 |
| Stand. Dev. | 1.0 | 1.1 | 1.2 | 0.9 | 0.8 | 0.7 | 0.8 | 0.8 | 0.7 | |

Table 3.32. Trace ADC MRI Baseline Data from Series 2 Animals for the "Entire Brain" ROI.

| $mm^2/sec$ | Slice 1 | | | | Slice 2 | | | Slice 3 | N |
|---|---|---|---|---|---|---|---|---|---|
| | Cortex | Hippocampus | Thalamus | Whole Brain | Cortex | Caudate Putamen | Whole Brain | Whole Brain | |
| Mean | 0.69 | 0.73 | 0.70 | 0.74 | 0.71 | 0.70 | 0.72 | 0.73 | 5 |
| Stand. Dev. | 0.05 | 0.04 | 0.05 | 0.05 | 0.04 | 0.03 | 0.04 | 0.04 | |

Table 3.33. Fractional Anisotropy MRI Baseline Data from Series 2 Animals for the "Entire Brain" ROI.

| | Slice 1 | | | | Slice 2 | | | Slice 3 | N |
|---|---|---|---|---|---|---|---|---|---|
| | Cortex | Hippocampus | Thalamus | Whole Brain | Cortex | Caudate Putamen | Whole Brain | Whole Brain | |
| Mean | 0.24 | 0.19 | 0.19 | 0.28 | 0.27 | 0.41 | 0.30 | 0.29 | 5 |
| Stand. Dev. | 0.03 | 0.01 | 0.02 | 0.01 | 0.01 | 0.02 | 0.02 | 0.01 | |

Following the completion of an acquisition, motion can be readily observed in the MR images. The $T_2$-weighted image that is acquired early in the overall MRI session, is particularly important for this as any motion that occurs during the long time between the two excitation pulses will induce phase distortions in the image. Adjustments in the isoflurane level may be made and the image reacquired. Some later animals in the first series received the drug vecuronium, a muscle relaxant, which may be used in conjunction with isoflurane.

A comparison of the baseline data from the two groups of animals shows that the measured values have some agreement, particularly when the large standard deviations are considered. Those ROI's that show variability between the two series are primarily due to the inability to control the animal motion in the first series. The predominate number of animals used for baseline measurements in the first series were imaged before the use of vecuronium. Qualitative analysis of the images showed that the motion could be somewhat reduced with vecuronium.

For the second series of animals, a detailed effort was put forth to address the animal motion issue. Careful analysis was performed on the ventilator calibration. Animal handlers (Jiepei Zhu, Travis Parsons), experienced with the Narcomed ventilator and rat anesthesia requirements, carefully observed and modified the unit's volume and respiratory rate settings. Likewise, the NMR acquisition protocols were modified. As described above, $T_2$-weighted images are adequate for an initial assessment of animal motion, but the protocol most easily overcome by motion is the diffusion-weighted images. The strong diffusion gradients readily amplify, through signal phase distortion, any ongoing motion. Significant parameter changes were made in the TR/TE values from the first series of animals to the second. As the many acquisition parameters are dependent on each other, two significant changes were made. These

were: 1) reducing the number of phase encoding steps per segment from 16 to 8, thereby doubling the acquisition time, but allowing the TE value to be greatly reduced, and 2) increasing the diffusion gradient strength from 100 to 200 milliTesla per meter, thereby allowing the duration of the applied gradient to be shortened, further reducing the TE. Overall, the TE was reduced from 41 to 27 milliseconds, but the acquisition time was increased from 15 to 30 minutes. The b-values for the diffusion gradients remained nearly the same, changing from 1007 to 1092 $sec^2/mm$. As we can assume that the animal is in a steady state in the magnet, additional acquisition time would be inconsequential.

Blast exposure was performed on the animals following baseline acquisitions. Blast exposures were either performed on the same day as the baseline acquisitions, or one to four days later. To perform the blast exposure, the animal was anesthetized and intubated as described above. The animal was positioned in the blast wave device and the distances from the blast wave nozzle to the center of the cranium were carefully measured. The nozzle and membrane were prepared and the intubation tube was disconnected immediately before blast exposure. The free end of the intubation tube was positioned so that the blast wave would not be able to enter it. Blast exposure was performed and the animal removed from the blast device and the intubation tube was reconnected. The entire procedure required less than 10 minutes.

Immediately following blast exposure, the animals would often enter a state of epileptic motion, which would last for less than one minute. Some animals suffered additional damage to vasculature in the ear, nose or eye. These additional injuries, although unsightly, did not provide any early indication of MRI outcome, as to be discussed below.

For the first series of animals, a timeline was followed as shown in Table 3.34. Each set of data from any particular animal took approximately two hours to perform. Complication with

Table 3.32. Series 1 Single blast exposure MRI timeline.

| | 9:00 AM | 10:00 AM | 11:00 AM | 12:00 PM | 1:00 PM | 2:00 PM | 3:00 PM | 4:00 PM | 5:00 PM |
|---|---|---|---|---|---|---|---|---|---|
| Friday | | | | | Rat 1-Baseline | | Rat 2-Baseline | | |
| Saturday | | | | | | | | | |
| Sunday | | | | | | | | | |
| Monday | Rat 3-Baseline | | Rat 4-Baseline | | Rat 5-Baseline | | Rat 2-4hour | | |
| | | | Rat 3-Blast | Rat 2-Blast | Rat 4-Blast | | Rat 5-Blast | | |
| Tuesday | Rat 3-Day 1 | | Rat 2-Day 1 | | Rat 4-Day 1 | | Rat 5-Day 1 | | |
| Wednesday | Rat 3-Day 2 | | Rat 2-Day 2 | | Rat 4-Day 2 | | Rat 5-Day 2 | | |
| Thursday | | | | | | | | | |
| Friday | Rat 3-Day 4 | | Rat 2-Day 4 | | Rat 4-Day 4 | | Rat 5-Day 4 | | |
| Saturday | | | | | | | | | |
| Sunday | | | | | | | | | |
| Monday | Rat 3-Day 7 | | Rat 2-Day 7 | | Rat 4-Day 7 | | Rat 5-Day 7 | | |

the anesthesia or MRI acquisitions could potentially increase that time. If possible, on the blast exposure day, a four hour post-blast measurement was performed. This necessitated the additional complication of re-anesthetizing and intubating the animal. The potential for complication limited the number of animals at this time point that were studied. Baseline data was collected on five animals in the event that one of them might expire during blast exposure.

For the second series of animals, two blast exposures, separated by 24 hours, were performed. The goal with the two blasts was to increase the intensity of injury to a level that might be observable either with the MRI or behavioral studies. A dual blast timeline is shown in Table 3.35. The same animal preparations procedures were followed with the dual blast model as with the single blast.

Magnetic resonance imaging data collection was the same as described above for the baseline data. Regions of interest were drawn on the post-processed percent water map and Trace images and compared with baseline data. The ROIs drawn were as described in Table 3.26.

Table 3.33. Series 2 Double blast exposure MRI timeline.

| | 9:00 AM | 10:00 AM | 11:00 AM | 12:00 PM | 1:00 PM | 2:00 PM | 3:00 PM | 4:00 PM | 5:00 PM |
|---|---|---|---|---|---|---|---|---|---|
| Friday | | | | | Rat 1-Baseline | | Rat 2-Baseline | | |
| Saturday | | | | | | | | | |
| Sunday | | | | | | | | | |
| Monday | | | Rat 3-Baseline | | Rat 4-Baseline | | | | |
| Tuesday | | | Rat 1 Blast 1 | Rat 2 Blast 1 | Rat 3 Blast 1 | Rat 4 Blast 1 | | | |
| Wednesday | | | Rat 1 Blast 2 | Rat 2 Blast 2 | Rat 3 Blast 2 | Rat 4 Blast 2 | | | |
| Thursday | Rat 1-Day 1 | | Rat 2-Day 1 | | Rat 3-Day 1 | | Rat 4-Day 1 | | |
| Friday | Rat 1-Day 2 | | Rat 2-Day 2 | | Rat 3-Day 2 | | Rat 4-Day 2 | | |
| Saturday | | | | | | | | | |
| Sunday | | | | | | | | | |
| Monday | Rat 1-Day 5 | | Rat 2-Day 5 | | Rat 3-Day 5 | | Rat 4-Day 5 | | |
| Tuesday | | | | | | | | | |
| Wednesday | Rat 1-Day 7 | | Rat 2-Day 7 | | Rat 3-Day 7 | | Rat 4-Day 7 | | |

### B.1. Blast Wave TBI Series 1 Animals

The complete MRI region-of-interest data from the first series of animals with a single blast wave exposure at 70 mm down and 0 mm off-axis are presented in Table 3.36 – 3.39. These tables include the percent water, Trace, fractional anisotropy and spectroscopy data. To access an initial global view of what could be happening to the rat brain following blast exposure, an ROI is drawn on the image data encompassing all of the brain tissue in each of the three slices. Care is used to exclude all cerebrospinal fluid spaces, as the high intensity of the pure water will skew the ADC and percent water results. These ROI's are labeled "Whole Brain" in Tables 3.36 and 3.38. The average value of these three "Whole Brain" ROI's is labeled "Entire Brain" and displayed for each time point at the right side of the tables. These "Entire Brain" values are the measured value (percent water or $mm^2/sec$) from approximately nine millimeters length of brain tissue. The entire rat brain is twenty mm in length. For the time course of the measurements, these values are plotted in Figures 3.19 through 3.21. Likewise, the NAA-to Creatine proton spectroscopy results are displayed in Figure 3.22. Similar charts could be created for each of the individual ROIs in each of the brain slices.

Similar to the "Entire Brain" ROI, the cortical tissue values from Slice 1 and 2 are averaged and displayed in the column titled "Entire Cortex" in Tables 3.36 through 3.38. This ROI represent tissue that is the closest to the skull and thereby closest to the blast exposure source. The "Entire Cortex" values plotted in Figure 3.23 for the measured time points.

Because these displayed data values involve the averaging of a number of animals at each time point, more precise analyses should involve a statistical comparison. Student's t-test is the most common, well understood and straight forward test for the comparison of two sets of data. The t-test is used to determine the significance of the difference between the means of sets of

Table 3.36. Percent Water MRI data of Series 1 animals with blast exposure at 0 mm off-axis and 70 mm down for the "Entire Brain" ROI.

| % Water | Slice 1 | | | | Slice 2 | | | | Slice 3 | | | N |
|---|---|---|---|---|---|---|---|---|---|---|---|---|
| | Cortex | Hippocampus | Thalamus | Whole Brain | Cortex | Corpus Collusum | Caudate Putamen | Whole Brain | Whole Brain | Entire Brain | Entire Cortex | |
| Baseline | 76.9 ±0.6 | 78.1 ±0.5 | 71.9 ±0.7 | 75.6 ±0.5 | 76.3 ±0.6 | 71.4 ±0.8 | 71.8 ±0.8 | 75.4 ±0.6 | 75.7 ±1.0 | 75.5 ±0.8 | 76.6 ±0.7 | 14 |
| Day 1 | 76.8 ±1.0 | 77.9 ±0.8 | 72.4 ±1.1 | 75.6 ±1.0 | 76.3 ±0.3 | 70.9 ±0.5 | 72.1 ±0.8 | 75.4 ±0.4 | 75.7 ±0.9 | 75.6 ±0.8 | 76.5 ±0.7 | 6 |
| Day 2 | 76.1 ±0.3 | 78.0 ±0.3 | 72.1 ±0.3 | 75.1 ±0.7 | 75.5 ±0.3 | 69.9 ±0.7 | 70.8 ±0.2 | 74.2 ±0.5 | 74.4 ±1.4 | 74.6 ±0.9 | 75.8 ±0.7 | 3 |
| Day 3 | 76.6 ±0.6 | 78.3 ±0.6 | 72.6 ±1.5 | 75.3 ±0.4 | 76.1 ±0.6 | 70.6 ±0.8 | 72.0 ±1.0 | 75.1 ±0.8 | 75.3 ±0.8 | 75.2 ±0.6 | 76.3 ±0.7 | 2 |
| Day 4 | 77.0 ±0.3 | 78.4 ±0.2 | 72.3 ±0.3 | 75.5 ±0.2 | 76.1 ±0.2 | 70.8 ±0.8 | 71.5 ±0.2 | 75.0 ±0.1 | 75.0 ±0.3 | 75.2 ±0.3 | 76.6 ±0.7 | 3 |
| Day 8 | 77.0 ±0.5 | 78.8 ±0.6 | 73.6 ±1.3 | 75.9 ±0.5 | 76.0 ±1.1 | 71.3 ±0.1 | 71.9 ±0.4 | 74.9 ±1.0 | 74.8 ±0.7 | 75.2 ±0.8 | 76.5 ±0.7 | 2 |

Table 3.37. Trace ADC MRI data of Series 1 animals with blast exposure at 0 mm off-axis and 70 mm down for the "Entire Brain" ROI .

| $mm^2/sec$ | Slice 1 | | | | Slice 2 | | | Slice 3 | | | N |
|---|---|---|---|---|---|---|---|---|---|---|---|
| | Cortex | Hippocampus | Thalamus | Whole Brain | Cortex | Caudate Putamen | Whole Brain | Whole Brain | Entire Brain | Entire Cortex | |
| Baseline | 0.72 ±0.06 | 0.78 ±0.05 | 0.77 ±0.06 | 0.78 ±0.06 | 0.73 ±0.05 | 0.76 ±0.06 | 0.76 ±0.06 | 0.73 ±0.05 | 0.76 ±0.06 | 0.73 ±0.05 | 13 |
| Day 1 | 0.65 ±0.02 | 0.70 ±0.04 | 0.70 ±0.04 | 0.73 ±0.04 | 0.66 ±0.04 | 0.69 ±0.03 | 0.69 ±0.04 | 0.69 ±0.03 | 0.70 ±0.04 | 0.66 ±0.03 | 5 |
| Day 2 | 0.70 ±0.01 | 0.74 ±0.02 | 0.73 ± 0.01 | 0.75 ±0.03 | 0.71 ±0.01 | 0.73 ±0.05 | 0.74 ±0.00 | 0.71 ±0.03 | 0.73 ±0.03 | 0.70 ±0.01 | 2 |
| Day 3 | 0.75 | 0.81 | 0.79 | 0.77 | 0.73 | 0.74 | 0.73 | 0.73 | 0.74 ±0.03 | 0.73 | 1 |
| Day 4 | 0.65 ±0.03 | 0.68 ±0.03 | 0.70 ±0.03 | 0.72 ±0.03 | 0.68 ±0.04 | 0.69 ±0.02 | 0.70 ±0.03 | 0.68 ±0.02 | 0.70 ±0.03 | 0.67 ±0.04 | 3 |
| Day 8 | 0.71 ±0.11 | 0.74 ±0.11 | 0.75 ±0.10 | 0.75 ±0.12 | 0.69 ±0.08 | 0.69 ±0.08 | 0.70 ±0.08 | 0.69 ±0.06 | 0.72 ±0.08 | 0.70 ±0.10 | 2 |

Table 3.38. Fractional Anisotropy MRI data of Series 1 animals with blast exposure at 0 mm off-axis and 70 mm down for the "Entire Brain" ROI .

| | | | | | Slice 2 | | | Slice 3 | | | |
|---|---|---|---|---|---|---|---|---|---|---|---|
| | | Hippocampus | Thalamus | Whole Brain | Cortex | Caudate Putamen | Whole Brain | Whole Brain | Entire Brain | Entire Cortex | N |
| Baseline | 0.37 ±0.07 | 0.34 ±0.06 | 0.37 ±0.05 | 0.38 ±0.05 | 0.38 ±0.05 | 0.48 ±0.08 | 0.39 ±0.05 | 0.40 ±0.06 | 0.39 ±0.05 | 0.37 ±0.02 | 13 |
| Day 1 | 0.31 ±0.03 | 0.27 ±0.05 | 0.26 ±0.03 | 0.32 ±0.02 | 0.32 ±0.02 | 0.39 ±0.07 | 0.32 ±0.03 | 0.34 ±0.02 | 0.33 ±0.03 | 0.33 ±0.02 | 5 |
| Day 2 | 0.32 ±0.00 | 0.31 ±0.01 | 0.27 ±0.00 | 0.34 ±0.02 | 0.32 ±0.01 | 0.45 ±0.02 | 0.34 ±0.02 | 0.35 ±0.01 | 0.34 ±0.01 | 0.32 ±0.01 | 2 |
| Day 3 | 0.24 | 0.23 | 0.33 | 0.32 | 0.30 | 0.47 | 0.35 | 0.31 | 0.33 ±0.02 | 0.27 ±0.04 | 1 |
| Day 4 | 0.29 ±0.02 | 0.27 ±0.02 | 0.26 ±0.03 | 0.32 ±0.01 | 0.32 ±0.01 | 0.43 ±0.05 | 0.33 ±0.02 | 0.37 ±0.02 | 0.34 ±0.03 | 0.30 ±0.01 | 3 |
| Day 8 | 0.38 ±0.14 | 0.31 ±0.08 | 0.34 ±0.01 | 0.38 ±0.05 | 0.38 ±0.02 | 0.48 ±0.01 | 0.37 ±0.01 | 0.40 ±0.01 | 0.38 ±0.03 | 0.38 ±0.08 | 2 |

Table 3.39. Proton Spectroscopy MR data of Series 1 animals with blast exposure at 0 mm off-axis and 70 mm down. The data is normalized to the Creatine peak.

| | NAA | Creatine | Choline | Inisotol | N |
|---|---|---|---|---|---|
| Baseline | 2.15 ±0.50 | 1.00 | 0.81 ±0.17 | 0.41 ±0.19 | 13 |
| Day 1 | 2.36 ±0.95 | 1.00 | 0.82 0.21 | 0.38 ±0.24 | 5 |
| Day 2 | 2.16 ±0.07 | 1.00 | 0.90 ±0.05 | 0.48 ±0.03 | 4 |
| Day 3 | 2.00 ±0.39 | 1.00 | 0.84 ±0.00 | 0.42 ±0.14 | 2 |
| Day 4 | 1.86 ±0.36 | 1.00 | 0.92 ±0.03 | 0.21 ±0.10 | 3 |
| Day 8 | 1.83 ±0.19 | 1.00 | 0.89 ±0.07 | 0.33 ±0.06 | 2 |

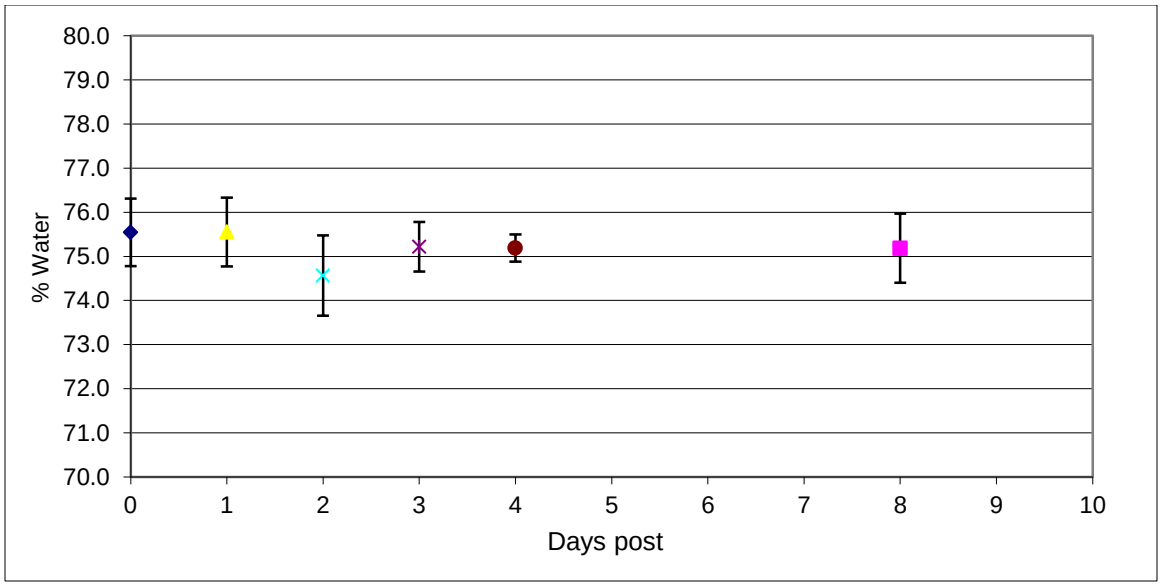


Figure 3.19. Percent Water MRI data from the "Entire Brain" of Series 1 animals with blast exposure at 70 mm down and 0 mm offset. Baseline data at time point "0".

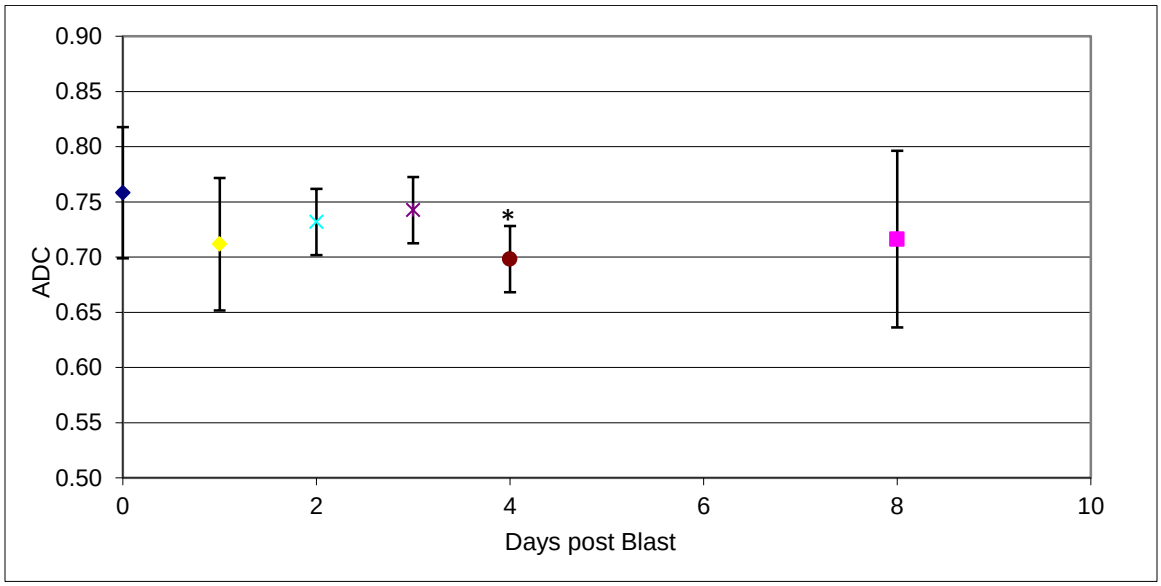


Figure 3.20. Trace ADC MRI data from the "Entire Brain" of Series 1 animals with blast exposure at 70 mm down and 0 mm offset. Baseline data at time point "0". *P ≤ 0.05.

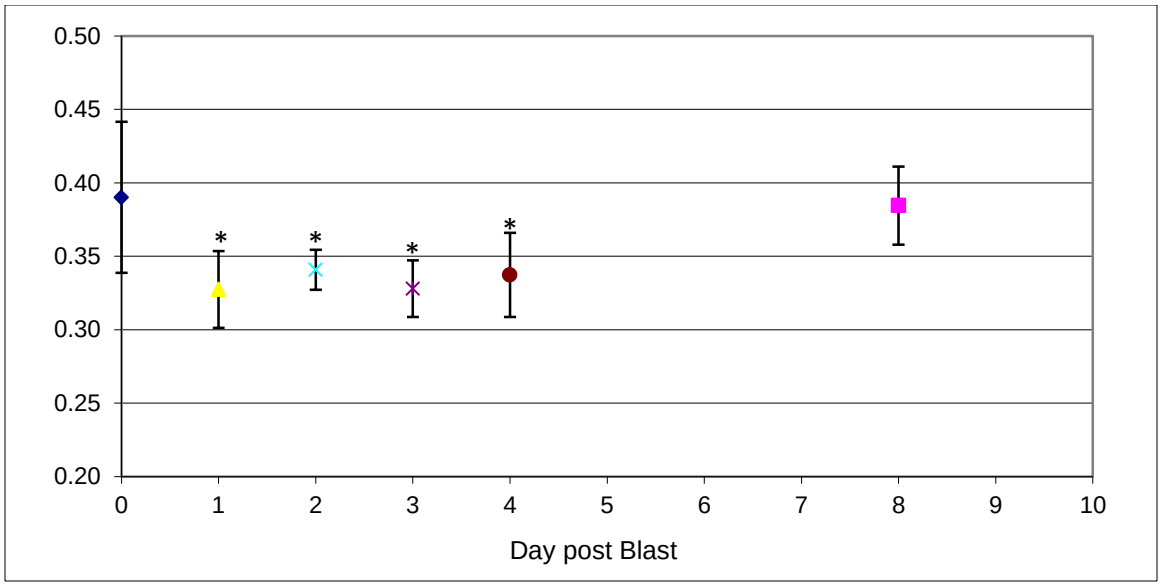


Figure 3.21. Fractional Anisotropy MRI data from the "Entire Brain" of Series 1 animals with blast exposure at 70 mm down and 0 mm offset. Baseline data at time point "0". *P ≤ 0.05.

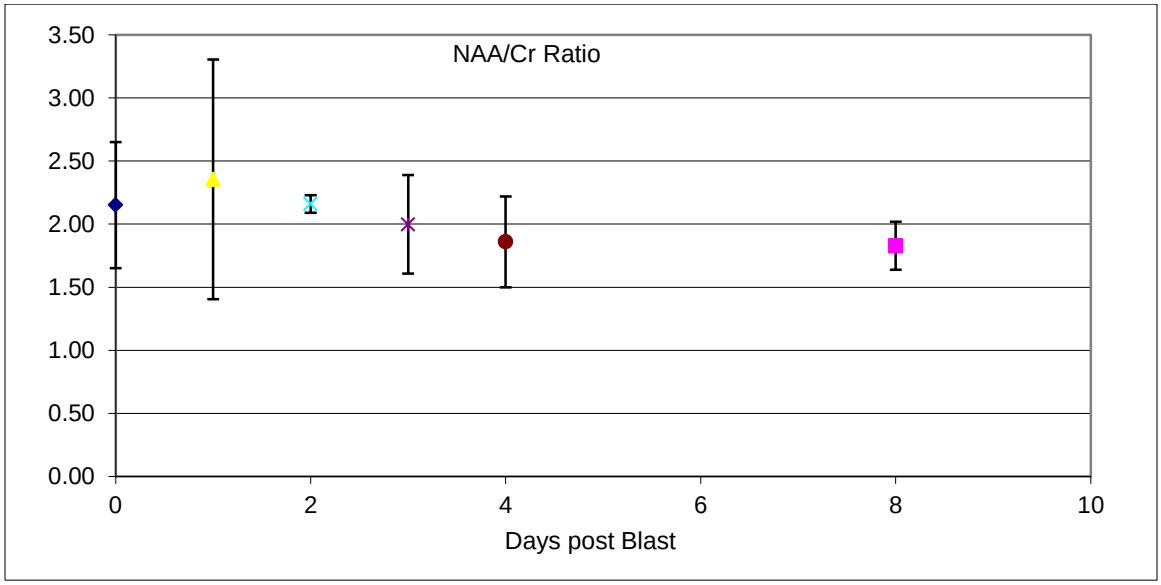


Figure 3.22. MR Spectroscopy data of NAA-to-Creatine ratio from Series 1 animals with blast exposure at 70 mm down and 0 mm offset. Baseline data at time point "0".

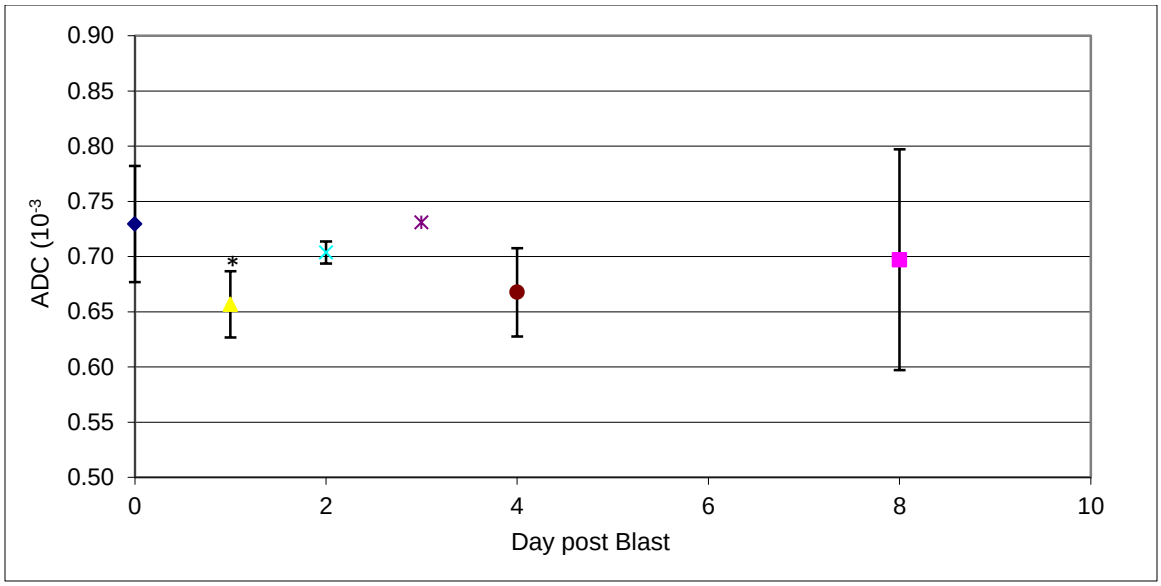


Figure 3.23. Trace ADC MRI data from the "Entire Cortex" of Series 1 animals with blast exposure at 70 mm down and 0 mm offset. Baseline data at time point "0". *P ≤ 0.05.

data. In essence, the test compares the difference in sample means relative to the observed random variations in each data set to calculate a t-value [62]. The t-value is then compared to critical values of the t-distribution plotted against the degrees of freedom, a parameter related to sampling size. Various probability levels may be inferred from the Critical t-value – degree of freedom chart that describe the degree to which the two sets of data are actually the same distribution. Historically, a probability of 5% (P=0.05) or less is sought. This probability is sufficiently small that the difference between the two sets of means would be considered to be "statistically significant"; that is, that the underlying distributions have very different means.

In this experiment, post blast injured animals at the different measured time points are compared to baseline animals in the hope of noting a difference. Due to the difficulties described above in collecting the data and maintaining the animals, it is very infrequent that the same animals will be imaged at every time point and therefore the number of data points in the baseline and post blast populations are seldom the same. The data must therefore be viewed independently and not paired.

The results from the t-test analysis of the image data for the percent water, Trace, FA and the spectroscopic ratios are shown in Tables 3.40, 3.41, 3.42 and 3.43, respectively. For the percent water data in Table 3.40 and the spectroscopic ratio data in Table 3.43, the P-values are routinely greater than the desired 0.05 percent that would indicate significance. For the Trace data, a single data point at 4 days post blast exposure has a P-value that would indicate significance. The overall relevance of this particular time point is uncertain, because the ADC values are at baseline levels for the day 3 and again at the following 7 day time point measurement. The fractional anisotropy data though, reveals significance for days 1, 2, 3 and 4

Table 3.40. Student T-test comparison of Percent Water MRI data from Series 1 animals with blast exposure at 0 mm off-axis and 70 mm down. $P \leq 0.05$ indicates significance.

| Probability (P) | Slice 1 | | | | Slice 2 | | | | Slice 3 | | |
|---|---|---|---|---|---|---|---|---|---|---|---|
| | Cortex | Hippocampus | Thalamus | Whole Brain | Cortex | Corpus Collusum | Caudate Putamen | Whole Brain | Whole Brain | Entire Brain | Entire Cortex |
| Day 1 | 0.76 | 0.63 | 0.41 | 0.98 | 0.99 | 0.17 | 0.48 | 0.93 | 0.93 | 0.98 | 0.78 |
| Day 2 | 0.01 | 0.90 | 0.53 | 0.35 | 0.02 | 0.04 | 0.00 | 0.04 | 0.25 | 0.09 | 0.00 |
| Day 3 | 0.59 | 0.80 | 0.66 | 0.50 | 0.69 | 0.36 | 0.82 | 0.65 | 0.66 | 0.62 | 0.64 |
| Day 4 | 0.65 | 0.06 | 0.12 | 0.76 | 0.32 | 0.32 | 0.24 | 0.06 | 0.06 | 0.06 | 0.82 |
| Day 8 | 0.90 | 0.37 | 0.33 | 0.59 | 0.70 | 0.70 | 0.81 | 0.61 | 0.29 | 0.61 | 0.84 |

Table 3.41. Student T-test comparison of Trace ADC MRI data from Series 1 animals with blast exposure at 0 mm off-axis and 70 mm down. $P \leq 0.05$ indicates significance.

| Probability (P) | Slice 1 | | | | Slice 2 | | | Slice 3 | | |
|---|---|---|---|---|---|---|---|---|---|---|
| | Cortex | Hippocampus | Thalamus | Whole Brain | Cortex | Caudate Putamen | Whole Brain | Whole Brain | Entire Brain | Entire Cortex |
| Day 1 | 0.00 | 0.03 | 0.11 | 0.11 | 0.05 | 0.03 | 0.05 | 0.14 | 0.08 | 0.02 |
| Day 2 | 0.13 | 0.11 | 0.09 | 0.34 | 0.21 | 0.63 | 0.24 | 0.43 | 0.30 | 0.16 |
| Day 3 | - | - | - | - | - | - | - | - | - | - |
| Day 4 | 0.02 | 0.00 | 0.05 | 0.03 | 0.16 | 0.01 | 0.04 | 0.02 | 0.03 | 0.07 |
| Day 8 | 0.86 | 0.70 | 0.89 | 0.78 | 0.56 | 0.45 | 0.05 | 0.54 | 0.62 | 0.72 |

Table 3.42. Student T-test comparison of Fractional Anisotropy MRI data from Series 1 animals with blast exposure at 0 mm off-axis and 70 mm down. $P \leq 0.05$ indicates significance.

| Probability (P) | Slice 1 | | | | Slice 2 | | | Slice 3 | | |
|---|---|---|---|---|---|---|---|---|---|---|
| | Cortex | Hippocampus | Thalamus | Whole Brain | Cortex | Caudate Putamen | Whole Brain | Whole Brain | Entire Brain | Entire Cortex |
| Day 1 | 0.05 | 0.03 | 0.00 | 0.00 | 0.00 | 0.04 | 0.00 | 0.01 | 0.00 | 0.03 |
| Day 2 | 0.02 | 0.19 | 0.00 | 0.13 | 0.01 | 0.24 | 0.05 | 0.00 | 0.03 | 0.00 |
| Day 3 | - | - | - | - | - | - | - | - | - | - |
| Day 4 | 0.00 | 0.00 | 0.00 | 0.00 | 0.00 | 0.17 | 0.00 | 0.13 | 0.00 | 0.00 |
| Day 8 | 0.94 | 0.72 | 0.08 | 0.87 | 0.93 | 0.97 | 0.23 | 0.95 | 0.82 | 0.96 |

Table 3.43. Student T-test comparison of proton spectroscopy data of Series 1 animals with blast exposure at 0 mm off-axis and 70 mm down. The data is normalized to the Creatine peak. $P \leq 0.05$ indicates significance.

| Probability (P) | NAA/Cr | Choline/Cr | Inositol/Cr |
|---|---|---|---|
| Day 1 | 0.67 | 0.94 | 0.90 |
| Day 2 | 0.96 | 0.14 | 0.25 |
| Day 3 | 0.68 | 0.50 | 0.93 |
| Day 4 | 0.31 | 0.05 | 0.06 |
| Day 8 | 0.17 | 0.28 | 0.35 |

post blast wave exposure. This FA data could be a strong indication that disruption of the neuronal pathways has occurred due to the blast.

Trace ADC values as measured in the cortical tissue ROI , named “Entire Cortex”, and displayed in Figure 3.23, indicate that there exists a drop in the ADC values for the cortex at 1 day post blast wave trauma. Day 2 and 3 show ADC values that appear to return to the baseline value. From Table 3.41, the t-test analysis results of this “Entire Cortex” data do reveal that the P values at Day 1 indicate a significant difference from the baseline data. This could be indicative of a transient effect.

Overall, these values tend to suggest that the blast wave, as applied to the rat at 0 mm off-axis and 70 mm below the nozzle, can induce a transient neurological detriment of the brain as measured by MRI.

### B.2. Blast Wave TBI Series 2 Animals

The second series of animals followed a concerted effort to improve the quality and reproducibility of the data acquired from each animal. The numerous steps taken to achieve this included a through characterization of the blast box, reevaluating the animal anesthesia and modification in the MRI acquisitions protocols: all of which have been described above. In the first series of animals, blast exposure appeared to produce a slight and transient measureable detriment in the brain as measured with the processed MR images. In an attempt to increase the potential severity of the injury, a dual blast regimen was employed, with blast exposure to a single animal occurring on two consecutive days. This protocol was shown in Table 3.35.

The MRI data collection was entirely as described above. $T_1W$, $T_2W$, inversion-recovery images for a percent water map calculation and diffusion weighted imaged for Trace calculations were collected. Proton spectroscopy was attempted on all of the animals at all-time points, but a serious phase distortion issue was prevalent throughout the acquired spectra, the cause of which was most likely related to magnet field inhomogeneity across the voxel. Every effort was made for accurate shimming using techniques that had been developed over many years in the NMR laboratory, but the problem could not be resolved.

The percent water, Trace and fractional anisotropy data for the series of animals that received the dual shock wave blasts at 50 mm down and 50 mm off-axis are shown in Tables 3.44, 3.45 and Table 3.46, respectively. As above in the Series 1 data, the ROI data for the "Entire Brain" is plotted and shown in Figure 3.24 for the percent water and Figure 3.25 for the Trace data. Unlike the data in Series 1, this data tends to show a consistency with the baseline value over the post blast exposure time points. It appears that no change is occurring in the MRI observable brain parameters following the off-axis, dual blast wave exposure.

Table 3.44. Percent Water MRI data of Series 2 animals with blast exposure at 50 mm off-axis and 50 mm down for the "Entire Brain" ROI.

| % Water | Slice 1 | | | | Slice 2 | | | | Slice 3 | | N |
|---|---|---|---|---|---|---|---|---|---|---|---|
| | Cortex | Hippocampus | Thalamus | Whole Brain | Cortex | Corpus Collusum | Caudate Putamen | Whole Brain | Whole Brain | Entire Brain | |
| Baseline | 77.8 ±1.0 | 79.0 ±1.1 | 73.4 ±1.2 | 76.3 ±0.9 | 77.5 ±0.8 | 71.9 ±0.7 | 72.5 ±0.8 | 76.2 ±0.8 | 77.0 ±0.7 | 76.5 ±0.8 | 7 |
| 1 Hour | 76.9 ±1.8 | 77.4 ±2.8 | 73.9 ±0.4 | 75.7 ±1.3 | 77.5 ±0.5 | 71.6 ±0.1 | 72.4 ±0.9 | 76.5 ±0.3 | 77.9 ±0.3 | 76.7 ±1.2 | 2 |
| Day 1 | 78.1 ±0.4 | 79.2 ±0.6 | 73.5 ±0.7 | 76.5 ±0.5 | 77.2 ±0.2 | 71.7 ±0.2 | 72.5 ±0.5 | 75.9 ±0.2 | 76.2 ±0.6 | 76.2 ±0.5 | 3 |
| Day 2 | 77.9 ±0.6 | 78.9 ±0.6 | 73.2 ±0.6 | 76.1 ±0.6 | 77.3 ±0.9 | 71.6 ±0.8 | 72.1 ±0.4 | 75.7 ±0.7 | 76.3 ±1.2 | 76.0 ±0.9 | 3 |
| Day 5 | 77.6 ±1.0 | 79.2 ±0.6 | 72.9 ±0.6 | 76.1 ±0.8 | 76.8 ±0.8 | 71.9 ±1.0 | 71.6 ±0.4 | 75.5 ±0.8 | 75.6 ±0.7 | 75.8 ±0.7 | 3 |
| Day 7 | 78.0 ±0.5 | 79.3 ±0.1 | 73.5 ±0.6 | 76.4 ±0.3 | 77.7 ±0.4 | 71.9 ±0.4 | 72.6 ±0.5 | 76.4 ±0.2 | 77.1 ±0.8 | 76.6 ±0.5 | 3 |

Table 3.45. Trace ADC MRI data of Series 2 animals with blast exposure at 50 mm off-axis and 50 mm down for the "Entire Brain" ROI.

| $mm^2/sec$ | Slice 1 | | | | Slice 2 | | | Slice 3 | | N |
|---|---|---|---|---|---|---|---|---|---|---|
| | Cortex | Hippocampus | Thalamus | Whole Brain | Cortex | Caudate Putamen | Whole Brain | Whole Brain | Entire Brain | |
| Baseline | 0.69 ±0.05 | 0.73 ±0.04 | 0.70 ±0.05 | 0.74 ±0.05 | 0.71 ±0.04 | 0.70 ±0.03 | 0.72 ±0.04 | 0.73 ±0.04 | 0.73 ±0.04 | 5 |
| 1 Hour | 0.70 ±0.08 | 0.74 ±0.06 | 0.73 ±0.03 | 0.74 ±0.07 | 0.72 ±0.06 | 0.70 ±0.06 | 0.71 ±0.06 | 0.72 ±0.07 | 0.72 ±0.05 | 2 |
| Day 1 | 0.71 ±0.03 | 0.75 ±0.03 | 0.72 ±0.03 | 0.75 ±0.03 | 0.70 ±0.02 | 0.70 ±0.02 | 0.71 ±0.02 | 0.74 ±0.02 | 0.74 ±0.03 | 2 |
| Day 2 | 0.67 ±0.05 | 0.72 ±0.06 | 0.70 ±0.06 | 0.72 ±0.06 | 0.68 ±0.01 | 0.68 ±0.02 | 0.70 ±0.02 | 0.71 ±0.04 | 0.71 ±0.04 | 3 |
| Day 5 | 0.72 ±0.02 | 0.76 ±0.01 | 0.74 ±0.01 | 0.76 ±0.02 | 0.71 ±0.02 | 0.71 ±0.01 | 0.72 ±0.02 | 0.75 ±0.02 | 0.74 ±0.02 | 3 |
| Day 7 | 0.71 ±0.01 | 0.74 ±0.01 | 0.71 ±0.01 | 0.74 ±0.00 | 0.70 ±0.00 | 0.69 ±0.01 | 0.71 ±0.00 | 0.74 ±0.01 | 0.73 ±0.02 | 2 |

Table 3.46. Fractional Anisotropy MRI data of Series 2 animals with blast exposure at 50 mm off-axis and 50 mm down for the "Entire Brain" ROI

| | Slice 1 | | | | Slice 2 | | | Slice 3 | | |
|---|---|---|---|---|---|---|---|---|---|---|
| | Cortex | Hippocampus | Thalamus | Whole Brain | Cortex | Caudate Putamen | Whole Brain | Whole Brain | Entire Brain | N |
| Baseline | 0.24 ±0.03 | 0.19 ±0.01 | 0.19 ±0.02 | 0.28 ±0.01 | 0.27 ±0.01 | 0.41 ±0.02 | 0.30 ±0.02 | 0.29 ±0.01 | 0.29 ±0.02 | 5 |
| 1 Hour | 0.26 ±0.02 | 0.24 ±0.05 | 0.22 ±0.04 | 0.32 ±0.01 | 0.36 ±0.04 | 0.43 ±0.08 | 0.34 ±0.04 | 0.32 ±0.01 | 0.33 ±0.02 | 2 |
| Day 1 | 0.23 ±0.01 | 0.20 ±0.00 | 0.19 ±0.01 | 0.28 ±0.01 | 0.28 ±0.01 | 0.40 ±0.02 | 0.29 ±0.01 | 0.28 ±0.00 | 0.28 ±0.01 | 2 |
| Day 2 | 0.25 ±0.02 | 0.23 ±0.07 | 0.24 ±0.05 | 0.33 ±0.06 | 0.29 ±0.01 | 0.40 ±0.08 | 0.32 ±0.01 | 0.33 ±0.02 | 0.33 ±0.03 | 3 |
| Day 5 | 0.21 ±0.02 | 0.20 ±0.04 | 0.18 ±0.04 | 0.26 ±0.03 | 0.25 ±0.03 | 0.42 ±0.01 | 0.30 ±0.01 | 0.30 ±0.02 | 0.28 ±0.02 | 3 |
| Day 7 | 0.22 ±0.01 | 0.18 ±0.01 | 0.19 ±0.04 | 0.28 ±0.00 | 0.26 ±0.01 | 0.44 ±0.02 | 0.30 ±0.01 | 0.29 ±0.02 | 0.29 ±0.01 | 2 |

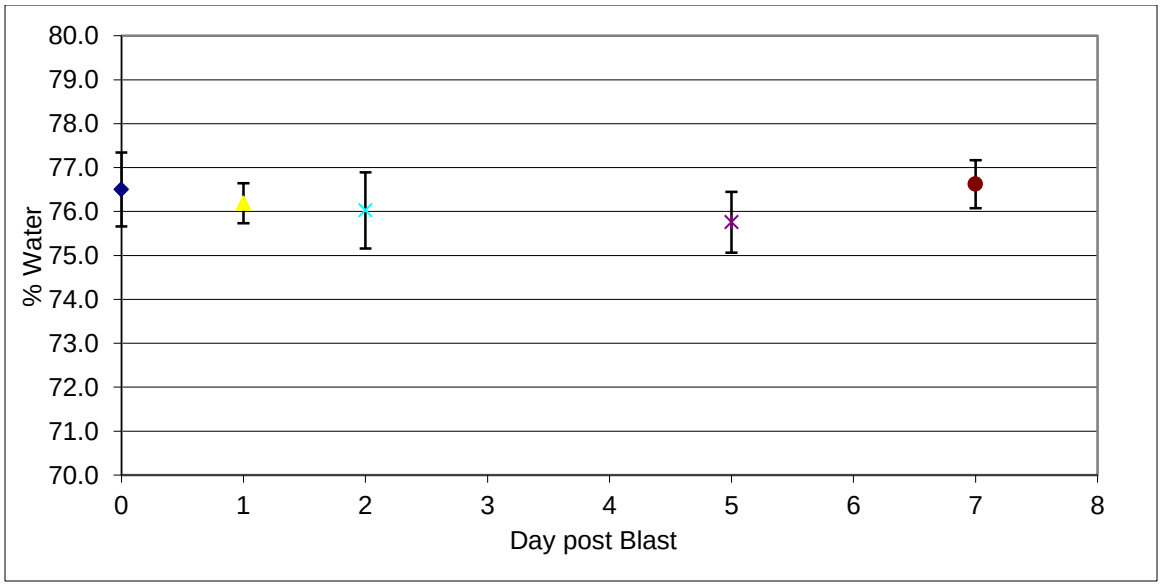


Figure 3.24. Percent Water MRI data from the "Entire Brain" of Series 2 animals with blast exposure at 50 mm down and 50 mm offset. Baseline data at time point "0".

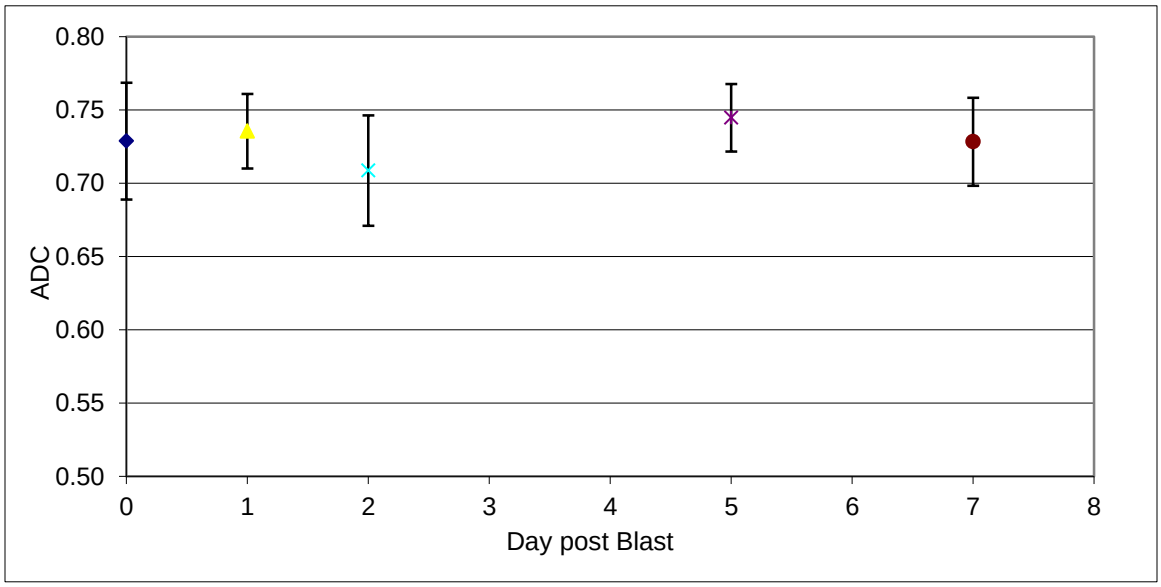


Figure 3.25. Trace ADC MRI data from the "Entire Brain" of Series 2 animals with blast exposure at 50 mm down and 50 mm offset. Baseline data at time point "0".

T-test analysis was also performed on this data with the results shown in Tables 3.47 through 3.49 for the percent water, Trace, and FA images, respectively. As predicted from the figures for the "Entire Brain" ROI, there is no significance ($P \leq 0.05$) between the baseline and post blast time point data for the percent water and Trace data. Fractional anisotropy for the "Entire Brain" ROI, Table 3.49, contains one point, at 1 day post blast exposure, that shows significance. From Table 3.46, it can be seen that this FA value increased from baseline, completely in opposition of what would be expected with neuronal damage. This significant data point must therefore be held in suspicion.

In all, the MRI data from the second series of animals to undergo blast wave exposure at 50 mm off-axis and 50 mm down shows no measureable detriment to the brain.

Table 3.47. Student T-test comparison of Percent Water data from Series 2 animals with blast exposure at 50 mm off-axis and 50 mm. $P \leq 0.05$ indicates significance.

| Probability (P) | Slice 1 | | | | Slice 2 | | | | Slice 3 | |
|---|---|---|---|---|---|---|---|---|---|---|
| | Cortex | Hippocampus | Thalamus | Whole Brain | Cortex | Corpus Collusum | Caudate Putamen | Whole Brain | Whole Brain | Entire Brain |
| 1 Hour | 0.61 | 0.57 | 0.38 | 0.64 | 0.86 | 0.31 | 0.85 | 0.47 | 0.04 | 0.67 |
| Day 1 | 0.50 | 0.78 | 0.88 | 0.66 | 0.28 | 0.68 | 0.96 | 0.29 | 0.12 | 0.40 |
| Day 2 | 0.89 | 0.85 | 0.76 | 0.70 | 0.61 | 0.63 | 0.30 | 0.27 | 0.27 | 0.34 |
| Day 5 | 0.76 | 0.79 | 0.43 | 0.78 | 0.26 | 0.91 | 0.04 | 0.26 | 0.04 | 0.22 |
| Day 7 | 0.76 | 0.51 | 0.87 | 0.68 | 0.75 | 0.83 | 0.90 | 0.68 | 0.93 | 0.77 |

Table 3.48. Student T-test comparison of Trace ADC data from Series 2 animals with blast exposure at 50 mm off-axis and 50 mm down and. $P \leq 0.05$ indicates significance.

| Probability (P) | Slice 1 | | | | Slice 2 | | | Slice 3 | |
|---|---|---|---|---|---|---|---|---|---|
| | Cortex | Hippocampus | Thalamus | Whole Brain | Cortex | Caudate Putamen | Whole Brain | Whole Brain | Entire Brain |
| 1 Hour | 0.90 | 0.93 | 0.35 | 0.99 | 0.85 | 0.91 | 0.98 | 0.86 | 0.95 |
| Day 1 | 0.68 | 0.66 | 0.57 | 0.74 | 0.66 | 0.67 | 0.96 | 0.67 | 0.80 |
| Day 2 | 0.55 | 0.70 | 0.96 | 0.73 | 0.23 | 0.27 | 0.44 | 0.39 | 0.52 |
| Day 5 | 0.42 | 0.30 | 0.14 | 0.30 | 0.82 | 0.62 | 0.67 | 0.58 | 0.48 |
| Day 7 | 0.54 | 0.81 | 0.57 | 0.72 | 0.77 | 0.73 | 0.59 | 0.93 | 0.99 |

Table 3.49. Student T-test comparison of Fractional Anisotropy data from Series 2 animals with blast exposure at 50 mm off-axis and 50 mm down and. $P \leq 0.05$ indicates significance.

| Probability (P) | Slice 1 | | | | Slice 2 | | | Slice 3 | |
|---|---|---|---|---|---|---|---|---|---|
| | Cortex | Hippocampus | Thalamus | Whole Brain | Cortex | Caudate Putamen | Whole Brain | Whole Brain | Entire Brain |
| 1 Hour | 0.42 | 0.40 | 0.49 | 0.08 | 0.16 | 0.85 | 0.38 | 0.16 | 0.13 |
| Day 1 | 0.39 | 0.11 | 0.59 | 0.96 | 0.57 | 0.45 | 0.17 | 0.10 | 0.04 |
| Day 2 | 0.59 | 0.42 | 0.17 | 0.27 | 0.08 | 0.83 | 0.08 | 0.05 | 0.14 |
| Day 5 | 0.22 | 0.68 | 0.69 | 0.31 | 0.38 | 0.40 | 0.69 | 0.54 | 0.21 |
| Day 7 | 0.14 | 0.18 | 0.88 | 0.93 | 0.13 | 0.33 | 0.61 | 0.80 | 0.53 |

# Chapter 4

## Summary and Conclusions

As has become clearly understood from observation and experimentation over the last 100 years, blast wave exposure has the potential for inducing significant injury to personnel in the immediate vicinity. The degree of injury depends directly on the force and the distance of the explosive event. Personnel injuries from blast waves may present in a variety of symptoms depending on the anatomical structure affected by the wave. In this study, specific damage to the neurological state was investigated with a newly designed device for generating blast wave exposure.

The novel design of this blast device is to allow free field blast wave exposure to subjects at various distances from the shock wave generating center. This was accomplished through the use of a nozzle and membrane system, such that when the membrane ruptured under high pressure, a shock wave was created and emitted from the nozzle. An animal could be positioned at measureable distances from the opening of the nozzle, to experience the force of the shock wave and/or air blast.

Numerous blast wave exposures from the blast device were measured with a piezoelectric transducer to gain an understanding of the shape and intensity of the resultant blast wave. The measurements were carried out at different locations in the blast field and under maximum different shock wave amplitudes. Four membrane materials were investigated. They were polyvinylchloride, PETG, polycarbonate and Mylar. The shock wave amplitude was found to be

reproducible for the different membranes at a given rupturing pressures. Of particular note with the chosen membranes were their great differences in bursting pressure. Because of these differences, a choice of Mylar membranes was made for performing the majority of the remaining tests and for use with the animal experiments. The shock wave was additionally observed to be emitted symmetrically from the blast nozzle. The air blast component, as described earlier, was readily observable at measurement points nearly on-axis with the nozzle and with careful planning could be avoided in the animal studies.

Animal studies were performed to test the hypothesis that shock wave exposure to the cranium will induce traumatic brain injury. Two major series of animals were investigated. The first series involved blast wave exposure from the blast device before it had been thoroughly investigated. Blast exposures were performed on rats and MRI images were acquired to search for indications that would have implied injury. These indications would have been a reduction in the apparent diffusion coefficient and/or fractional anisotropy, an increase in the total water content of the brain, or a decrease in the N-acetylaspartate to creatine spectroscopic ratio, as the NAA decreases.

Data that suggested injury in the first series of animals included a single time point drop in the ADC at Day 4 for the “Entire Brain” and at Day 1 for the “Entire Cortex”. It is possible that these are transient events, but the possibility exists that these are also spurious data points. Fractional Anisotropy yields the strongest suggestion that something significant happened to the neuronal pathways following blast exposure. The drawbacks from this series of animals was that blast exposure was performed directly on-axis, so as has been described before, the brain of the animal received not only the shock wave, but also the energy from the following air blast, which could have amplified the injury.

The second series of animals, performed after careful characterization of the blast wave device and the shock wave, involved placing the cranium of an animal at an off-axis location deemed to be optimal for inducing injury. Animals exposed at this location received the maximum shock wave pressure attainable with the setup configuration of the blast device. Additionally, the coexistent air blast would not contribute to any observed injury. Magnetic resonance imaging assessment of the brain following a double blast exposure again revealed no major detriment.

Detriment in the brain following traumatic brain injury is well documented in the literature [63] [57] and have been investigated in this NMR research laboratory for many years. The increase in the water content throughout the entire brain can exceed 2 percent above baseline within 1 day following TBI. Likewise, the ADC has been reported to drop at least 10 percent in the days following trauma. The origins of these detriments are believed to be related to the disturbance of the cellular osmoregulation resulting in the intracellular uptake of water. The fact that no detriment was observed in the second series of animal studies with the blast wave device is a strong indicator that the shock wave alone is of insufficient amplitude to induce injury.

Inducing traumatic brain injury in rats is tremendously difficult. Previous experience in the NMR laboratory has shown that a single insult to the rat cranium was frequently insufficient for creating MR observable injury. Often, a secondary insult would be applied along with a traumatic brain injury event. These secondary injuries consisted of either hypoxia or hypoventilation [64]. Apparent diffusion coefficient map magnetic resonance imaging from these animals showed a significant drop in the ADC values from baseline to post injury, with the ability to correlate the ADC values to the degree of injury. These studies were all performed on the same NMR system that is currently being used for this blast wave study.

The second series of animals studied in this protocol underwent a second insult in the hope of increasing injury severity. The blast exposure was repeated twice over a 24 hour period. As MR image analysis has shown, this regimen was still not severe enough. The blast wave impact is at best very similar to a low force, diffuse closed head injury.

It was our hope that blast device would induce injury with a free field shock wave. Unfortunately due to the rapid diminishment in the amplitude of the shock wave with distance, insufficient amplitude is available for inducing an injury. Attempts to bring the animal closer to the blast nozzle would result in the animals experiencing the force of the air blast emanating from the nozzle. A potential remedy would be to increase the pressure in the nozzle by increasing the membrane thickness. As shown, the higher rupture pressure would increase the amplitude of the shock wave. Limitations exist, however though in the maximum pressure that can be delivered by the high pressure air cylinder, and more importantly by the basic design of the current setup. The pressure retaining capacity of the air lines or the blast nozzle itself could be exceeded. Increasing the limits on both of these items would require a significant re-working of the entire blast device.

Alternatively, the concept of a shock tube could be incorporated into the current structure. As discussed previously, the shock tube confines the blast wave and allows it to travel greater distances with minimal decrease in amplitude. These distances can be made great enough to allow the force of the air blast to diminish before reaching the end of the tube. And most importantly, shock tubes have been shown to be effective in generating blast injury [65]. Incorporating a shock tube design might be as simple as securely attaching the tube directly to the blast nozzle. The tube should have similar dimension as the nozzle output.

Blast wave traumatic brain injury is currently an area of study that is being vigorously pursued. Global political instabilities have forced this injury modality into the forefront and have provided many opportunities for innovative research and reliable funding. The current funding for this particular blast induce traumatic brain injury project is continuing beyond the completion date of the research described herein. In the future, efforts will continue to improve the blast delivery device and improve the quality of the magnetic resonance imaging.

# Bibliography


1. Maas, A.I.R., N. Stocchetti, and R. Bullock, *Moderate and severe traumatic brain injury in adults.* The Lancet Neurology, 2008. **7**(8): p. 728.

2. Summers, C., B. Ivins, and K. Schwab, *Traumatic Brain Injury in the United States: An Epidemiologic Overview.* Mount Sinai Journal of Medicine, 2009. **76**: p. 105-110.

3. Marmarou, A., *A review of progress in understanding the pathophysiology and treatment of brain edema.* Neurosurg. Focus, 2007. **22**(5): p. 1-10.

4. Stuhmiller, J.H., I. Yancy Y. Phillips, and D.R. Richmond, *The Physics and Mechanisms of Primary Blast Injury*. The Textbook of Military Medicine-Conventional Warfare, ed. R. Bellamy and R. Zajtchuk. Vol. 5. 1991, Washington, DC: Department of the Army, Office of Surgen General. 241-270.

5. Friedlander, F., *The diffraction of sound pulses.* Proceedings of the Royal Society, 1946. **186**: p. 322-367.

6. Wolf, S.J., et al., *Blast Injuries.* The Lancet, 2009. **374**: p. 405-415.

7. Liberman, M. and A. Velikovich, *Physics of shock waves in gases and plasmas*. Springer Series in Electrophysics, ed. G. Ecker, W. Engl, and L. Felsen. Vol. 19. 1986, New York: SpringerpVerlag. 385.

8. Landau, L.D. and E.M. Lifshitz, *Fluid Mechains*. Addison-Wesley Series in Advanced Physics, ed. J.B. Sykes and W.H. Reid. Vol. 6. 1959, Reading: Addison-Wesley Publishing Co., Inc. 536.

9. Leung, L., et al., *Blast related neurotrauma: a review of cellualr injury.* Mol Cell Biomech, 2008. **5**(3): p. 155-168.

10. Garner, J. and S.J. Brett, *Mechanisms of Inury by Explosive Devices.* Anesthesioloy Clin, 2007. **25**(1): p. 147-160.

11. Ritenour, A.E. and T.W. Baskin, *Primary blast injury: Update on diagnois and treatment.* Crit Care Med, 2008. **36**(7): p. S311-S317.

12. Hicks, R.R., et al., *Neurological effects of blast injury.* J Trauma, 2010. **68**(5): p. 1257-63.

13. Cernak, I., *Animal Models of Head Trauma.* NeuroRX, 2005. **2**(3): p. 410.

14. Saljo, A., et al., *Neuropathology and Pressure in the pig brain resulting from low-impulse noise exposure.* Journal of Neurotrauma, 2008. **25**: p. 1397-1406.

15. Taber, K., D. Warden, and R. Hurley, *Blast-related traumatic brain injury: what is known?* J. Neuropsychiatry Clin Neurosci, 2006. **18**(2): p. 141-145.

16. Okie, S., *Traumatic brain injury in the war zone.* N Engl J Med, 2005. **352**(20): p. 2043-2047.

17. Phillips, Y. and D. Richmond, *Primary blast injury and basic research: a brief history*. The Textbook of Military Medicine-Conventional Warfare, ed. R. Bellamy and R. Zajtchuk. Vol. 5. 1991, Washington, DC: Department of the Army, Office of Surgen General. 221-240.

18. Myers, C.S., *A contribution to the study of shell shock.: Being an account of three cases of loss of memory, vision, smell and taste, admitted into the duchess of Westminister's War Hospital, Le Touquet.* The Lancet, 1915. **185**(4772): p. 316-320.

19. Mott, F., *The effects of high explosives upon the CNS. Lecture I.* Lancet, 1916. **4824**: p. 331-338.

20. Mott, F., *The effects of high explosives upon the CNS. Lecture III.* Lancet, 1916. **4828**: p. 554-553.

21. Jones, E., N.T. Fear, and S. Wessely, *Shell Shock and Mild Traumatic Brain Injury: A Historical Review.* Am J Psychiatry, 2007. **164**(11): p. 1641-1645.

22. Mott, F., *Mental hygiene in shell shock during and after the war.* J Ment Sci, 1917. **63**: p. 467-488.

23. Jones, E. and S. Wessley, *"Forward Psychiatry" in the military: its origin and effectiveness.* Journal of Traumatic Stress, 2003. **16**(4): p. 411-419.

24. Prideaux, F., *Conference of Neurologists and Represenatatives of the Service Departments. Compensation in Cases of Neurashenia and Psychosis.* 1938.

25. Macleod, A.D., *Shell shock, Gordon Holmes and the Great War.* J R Soc Med, 2004. **97**(2): p. 86-89.

26. Shephard, B., *A War of Nerves: Soliders and Psychiatrist in the Twentieth Century*. 1 ed2001: Harvard University Press. 512.

27. Mott, F., Journal Roy. Army Med. Corps, 1917. **29**: p. 662.

28. Hooker, D.R., *Physiological Effects of Air Concussion.* American Journal of Physiology, 1924. **67**(2): p. 219-273.

29. Southborough, L., ed. *Report of the War Office Committee of Enquiry into "Shell-shock"*. 1922, His Majesty's Stationary Office: London. 202.

30. Carver, A. and A. Dinsley, *Some Biological Effects due to High Explosives.* Brain, 1919. **42**(2): p. 113-129.

31. Mira, E., *Psychiatric experiences in the Spanish War.* British Medical Journal, 1939. **1**: p. 1217-1220.

32. Culpin, M., *Concussion and War Psychiatry.* British Medical Journal, 1939. **2**: p. 37.
33. Schaller, W., *After-effect of head injury.* Journal of American Medical Association, 1939. **113**(20): p. 1779-1785.

34. Stewart, O.W.M.D., CAPTAIN R.C.A.M.C., C.K.M.D. Russel, LIEUT.-COLONEL R.C.A.M.C., and W.V.M.D. Cone, LIEUT.-COLONEL R.C.A.M.C., *INJURY TO THE CENTRAL NERVOUS SYSTEM BY BLAST : OBSERVATIONS ON A PHEASANT* The Lancet, 1941. **237**(6128): p. 172-174.

35. Fulton, J.F., *Blast Concussion in the Present War.* New England J. Med., 1942. **226**: p. 1-8.

36. Abbott, W.D., F.O. Due, and W.A. Nosik, *Subdural hematoma and effusion as a result of blast injuries.* J. Am. Med. Assoc., 1943. **121**(10): p. 739-741.

37. Pollock, L., *Blast injuries of the central nervous system.* Illinois Med. J., 1943. **83**: p. 165-168.

38. Roger, L., *Blast injury of the brain.* Med. J. Aust., 1943. **2**: p. 209-210.

39. Aita, J.A., Captain, MC, Aus and W.Z. Kerman, Captain, MC, Aus., *The closed head injury syndrome due to blast, bull.* U.S. Army M. Dept., 1946. **6**: p. 411-427.

40. Fabing, H.D., *Cerebral Blast Syndrome in Combat Soliders.* Arch. Neurol. & Psychiat., 1947. **57**: p. 14-57.

41. Cramer, F., S. Paster, and C. Stephenson, *Cerebral injuries due to explosion waves - "Cerebral Blast Concussion".* Archives of Neurolgy and Psychiatry, 1949. **61**(1): p. 1-20.

42. Denny-Brown, D.E., *The effect of high explosives on the post-traumatic syndrome.* Trans. Am. Neurol. A., 69. **69**: p. 98-102.

43. Benzinger, T. and R. Rossle. Jahrbuch der Deutschen Akademie der Luftfahrtforschung, 1943.

44. Blair, W. and F. Schulze, *Technical Memorandum No. 17-1, Psychological and Physiological Effects of Muzzle and Breech Blast*, 1956, U.S. Army: Aberdeen Proving Ground, MD.

45. Fomin, N., *110 years of experiments on shock tubes.* Journal of Engineering Physics and Thermophysics, 2010. **83**(6): p. 1118-1135.

46. Cernak, I., et al., *Blast Injury from Explosive Munitions.* The Journal of Trauma, 1999. **47**(1): p. 96-103.

47. Chavko, M., et al., *Measurement of blast wave by a miniature fiber optic pressure transducer in the rat brain.* Journal of Neuroscience Methods, 2007. **159**(2): p. 277-281.

48. Long, J.B., et al., *Blast Overpressure in Rats: Recreating a Battlefield Injury in the Laboratory.* Journal of Neurotrauma, 2009. **26**(6): p. 827-840.

49. Jaffin, J.H., et al., *A Laboratory Model for Studing Blast Overpressuer Injury.* Journal of Trauma, 1987. **27**(4): p. 349-356.

50. Irwin, R.J., et al., *Global Primary Blast Injury: A Rat Model.* J Oklahoma State Med Assoc, 1998. **91**(7): p. 387-392.

51. Ohashi, K., H. Kleine, and K. Takayma, *Characteristics of blast waves generated by milligram charges.* Proc. ISSW23, 2001.

52. McRobbie, D.W., et al., *MRI From Picture to Proton*, 2005, Cambridge University Press. p. 359.

53. LeBihan, D., et al., *Diffusion tensor imaging: concepts and applications.* J Magn Reson Imaging, 2001. **13**(4): p. 534-46.

54. Bernstein, M.A., K.F. King, and X.J. Zhou, *Handbook of MRI Pulse Sequences*2004, Oxford: Elsevier Academic Press. 1017.

55. Pierpaoli, C. and P. Basser, *Toward a quantitative assessment of diffusion anisotrophy.* Magn Reson Med, 1996. **36**(6): p. 893-906.

56. Fatouros, P., et al., *In vivo brain water determination by $T_1$ measurements: effect of total water content, hydration fraction, and field strength.* Magn Reson Med, 1991. **17**(2): p. 402-413.

57. Pascual, J., et al., *Time course of early metabolic changes following diffuse traumatic brain injury in rats as detected by $^{1}H$ NMR Spectroscopy.* J Neurotrauma, 2007. **24**(6): p. 944-959.

58. Kleindienst, A., et al., *Assessment of S100B levels by proton magnetic resonance spectroscopy after lateral fulid-percussion injury in the rat.* J Neurosurg, 2005. **102**(6): p. 1115-1121.

59. Signoretti, S., et al., *N-Acetylaspartate Reduction as a Measure of Injury Severity and Mitochondiral Dysfunction Following Diffuse Traumatic Brain Injury.* Journal of Neurotrauma, 2001. **18**(10): p. 977-991.

60. Akoka, S., *Magnetic Resonance Spectroscopy in Biology and Medicine*, ed. J.D.d. Certaines, W.M.M.J. Bovee, and F. Podo1992, New York: Pergamon Press. 689.

61. Paxino, G. and C. Watson, *The Rat Brain in Stereotaxic Coordinates*. Fourth ed1998, San Diego, CA: Academic Press.

62. Cherry, S., J. Sorenson, and M. Phelps, *Physics in Nuclear Medicine*2003, Philadelphia: Saunders.

63. Barzo, P., et al., *Contribution of vasiogenic and cellular edema to traumatic brain swelling measured by diffusion-weighted imaging.* J Neurosurg, 1997. **87**: p. 900-907.

64. Ito, J., et al., *Characterization of edema by diffusion-weighted imaging in experimental traumatic brain injury.* Journal of Neurosurgery, 1996. **84**(1): p. 97-103.

65. Cernak, I., et al., *Cognitive deficits following blast injury-induced neurotrauma: possible involvement of nitric oxide.* Brain Injury, 2001. **15**(7): p. 593.

## VITAE

Frank David Corwin was born on December 30, 1962 in Frankfurt, Germany and is a citizen of the United States of America. He graduated in 1981 from Denbigh High School in Newport News, Virginia. He received a Bachelor of Science in Physics from Virginia Polytechnic Institute and State University in 1985 and subsequently a Master of Science in Physics from Virginia Commonwealth University (VCU) in 1994. Beginning in 1987, he began working for Virginia Commonwealth University on the Medical College of Virginia campus, in the Department of Radiology as the primary operator and coordinator of the research Nuclear Magnetic Resonance Imaging laboratory. During his tenure at VCU, he has attained the position of Assistant Professor. Following graduation, he will continue employment with VCU, performing Magnetic Resonance Imaging research and providing clinical Medical Physics support. He is Board Certified by the American Board of Radiology in Radiological Physics and is a member of the American Association of Physicists in Medicine. Mr. Corwin is married and has three children.

BIBLIOGRAPHY:


Zhang J, Fatouros PP, Shu C, Reid J, Owens LS, Cai T, Gibson HW, Long GL, Corwin FD, Chen ZJ, Dorn HC: High relaxivity trimetallic nitride ($Gd_3N$) metallofullerene MRI contrast agents with optimized functionality. Bioconjugate Chem:21:610-615, 2010.

Shu C, Corwin F, Zhang J, Chen Z, Reid J, Sun M, Xu W, Sim JH, Wang C, Fatouros P, Esker A, Gibson H, Dorn H: Facile preparation of a new gadofullerene-based magnetic resonance imaging contrast agent with high $^1H$ relaxivity. Bioconjugate Chem:20:1186-1193, 2009.

Durrant D, Corwin F, Simoni D, Zhao M, Rudek M, Salloum F, Kukreja R, Fatouros P, Lee R: *cis*-3,4',5-Trimethoxy-3'aminostilbene disrupts tumor vascular perfusion without damaging normal organ perfusion. Cancer Chemother Pharmacol:63:191-200, 2009.

Fatouros P, Corwin F, Chen Z, Broaddus W, Tatum J, Kettenmann B, Ge Z, Gibson H, Russ J, Leonard A, Duchamp J, Dorn H: In vitro and in vivo Imaging Studies of a New Endohedral Metallofullerene Nanoparticle. *Radiology*:240(3):756-764, 2006.

Kleindienst A, Tolias C, Corwin F, Muller C, Marmarou A, Fatouros P, Bolluck M: Assessment of Cerebral S100B Levels be Mr Proton Spectroscopy. *Journal of Neurosurgery*:102(6):1115-1121, 2005.

Barzo P, Czigner A, Marmarou A, Beaumont A, Deak G, Fatouros P, Corwin F: [Increasing cerebral perfusion pressure in srious cranial injury – contradictory effects of dopamine]. *Ideggyogy Sz* [Hungarian]:58(7-8), 2005.

Chen ZJ, Gillies G, Broaddus W, Prabhu S, Fillmore H, Mitchell R, Corwin F, Fatouros P: A realistic brain phantom for intraparenchymal infusion studies. *Journal of Neurosurgery*:101*:*314-322, 2004.

Beaumont A, Hayasaki K, Marmarou A, Barzo P, Fatouros P, Corwin F: Contrasting Effects of Dopamine Therapy in Experimental Brain Injury. *Journal of Neurotrauma:*18:1359, 2001.

Alessandri B, Rim AL-Samsam, Corwin F, Fatouros P, Young H, Bullock R: Acute and late changes in N-acetyl-aspartate following diffuse axonal injury in rats: An MRI spectroscopy and micro dialysis Study. *Neurological Research:22:*705-712, 2000.

Portella G, Beaumont A, Corwin F, Fatouros P, Marmarou A: Characterizing Edema Associated with Cortical Contursion and Secondary Insult using Magnetic Resonance Spectroscopy. *Acta Neurochir 2000 (Suppl):76:273-275,* 2000.

Beaumont A, Fatouros P, Corwin F, Marmarou CR, Marmarou A: The Influence of Secondary Insults on Blood Brain Barrier Dysfunction in Contused Brain. *Journal of Neurotrauma:*16:966, 1999.

Tsuchida E, Alessandri B, Corwin F, Fatouros P, Bullock R: Detection of Ultra-Early Brain Damage After Acute Subdural Hematoma in the Rat by Magnetic Resonance Imaging. *Journal of Neurotrauma:16:*595-602, 1999.

Barzó P, Marmarou A, Fatouros P, Corwin F, Dunbar J: Acute Blood-Brain Barrier Changes in Experimental Closed Head Injury as Measured by MRI and Gd-DTPA. *Brain Edema X.*, H James, L Marshall, H-J Ruelen, *et-al*. (editors), Springer Verlag, Wien/New York. *Acta Neurochir (Suppl)*:*70*:243-246, 1997.

Barzó P, Marmarou A, Fatouros P, Hayasaki K, Corwin F: Biphasic Pathophysiological Response of Vasogenic and Cellular Edema in Traumatic Brain Swelling. *Brain Edema X.*, H James, L Marshall, H-J Ruelen, *et-al*. (editors), Springer Verlag, Wien/New York. *Acta Neurochir (Suppl)*:*70*:119-122, 1997.

Barzó P, Marmarou A, Fatouros P, Ito J, Corwin F: MRI Diffusion-Weighted Spectroscopy of Reversible and Irreversible Ischemic Injury Following Closed Head Injury. *Brain Edema X.*, H James, L Marshall, H-J Ruelen, *et-al*. (editors), Springer Verlag, Wien/New York. *Acta Neurochir (Suppl)*:*70*:115-118, 1997.

Hayasaki K, Marmarou A, Barzó P, Fatouros P, Corwin F: Detection of Brain Atrophy following Closed Head Injury. *Brain Edema X.*, H James, L Marshall, H-J Ruelen, *et-al*. (editors), Springer Verlag, Wien/New York. *Acta Neurochir (Suppl)*:*70*:75-77, 1997.

Barzó P, Marmarou A, Fatouros P, Hayasaki K, Corwin F: Contribution of Vasogenic and Cellular Edema to Traumatic Brain Swelling Measured by Diffusion-Weighted Imaging. *Journal of Neurosurgery*:*87:*900-907, 1997.

Di X, Bullock R, Watson J, Fatouros P, Chenard B, White F, Corwin F: Effect of CP101,606, a Novel NR2B Subunit Antagonist of the N-Methyl-D-Aspartate Receptor, on the Volume of Ischemic Brain Damage and Cytotoxic Brain Edema after Middle Cerebral Artery Occlusion in the Feline Brain. *Stroke*:*28,* 2244-2251, 1997.

Kraft K, Fatouros P, Corwin F, Fei D: *In Vitro* Validation of Rapid MR Measurement of Wave Velocity. *Journal of Magnetic Resonance*:*126,* 103-109, 1997.

Barzó P, Marmarou A, Fatouros P, Corwin F, Dunbar J: Magnetic Resonance Imaging-monitored acute Blood-Brain Barrier Changes in Experimental Traumatic Brain Injury. *Journal of Neurosurgery*:*85:1113-1121,* 1996.

Ito J, Marmarou A, Barzó P, Fatouros P, Corwin F: Characterization of Edema by Diffusion-Weighted Imaging in Experimental Traumatic Brain Injury. *Journal of Neurosurgery*:*85,*97-103, 1996.

Yoshida K, Corwin F, Marmarou A: "Effect of THAM in Brain Edema in Experimental Brain Injury", *Acta Neurochir (Suppl)*:*51*:317-319, 1990.